Aus der Medizinischen Klinik und Poliklinik IV der

Ludwig-Maximilians-Universität München

Direktor: Prof. Dr. med. Martin Reincke

The Pathogenesis of Chronic Uric Acid Crystal Nephropathy

Dissertation

zum Erwerb des Doktorgrades der Medizin

an der Medizinischen Fakultät der

Ludwig-Maximilians-Universität München

vorgelegt von

Moritz Roman Hernández Petzsche

aus León, México

2021

Mit Genehmigung der Medizinischen Fakultät

der Ludwig-Maximilians-Universität München

Berichterstatter:	PD Dr. Stefanie Steiger
Mitberichterstatter:	Prof. Dr. Alexander Buchner
Mitberichterstatter:	PD Dr. Heike Pohla
Mitberichterstatter:	PD Dr. Michael Schmolke

Dekan : Prof. Dr. med. dent. Reinhard Hickel

Tag der mündlichen Prüfung: 01.07.2021

Publications resulting from this project:

Sellmayr M[#], Hernandez Petzsche MR[#], Ma Q, Krüger N, Liapis H, Brink A, Lenz B, Angelotti ML, Gnemmi V, Kuppe C, Kim H, Bindels EMJ, Tajti F, Saez-Rodriguez J, Lech M, Kramann R, Romagnani P, Anders HJ, Steiger S. Only Hyperuricemia with Crystalluria, but not Asymptomatic Hyperuricemia, Drives Progression of Chronic Kidney Disease. *J Am Soc Nephrol.* 2020 Sep 16. doi: 10.1681/ASN.2020040523. PMID: 32938648.

# equal contribution

Poster presentation at the 54th ERA-EDTA Congress June 3rd-6th 2017 in Madrid:

Moritz Hernandez Petzsche, Stefanie Steiger, Helen Liapis, Hans-Joachim Anders. Hyperuricemia- and gouty arthritis-related medullary gout tophi associate with glomerulosclerosis and interstitial fibrosis in a series of 81,200 kidney biopsies.

Table of Contents

Zusammenfassung

Die chronische Nierenerkrankung (CKD) stellt einen wichtigen globalen ungedeckten medizinischen Bedarf dar. Zu einer Vielzahl von CKD-Ursachen zählen die kristallinen Nephropathien. In diesem Projekt wurden die Pathogenese und Relevanz der chronischen Harnsäurekristall-Nephropathie untersucht. Die chronische Harnsäurekristall-Nephropathie (oder Gichtnephropathie) wird definiert als das Vorhandensein von Harnsäure Granulomen im Nierenmark. Dieser Befund ist häufig mit einer ausgedehnten Nierenvernarbung verbunden. Vor einigen Jahrzehnten bezweifelten jedoch eine Reihe von Veröffentlichungen die klinische Relevanz der Gichtnephropathie, und die Forschung zu diesem Thema stagnierte seitdem. Ein weiteres umstrittenes Untersuchungsthema ist ob die Hyperurikämie zu einem Fortschreiten der CKD beiträgt. Ziel meines Projekts war es, medulläre Tophi mithilfe moderner Untersuchungstechniken neu zu bewerten: (1) die histologischen Anomalien diagnostischer Nierenbiopsien in einer großen Fall-Kontroll-Studie zu charakterisieren, (2) ein zuverlässiges Mausmodell für die Harnsäurekristall-Nephropathie zu etablieren und um zu testen, ob Harnsäurekristallgranulome zur CKD-Progression beitragen, und (3) um zu testen, ob eine asymptomatische Hyperurikämie die bereits vorhandene CKD bei Mäusen verschlimmert.

Unsere Fall-Kontroll-Studie hat den starken Zusammenhang zwischen Nierenfibrose und dem Vorhandensein von Nierenmark-Tophi festgestellt. Darüber hinaus wurden mehrere bisher unbekannte Korrelationen wie eine starke Assoziation von Harnsäure Tophi mit Arteriosklerose und Verlust der Podozytenfußfortsätze festgestellt.

Unter Verwendung von leberspezifischen und induzierbaren Glut9 K/O Mäusen wurde ein hyperurikämisches Mausmodell erstellt, das bei Fütterung einer acidogenen Diät mit Inosin-Supplementierung eine kristallinduzierte tubuläre Obstruktion und damit eine Nierenerkrankung mit Entzündung und Fibrose entwickelte. Innerhalb der interstitiellen Fibrose bildeten sich Harnsäure Kristallgranulome.

CKD wurde in hyperurikämischen (Alb-creERT2;*Glut9*$^{lox/lox}$) und normourikämischen (*Glut9*$^{lox/lox}$) Mäusen unter Verwendung von Aristolochinsäure induziert, um festzustellen, ob eine Hyperurikämie ohne Kristallbildung die CKD-Progression antreibt. Es gab keinen Unterschied in der CKD-Progression, gemessen durch eine hochempfindliche transkutane GFR-Messung.

Zusammenfassend kann ich sagen, dass medulläre Gichttophi mit einer ausgedehnten Nierenfibrose assoziiert sind. Wir haben ein Mausmodell für die granulomatöse Harnsäure Nephropathie erstellt und gezeigt, dass die Harnsäurekristall-Nephropathie eine CKD antreibt. Hingegen die asymptomatische Hyperurikämie ohne Kristallurie weder eine CKD verursacht noch zu deren Progression beiträgt.

Summary

Chronic kidney disease (CKD) represents an important global unmet medical need. To a multitude of CKD causes belong the crystalline nephropathies. In this project, the pathogenesis and relevance of chronic uric acid crystal nephropathy were investigated. Chronic uric acid crystal nephropathy (or gouty nephropathy) is defined as the presence of uric acid granulomas in the kideny medulla. This finding is often associated with extensive kidney scarring. However, a few decades ago a number of publications questioned the clinical relevance of gouty nephropathy, and research on the subject has subsequently stagnated. Another controversial research topic is whether hyperuricemia contributes to the progression of CKD. The aim of my project was to re-evaluate medullary tophi: (1) to characterize the histological abnormalities of diagnostic kidney biopsies in a large case-control study, (2) to establish a reliable mouse model for uric acid crystal nephropathy and to test whether uric acid crystal granulomas contribute to CKD progression; and (3) to test whether asymptomatic hyperuricemia aggravates pre-existing CKD in mice.

Our case-control study identified a strong association between kidney fibrosis and the presence of kidney medullary tophi. In addition, several previously unknown correlations such as a strong association of uric acid tophi with arteriosclerosis and loss of podocyte foot processes were found.

Using liver-specific and inducible Glut9 K/O mice, a hyperuricemic mouse model was created which, when fed an acidogenic diet with inosine supplementation, developed crystal-induced tubular obstruction and thus kidney disease with inflammation and fibrosis. Uric acid crystal granulomas formed within the interstitial fibrosis.

CKD was induced in hyperuricemic (Alb-creERT2; Glut9$^{lox/lox}$) and normouricemic (Glut9$^{lox/lox}$) mice using aristolochic acid to determine whether non-crystalline hyperuricemia drives CKD progression. There was no difference in CKD progression as measured by a highly sensitive transcutaneous GFR measurement.

In summary, we concluded that medullary gouty tophi are associated with extensive kidney fibrosis. We created a mouse model of granulomatous uric acid nephropathy and showed that uric acid crystal nephropathy drives CKD. In contrast, asymptomatic hyperuricemia without crystalluria neither causes CKD nor contributes to its progression.

Abbreviations

AA	aristolochic acid
AAI	8-methoxy-6-nitro-phenanthro-(3,4-d)-1,3-dioxolo-5-carboxylic acid
AAII	6-nitro-phenanthro-(3,4-d)-1,3-dioxolo-5-carboxylic acid
AAN	aristolochic acid nephropathy
ABCG2	Apical ATP-binding cassette transporter G2
ACE	angiotensin-converting enzyme
AKI	acute kidney injury, acute kidney injury
AMP	adenosine monophosphate
APRT	adenine phosphoribosyltransferase
AT_1	angiotensin-II-receptor-subtype-I
BEN	balkan endemic nephropathy
C_{Cr}	creatinine clearance
CKD	chronic kidney disease
C_{UA}	UA clearance
CVD	cardiovascular disease
DNA	deoxyribonucleic acid
eGFR	estimated GFR
FEUA	fractional excretion of UA
FSGS	focal segmental glomerulosclerosis
GFR	glomerular filtration rate
GMP	guanosine monophosphate
GWAS	genome wide association study
HD	hemodialysis
HGPRT	hypoxanthine–guanine phosphoribosyltransferase
hNPT4	human sodium phosphate transporter 4
HU	hyperuricemia
IL	interleukin
IMP	inosine monophosphate
KDIGO	Kidney Disease Improving Global Outcomes
K_m	Michaelis constant
KRT	kidney replacement therapy
MRP	multidrug resistance protein

NETs	neutrophil extracellular traps
OAT	organic anion transporter
PAS	Periodic acid-Schiff
P_{Cr}	plasma creatinine
PD	peritoneal dialysis
PRPP	ribose-5-phosphate to phosphoribosyl pyrophosphate
P_{UA}	plasma UA
RAAS	renin-angiotensin-aldosterone system
RNA	ribonucleic acid
SGLT2	sodium dependent glucose co-transporter 2
SLC22A12	solute carrier family 22, member 12
UA	uric acid
U_{Cr}	urine creatinine
ULT	urate lowering therapy
Uox	urate oxidase
U_{UA}	urine UA

1 Introduction

1.1 Chronic Kidney Disease

Chronic kidney disease (CKD) is defined as a change of kidney structure leading to organ dysfunction lasting for a prolonged period. According to the Kidney Disease Improving Global Outcomes (KDIGO) initiative, a person has CKD either if he/she, over a course of at least three months, has a glomerular filtration rate (GFR) below 60 ml/min/1.73 m^2 or if two or more makers of kidney damage (e.g. albuminuria or sediment abnormalities) are present. The KDIGO classifies CKD based on both GFR and severity of albuminuria. Together, these markers are effective tools for predicting CKD outcomes and the likelihood of progression to kidney failure (Table 1) [1].

Table 1. KDIGO classification of CKD
As albuminuria progresses and GFR declines, the risk of progression of GFR increases. The risk of an unfortunate outcome, which includes cardiovascular mortality relatively quantified in this table from 1 to 4 and color coded (green = little to no risk, red = high risk). Modified after [1].

			Albuminuria (mg albumin / g creatinine)		
			<30	33-300	>300
GFR (ml/min/1.73m^2)	>90	G1	1	1	2
	60-89	G2	1	1	2
	45-59	G3a	1	2	3
	30-44	G3b	2	3	3
	15-29	G4	3	3	4
	<15	G5	4	4	4

The average human kidney is composed of around 900,000 nephrons at the time of birth, although there is great interindividual variance. After the development of the kidney is completed, at the 36th week of gestation, no new nephrons are created [2]. The GFR of a single nephron can be calculated by dividing the total GFR by the total number of nephrons. The single-nephron GFR averages around 80 ml/min. An increased single-nephron GFR is associated with glomerular hypertrophy, more glomerulosclerosis and arteriosclerosis [3], and therefore predisposes humans to develop CKD. The

risk of CKD progression displayed in Table 1 can be explained by increases in single-nephron GFR. At the beginning of a kidney disease, the total GFR can be unchanged or even elevated as nephrons increase their single-nephron GFR by hyperfiltration [4]. This causes the glomerular shear stress in these remaining nephrons, which leads to accelerated podocyte loss and secondary focal segmental glomerulosclerosis (FSGS), causing global glomerulosclerosis and augmenting nephron loss. This process is a vicious cycle that leads to the progressive loss of nephrons and the decline of GFR [3]. When many nephrons are lost, CKD progresses to kidney failure. Kidney failure is defined as irreversible kidney failure that requires kidney replacement therapy (KRT), which can come in the form of peritoneal dialysis (PD), hemodialysis (HD), or kidney transplantation [5].

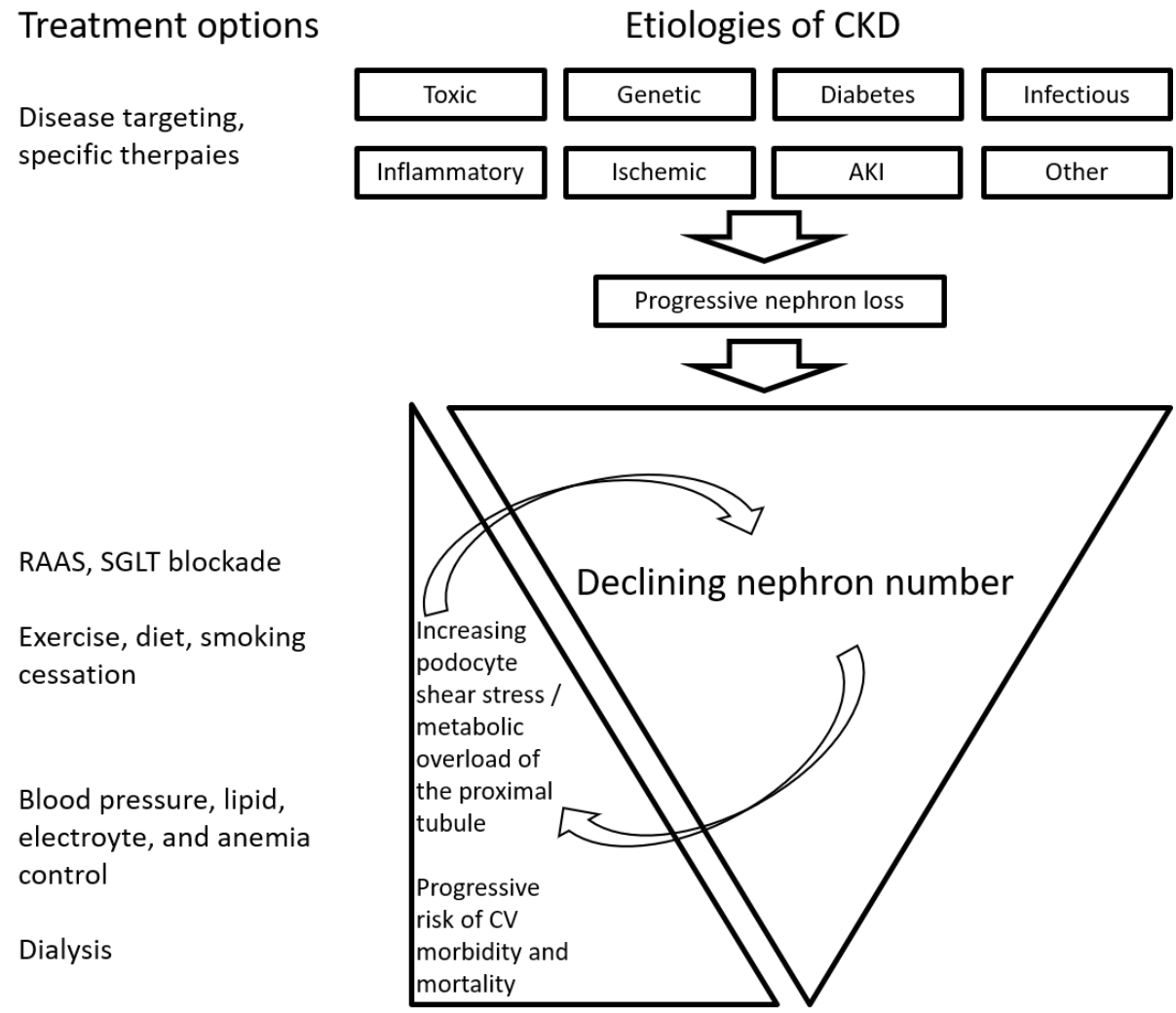

Figure 1. Pathogenesis and therapeutic options of CKD
An underlying disease process sets in motion the cycle of nephron loss, which auto-augments by increasing podocyte shear stress and metabolic overload (leading to dysfunction of the proximal tubule). Various therapeutic options are available at different stages of the process, some of these are listed exemplary on the left. Modified after [6].

CKD can be caused by a range of different underlying diseases (Figure 1). Examples include polycystic kidney disease (genetic), diabetes (metabolic), immune complex glomerulonephritis

(inflammatory/immunologic), bacterial pyelonephritis (infectious), fibromuscular dysplasia (vascular), lead nephropathy (toxic), obstructive nephrolithiasis (mechanical), or multiple myeloma (malignant). CKD can also result after a severe episode of acute kidney injury (AKI), causing irreversible kidney damage and leading to a permanent drop in GFR. Other factors predispose a person for CKD onset and accelerate CKD once it has manifested. These risk factors include obesity, low birth weight, aging, environmental and genetic factors, and pregnancy [4, 7, 8]. Obesity and pregnancy go along with an expansion of blood volume, leading to glomerular shear stress and causing glomerular hypertrophy and elevation of single-nephron GFR [4]. Low birth weight strongly correlates with fewer functioning nephrons at birth [9], leaving remaining nephrons to compensate by elevation of single-nephron GFR and hypertrophy, thus predisposing to CKD.

Clinically, the presentation of CKD varies based on the underlying disease. Initially it is asymptomatic, which often delays diagnosis and treatment. When CKD has progressed, the patient may experience a range of symptoms including weakness from anemia. Once CKD approaches to kidney failure, body homeostasis is severely impaired by persisting kidney failure and a range of different signs and symptoms may appear. Uremic symptoms, which occur late in the disease process, include fatigue, nausea, vomiting, weakness, and anorexia. Signs of advanced kidney disease include arterial hypertension caused by fluid overload and maximum activation of the renin-angiotensin-aldosterone system (RAAS). Electrolyte abnormalities causing cardiac arrhythmia, cognitive impairments, or neuromuscular malfunction are frequently observed in kidney failure. Anemia due to a lack of erythropoietin production or mineral bone disorder due to an impaired vitamin D hormone metabolism are often earlier signs of advancing CKD and presentations of kidney endocrine malfunction. Cardiovascular disease (CVD) is the main cause of mortality in patients with kidney failure and CKD [4].

Screening for CKD may be performed by measuring proteinuria and serum creatinine, which can be used to calculate the estimated GFR (eGFR). When screening yields a pathological finding, a cause must be determined. Here, the nephrologist will take a patient history and do a physical examination, additionally a large diagnostic repertoire is available including laboratory test, imaging, genetic testing, microscopy of the urinary sediment, and kidney biopsy to secure the underlying diagnosis. The determined underlying disease must then be treated to halt the progression of CKD.

CKD treatment usually consists of specific medication of the underlying disease and general treatment approaches to slow CKD progression or prevent or treat CKD complications. For example, a patient with diabetic nephropathy will not only receive standard care for diabetes to control blood sugar like insulin and non-insulin anti-diabetic drugs but may also receive an SGLT2 inhibitor. This drug not only lowers blood glucose by stimulating kidney glucose excretion; it also lowers renin secretion by the

macula densa and decreases the glomerular filtration pressure, amplifying its nephroprotective effect in diabetic nephropathy [10, 11]. A recent study has shown that SGLT2 inhibition is also effective in CKD treatment of patients without diabetes [12]. General approaches to treating CKD that prevent further nephron loss by lowering single-nephron GFR and preventing CKD complications are applied regardless of the underlying kidney disease. RAAS blockade has been established as a cornerstone of CKD treatment. RAAS is responsible for the regulation of blood pressure and glomerular filtration pressure. In CKD, RAAS is overactive leading to arterial hypertension and glomerular hyperfiltration. This causes podocyte barotrauma and proteinuria with subsequent podocyte loss and leads to advancement of CKD by acceleration of nephron loss. Blockade of RAAS, either by inhibition of the angiotensin-converting enzyme (ACE) or by blockade of the angiotensin-II-receptor-subtype-I (AT_1), leads to systemic vasorelaxation and causes normalization of arterial hypertension but also causes a reduction of glomerular filtration pressure and a decrease of single-nephron GFR by dilatating the efferent arteriole of the glomerulus. Another essential effect of RAAS inhibition seems to be the relief of the metabolic strain on the proximal tubule and a reduction of hyper-reabsorption (Figure 1) [6]. Therefore, RAAS inhibitors are used to break the vicious cycle described earlier and have been shown to have nephron-protective effects that can halt or slow the progression of CKD [13]. In Alport syndrome and diabetic nephropathy, treatment with RAAS blockade has been shown to be most effective when initiated as early as possible [14, 15]. Reducing protein and salt intake, controlling obesity, hypertension and dyslipidemia have also been shown to slow progression of CKD and diminish risk of kidney failure [16].

Once kidney failure has set in, KRT must be started to further prolong the life of the patient. The most frequently used form of KRT is hemodialysis. The blood is accessed either by arteriovenous fistula, arteriovenous graft, or by placing a central venous dialysis catheter. The blood is then flown in the opposite direction of the dialysate, separated by a semipermeable membrane. Blood waste products diffuse across this membrane into the dialysate. Another option for KRT is peritoneal dialysis; here the dialysate is pumped straight into the peritoneal cavity by a catheter and blood waste products diffuse across the peritoneum into the dialysate. The dialysate is drained after an osmotic equilibrium has set in. The third option is a kidney transplantation. Dead and living kidney donations can be performed. Transplantation is the option with the best prognostic benefit for the patient, however, it is limited by organ availability [17].

The European prevalence of CKD ranges from 3.31% in Norway to 17.3% in northeast Germany [18]. Within the Latin American population in the United State there is also great variability of CKD prevalence, ranging from 7.4% in South American women (11.2% in South American men) to 16.6 in Puerto Rican women (16.0% in “other” Latinos); the total Latino/Hispanic prevalence of CKD is 13.7 for women (15.3% for men) [19]. The prevalence of kidney failure is highest in Taiwan with over 2500 per

million population (ppm) and lowest in the African countries of Senegal and Ghana [20]. The variance of CKD and kidney failure prevalence are likely caused by different environmental and genetic factors. In 2010, CKD was ranked 18th most frequent cause of death in the global burden of disease study, it is up from 27th place in 1990 [21]. Economically, CKD also poses a large burden. CKD and kidney failure are challenges for large scale economic systems; CKD and kidney failure cost a total of 4,659 million Euros in 2015 in Germany [22]. This is evidence that there is a vast unmet medical need in CKD and that research is needed to further understand CKD and its pathophysiology to develop improved treatment and preventative modalities.

1.1.1 Aristolochic acid nephropathy

One etiology of CKD relevant to this project is aristolochic acid nephropathy (AAN). Aristolochic acid (AA) is an herbal compound that can be found in *Aristolochia fangchi* or *Aristolochia clematitis* and has been responsible in the past for several regional outbreaks of nephropathy. AA was used in the past in Chinese herbal medicine to treat many different types of diseases like hepatitis, stroke, or pneumonia [23]. In the 1990s several Belgian women consumed 'slimming' medicinal tinctures containing AA and were found to have rapid progressive fibrosing interstitial nephritis [24], in some cases requiring kidney transplantation. Many patients with AA nephropathy later went on to develop urothelial malignancies [25], prompting the WHO to declare AA a class I human carcinogen [26].

Long-term, small-dose exposure to AA was later declared the cause of the Balkan Endemic Nephropathy (BEN) that was first described in the 1920s. Contamination of wheat flour by *Aristolochia clematitis,* an herb that's commonly found in Balkan wheat fields was described by Ivic in 1969 [27] as a possible cause for continuous environmental exposure to AA. In endemic areas of eastern Europe, BEN is responsible for 70% of kidney failure [28]. Although prevalence BEN or AAN peaks in regions where members of the *Aristolochia* plant are at home, evidence suggests that AAN is a global problem and presents a great unmet medical need [28, 29].

AA is a mix of two structurally similar nitrophenanthrene carboxylic acids: 8-methoxy-6-nitro-phenanthro-(3,4-d)-1,3-dioxolo-5-carboxylic acid (AAI) and 6-nitro-phenanthro-(3,4-d)-1,3-dioxolo-5-carboxylic acid (AAII) [30]. AAI and AAII undergo redox reactions and their reduced forms form covalent adducts with DNA. This blocks mRNA transcription and DNA replication, leading to cell cycle arrest and p-53 dependent cell death [31]. This mechanism likely explains the observed tubular necrosis in AAN. It is not known why the kidney is primarily affected. Similarly, the mutagenic potential explains the compounds propensity to cause urothelial carcinoma.

The clinical presentation of AAN includes kidney insufficiency, anemia, erythrocytes and leukocytes in the urinary sediment and mild proteinuria. Kidney ultrasound reveals shrunken kidneys. The

histological findings are massive interstitial fibrosis and associated tubular atrophy, tubular necrosis, hyperplasia of arteriolar walls, and few interstitial inflammatory cells [23]. Around 40% of patients also present with urothelial carcinoma in situ [32]. Phytochemical analysis can confirm intake of AA and DNA adduct analysis can be used to confirm the presence of AA DNA adducts in biopsied kidney or urothelial tissue [23].

Treatment options of AAN are greatly limited. Individual reports have observed altered disease courses under steroid therapy [33, 34]. Beyond steroids, general management of CKD and kidney failure, including KRT, is indicated. Patients should be regularly screened for urothelial malignancies.

AA is used in an experimental setting to induce CKD in mice [35]. It models the effects of AAN in human and is a simple and fast way to induce kidney fibrosis in mice.

1.2 Uric Acid Metabolism

Uric acid (UA) is the end-product of the purine metabolism. It is a weak diprotic organic acid with a pKa1 ≈ 5.4 and pKa_2 ≈ 10.3. At the human physiological blood pH of 7.4, 1% is found as the electrically neutral UA and 99% of it is deprotonated once and present as the monovalent urate anion [36]. Biochemical literature uses the two terms *urate* and *uric acid* interchangeably for all protonation states. UA as bivalent anion is almost nonexistent in humans, due to its very basic pKa_2. UA has a solubility limit of about 7 mg/dl under physiological conditions (pH of 7.4, 37 °C). For this reason, blood UA concentrations above 7 mg/dl are considered hyperuricemic (varying slightly depending on the measuring laboratory and between men and women). The electrically neutral, undeprotonated UA has a much lower solubility limit, predisposing for crystal formation in acidic environments like urine.

Higher primates, including humans, have lost function of the hepatic uricase, an enzyme used by most other animals including rodents to degrade UA into the more water-soluble allantoin. This leads to higher serum UA levels in higher primates and humans compared to lower mammals. In normouricemic humans, the concentration of serum UA is close to its solubility limit, predisposing humans to precipitation of UA crystals in the tissue, and therefore to all UA crystal-related pathologies.

1.2.1 Synthesis and Degradation of Purines

De novo purine synthesis begins with ribose-5-phospahte, which is created in the pentose phosphate pathway, a sugar metabolism pathway. The phosphoribosyl pyrophosphate synthetase converts ribose-5-phosphate to phosphoribosyl pyrophosphate (PRPP) [37]. PRPP is enzymatically converted, over various intermediary products, into inosine monophosphate (IMP), which in turn is converted to guanosine monophosphate (GMP) or adenosine monophosphate (AMP), that make up the building blocks of deoxyribonucleic acid (DNA) and ribonucleic acid (RNA) together with the nucleotides of

pyrimidine bases thymine, cytosine, and, uracil. In the first step of AMP degradation, AMP is converted into IMP and then into hypoxanthine by the purine nucleoside phosphorylase [38]. Hypoxanthine is oxidized to xanthine by the xanthine oxidase. The metabolic pathway of GMP degradation merges into xanthine over guanosine and guanin. Xanthine is further oxidized to UA by the xanthine oxidase, ending the degradation pathway of purines in humans because of the missing urate oxidase (uricase). Figure 2 gives a detailed overview of the degradation of purines to UA. There is a salvage pathway for guanine and hypoxanthine, which can be recycled into GMP and IMP by the hypoxanthine–guanine phosphoribosyltransferase (HGPRT). A mutation in the gene encoding for the HGPRT causes Lesch–Nyhan syndrome, which is characterized by hyperuricemia with gout, reduced intellect, and self-mutilating behavior [39]. The adenine phosphoribosyltransferase (APRT) catalyzes the salvage pathway for adenine, recycling it to AMP. A deficiency of APRT leads to accumulation of 2,8-Dihydroxyadenine, a byproduct of the adenine metabolism, causing 2,8-Dihydroxyadenine nephrolithiasis and crystalline nephropathy [40].

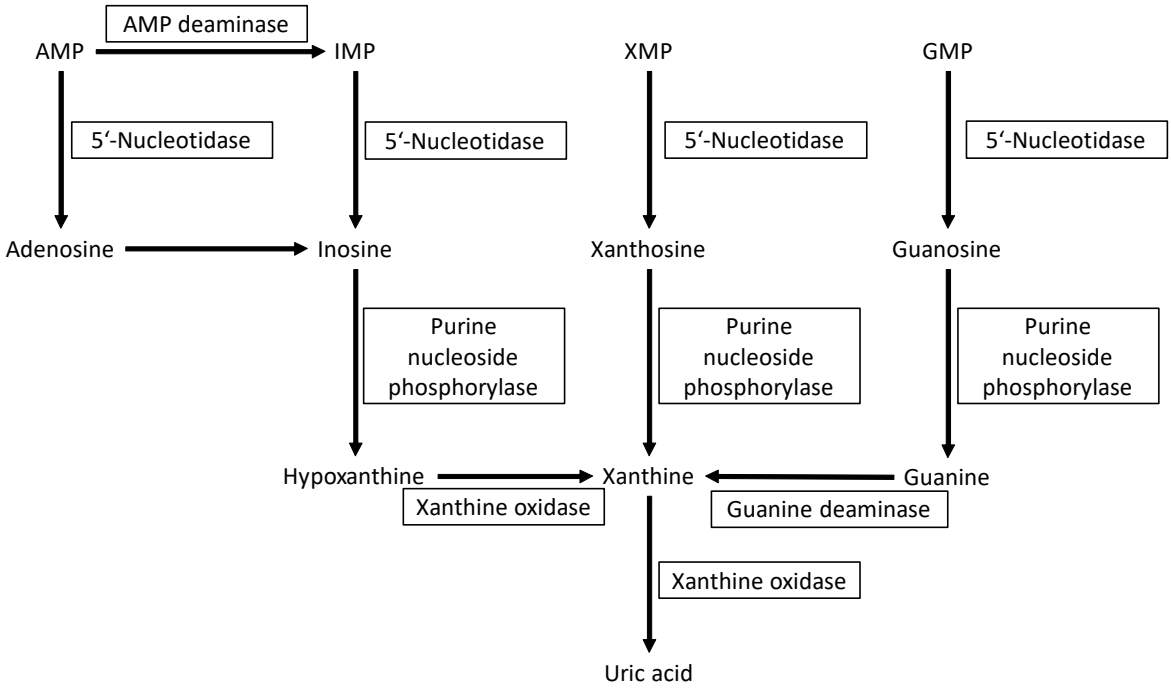

Figure 2. Uric acid synthesis
The degradation pathway of purines begins with the purine monophosphates. AMP is converted to IMP via the AMP deaminase. All purine monophosphates are dephosphorylated by the 5'-nuclotidase. The resulting nucleosides are further degraded by the purine nucleoside phosphorylase. This enzyme degrades the nucleosides to into their corresponding bases. The bases are enzymatically converted to xanthine, which is oxidized by the xanthine oxidase into UA. Modified after [41].

1.2.2 Elimination of UA

Humans and other mammals rely on urea, not UA for the excretion of nitrogen. Birds and snakes, however, with a fractional excretion of UA greater than 100%, use UA as primary vehicle for the elimination of nitrogen, demonstrating vast differences in the kidney handling of UA between animals [36]. UA is eliminated by the kidney through the urine or by the gut. The gut eliminates about 25 to 33% of the total UA [42]. Here, UA is secreted into the intestinal lumen, where it is degraded to allantoin by colonic bacteria.

1.2.3 Kidney Excretion of UA

The kidney is responsible for the elimination of the rest of the UA (75 to 66%) in humans and the kidney handling of UA is decidedly more complex. The fractional excretion of UA (FEUA) is approximately equal to the ratio of UA clearance (C_{UA}) and to the ratio of creatinine clearance (C_{Cr}), which are calculated using plasma and urine UA (P_{UA}, U_{UA}) and creatinine concentrations (P_{Cr}, U_{Cr}), therefore: $FEUA = C_{UA}/C_{Cr} \times 100\% = [(U_{UA} \times \text{urine sample volume})/ P_{UA}]/[(U_{Cr} \times \text{urine sample volume})/P_{Cr}] \times 100\% = (U_{UA} \times P_{Cr})/(P_{UA} \times U_{Cr}) \times 100\%$. This formula assumes that creatinine has a fractional excretion of 100% and is therefore neither absorbed nor filtered by the human kidney tubule. The FEUA is around 10% in adults, meaning that 10% of the filtered UA is excreted by the urine and 90% is reabsorbed into the bloodstream [43]. Infants have the highest FEUA at around 27%, declining to a mean of FEUA in childhood around 8% despite rising serum urate levels and therefore increased UA glomerular filtration [44-46].

UA has a molecular weight of 163.1 Dalton, therefore passing the glomerular filter unhindered. It is evident that if kidney FEUA is below 100%, there needs to be a tubular reabsorption of UA. In 1959, A. Gutman et. al. found evidence of tubular secretion of urate [47], therefore setting up a three-component system for kidney handling of UA: filtration, reabsorption, and secretion [48]. Evidence for postsecretory reabsorption was found 14 years later in a study of humans, where subjects received treatment with probenecid or sulfinpyrazone at a low dose compared to a high dose (both uricosuric agents that block kidney urate reabsorption [49, 50]), leading to an apparent increase of UA secretion as measured by a greater decrease of uricosuria after administration of pyrazinamide or low-dose aspirin (both thought to inhibit tubular secretion of UA [51, 52]). The authors concluded that this finding is more compatible with a partial reabsorption distal to the secretory site of UA in the tubule [53]. This led to the formation of the “classical” model of kidney UA excretion: 1st glomerular filtration of urate; 2nd presecretory reabsorption in S1 segment of the proximal convoluted tubule, where about 99% of the filtered UA is reabsorbed; 3rd secretion in the S2 segment 50% of the reabsorbed UA is secreted back into the tubular lumen; and 4th postsecretory reabsorption in the S3 segment, where 80% of the secreted UA undergoes post-secretory reabsorption [54], leaving a FEUA of around 10%.

Figure 3 gives an overview of nephron anatomy for orientation. Newer research has amended the strict order and segment-based placement of reabsorption and secretion that is described in the classical model and has shown that reabsorption and secretion via urate transporters can take place in the same part of the proximal kidney tubule [55]. The cause of hyperuricemia in patients taking the tuberculostatic medication pyrazinamide has also been revised by more recent research suggesting that it is at least in part explained by stimulation of urate reabsorption as opposed to only the inhibition of urate secretion [56, 57], therefore amending previous research that was crucial to the establishment of the classical model that assumed an effect of pyrazinamide only on tubular urate secretion.

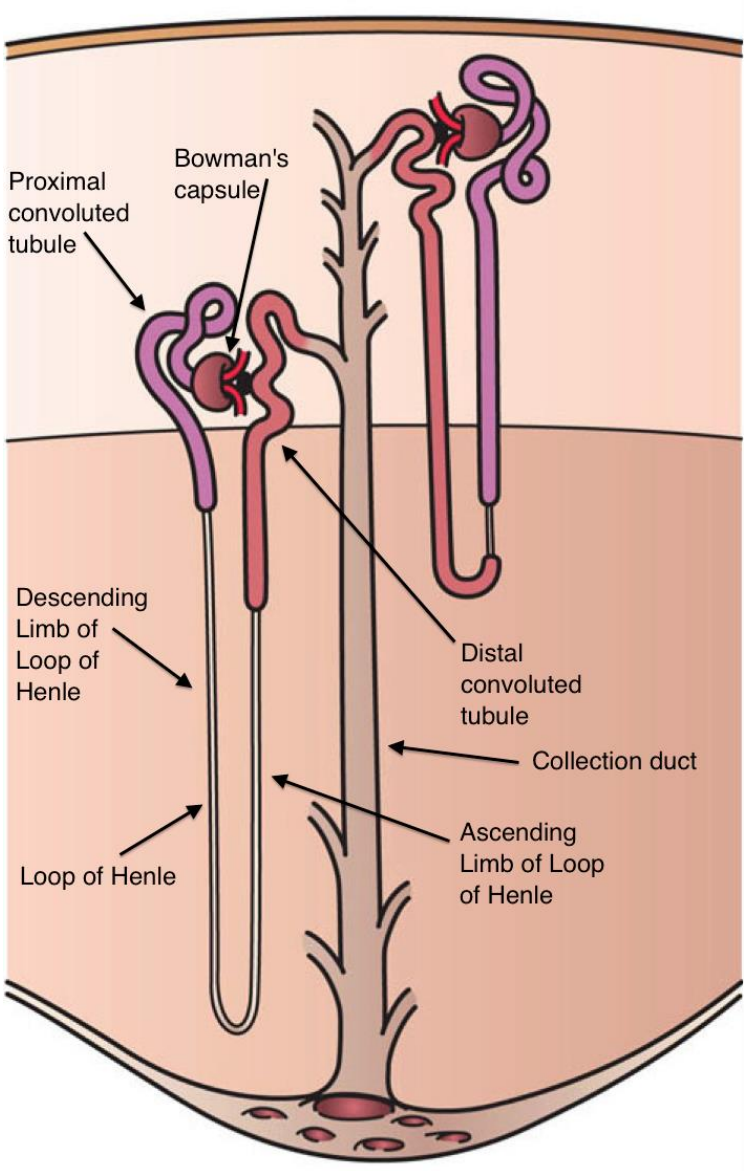

Figure 3. Nephron anatomy
A schematic overview of nephron anatomy is shown. The glomerulus is responsible for the filtration of blood into the Bowman's capsule, forming the "glomerular filtrate". This liquid is conducted into the proximal convoluted tubule, where the S1 and part of the S2 segment sits. The S2 segment extends into the straight proximal tubule (thick descending limb of the loop of Henle), leading into the S3 segment. The filtrate then passes into the thin descending limb and thin ascending limb of the loop Henle, the thick ascending limb, the distal convoluted tubule, and finally into the collecting duct. Generic license Artwork by Holly Fischer [58].

1.2.4 Kidney Urate Transporters

URAT1

URAT1, discovered in 2002, was the first kidney urate channel to be identified [57]. It is encoded by the SLC22A12 (solute carrier family 22, member 12) gene and part of the organic anion transporter (OAT) family. It is expressed in humans at the brush border (luminal) of human kidney tubular epithelium and responsible for UA reabsorption. Genome wide association analyses identified an association between serum UA levels and sequence variation of the SLC22A12 gene [59], providing further evidence for the role of URAT1 in UA metabolism. First functional studies were performed by cloning it into *Xenopus* oocytes; here, it was shown to take up UA in exchange for Cl^- or organic anions (antiuricosuric agents like pyrazinamide, lactate, aspirin serve as substrates for URAT1, increasing UA reabsorption) with a Michaelis constant (K_m) of 371 ± 28mM it is a target of benzbromarone and probenecid, the most commonly used uricosuric gout medication. Evidence for its importance in tubular reabsorption of urate was provided by the identification of congenital SLC22A12 loss of function mutation as the cause of renal hypouricemia in Japanese patients [57, 60-62]. These patients have an FEUA of 30-90% and suffer from nephrolithiasis and exercise-induced acute kidney failure [63]. Although their FEUA is much higher than that of healthy individuals, there is still net rest-reabsorption of UA even in patients with homozygous loss of function URAT1, meaning that URAT1 cannot be the only apical kidney transporter responsible for UA reabsorption.

GLUT9

The SLC2A9 gene, coding for GLUT9, was identified as having a cDNA sequence corresponding to a member of the human glucose transporter (GLUT) family. It was first cloned in 2000 and identified to have 12 transmembrane domains [64], similar to other transporters of this family. It is present in two splice variants that have distinct expression patterns: GLUT9 (aka GLUT9a), which is expressed in kidney, liver, placenta, and leukocytes, whereas GLUT9ΔN (aka GLUT9b) is only expressed in kidney and placenta [65]. In polarized Madin-Darby canine kidney cells GLUT9a was found in the basolateral membrane, whereas GLUT9b in the apical membrane. GLUT9 has a low affinity for deoxyglucose and it was not until 2007 that a role for UA handling was suggested for GLUT9 by genome wide association studies (GWAS) of two cohorts in Sardinia and Chianti [66]. Subsequent GWAS confirmed this association in other cohorts [67-69] and its heterologous expression in Xenopus laevis oocytes showed a strong UA transport activity of GLUT9. GLUT9 is a voltage dependent uniporter of UA and does not depend on the Na^+ transmembrane gradient [70]. It was shown that homozygous loss of function mutations of the SLC2A9 gene causes kidney hypouricemia with FEUA of 100% or higher (net secretion)

and a phenotype of UA nephrolithiasis and exercise-induced acute kidney failure [71-73]; it has also been described to cause posterior reversible encephalopathy syndrome [74]. Heterozygous loss of function mutation leads to a less pronounced phenotype of hyperuricosuria and renal hypouricemia [75-77]. Together, these findings suggest that GLUT9a is possibly the only tubular basolateral transporter for UA, while the apical GLUT9b has been hypothesized to play a role in tubular UA secretion and reabsorption, although its exact function remains to be elucidated.

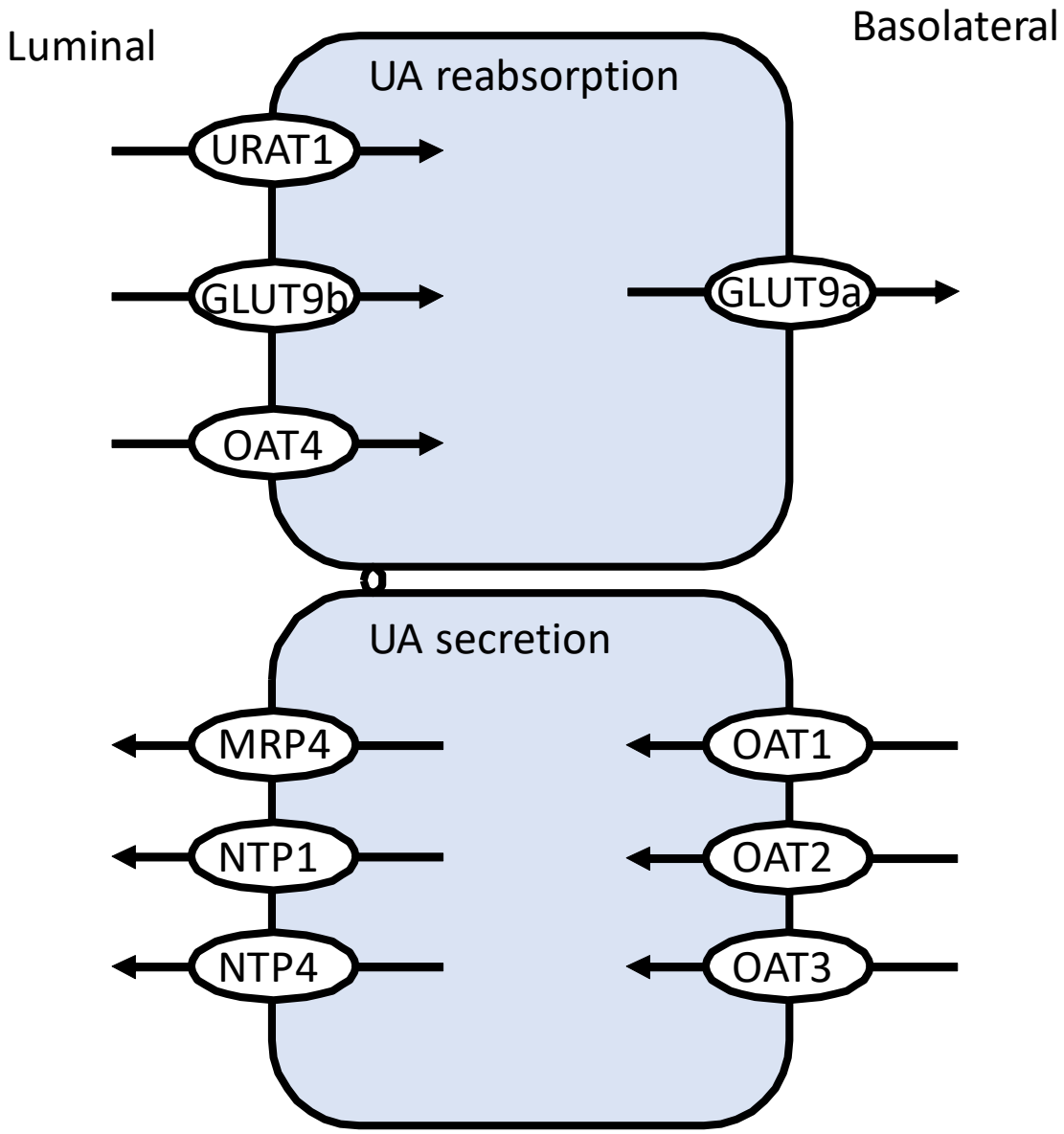

Figure 4. Transporters involved in tubular reabsorption and secretion of UA.
Pictured schematically are UA transporters of epithelial cells in the proximal tubule with the arrows indicating the direction of UA movement. UA reabsorption is performed on the apical (luminal) tubular membrane GLUT9b, URAT1, and, to a lesser extent, OAT4. GLUT9a is most likely the only reabsorption transporter for UA on the basolateral side of the tubular cell. A range of UA transporters have been shown or are hypothesized to play a role in UA secretion, including OAT1,2, and 3, MRP4, NTP 1 and 4.

Other kidney UA Transporters

A range of other UA transporters have been descried in the literature, however, the level of evidence for their roles in kidney handling of UA remains less than for GLUT9 and URAT1.

Other members of the OAT family have been shown to transport UA and are expressed in kidney tubular epithelium. OAT4 is an apical transporter of the proximal tubule and has been associated with hyperuricemia and gout in different GWAS [78-81]. It is sequentially similar to URAT1 and transports UA at a lower affinity. A study found that a variant of OAT4 leads to underexcretion of UA and predisposes patients to develop gout [82], which highlights its role in kidney UA handling. OAT10 was shown to transport UA at a very low affinity [83] but GWAS have not been able to show an association with gout or hyperuricemia for this transporter [59].

A range of different transporters have been postulated to potentially play a role in tubular secretion of UA. Multidrug resistance protein (MRP) 4, Apical ATP-binding cassette transporter G2 (ABCG2), human sodium phosphate transporter 4 (hNPT4/SLC17A3), NPT1 (SLC17A1), and Type 1 sodium-dependent phosphate transporter (SLC17A1 Protein) have all been shown to transport UA *in vitro* and are present on the apical side of human tubular cells [84-87]. ABCG2, NPT1, and NPT4 have been associated with hyperuricemia and gout in GWAS [59, 67, 80, 81]. OAT1, OAT2, and OAT3 are expressed basolaterally and have been hypothesized to play a role in tubular secretion by transporting urate from the kidney interstitium into the tubular epithelium [88]. Evidence for the role of these secretory transporters *in vivo* remains weak and pending further investigation. Figure 4 shows the function of each UA transporter in a tubular cell.

1.3 Gout

Gout is an inflammatory form of arthritis caused by the deposition of monosodium urate (MSU) crystals within joints and soft tissues. The deposition of MSU crystals is caused by pathologically elevated serum UA levels, called hyperuricemia.

The precipitation of MSU crystals triggering acute inflammation of the affected joint is called acute articular gout. Most commonly affected is the base joint of the big toe, a manifestation of gout called podagra. Advanced gout usually presents many years after initial onset of symptoms. Here, persisting UA crystals cause chronic inflammation, leading to the formation of granulomas around the crystal. This granuloma, in the case of gout, is called tophus. Within the tophus, both pro- and anti-inflammatory cytokines are excreted, leading to a state of low-level chronic inflammation [89]. Histologically, larger crystal masses are surrounded by layers of epithelioid mononuclear cells and foreign-body giant cells (fused macrophages, another hallmark of tophi). The tophus is encapsulated by surrounding fibrosis. Together, the inflammatory reaction and fibrosis around the tophus shield the

surrounding tissue from crystals and vice versa. Articular tophi can lead to bone destruction, loss of joint function, and joint disfigurement [90]. The morphology of articular gouty tophi is identical to the kidney UA tophi (see section 1.5.2).

The rate of gout is higher among men (3-6%) than among women (1-2%) [91]. The total incidence in the 2000s is 2-68 per 1000 person/year. Gout is more likely with higher age [91]. Significant comorbid disorders include hypertension (74%), CKD stage II or higher (71%), obesity (53%), diabetes (26%), and a history of myocardial infarction (14%) and stroke (10%) [92]. Risk of death in patients with gout is also increased, usually due to cardiovascular disease [93]. Whether or not the increased prevalence of these comorbid conditions is causally attributed to hyperuricemia or gout has been difficult to prove due to many potential confounding factors. However, some evidence suggests that hyperuricemia and gout directly contribute to worse outcomes in CKD and cardiovascular disease [94-96].

1.4 Hyperuricemia

There are a few useful physiological properties of UA making it likely that humans have garnered an evolutionary benefit by loss of uricase function, resulting in higher blood urate levels. One such property is its antioxidant function. It was shown that soluble UA (sUA) can reduce the oxo heme oxidant formed in the oxidation of hemoglobin with peroxide and can protect erythrocytes from lysis due to peroxidative damage. UA is also a powerful scavenger of hydroxy, singlet oxygen, and peroxyl radicals [97]. UA is therefore hypothesized to cause lengthening of lifespan due to protective mechanisms against oxygen radicals, decreasing incidence of cancer [97]. Early humanoids lost the function of the L-gulonolactone oxidase, the enzyme responsible for the production of ascorbic acid (Vitamin C), thus increasing selection pressure to find an alternative antioxidant and setting the stage for the loss of uricase function. *In vivo* data has shown significant reduction of ischemic changes in a rat model of cerebral artery occlusion when animals were treated with serum UA compared to placebo [98]. A mouse model of multiple sclerosis (MS) showed a strong, dose-dependent, therapeutic effect of UA. The same study showed a significantly lower level of serum UA in patients with MS compared to controls and that patients with both gout and MS were significantly less frequent in a large cohort of MS and gout than predicted mathematically [99]. The authors of both studies ascribed their findings to the antioxidant properties of sUA.

Other research, contrarily, has found that sUA, under certain conditions, also has radical oxidative properties [100-102]. When oxidized, sUA does not always turn into its neutral redox partner allantoin but also into radicals like the aminocarbonyl radical, which can amplify oxidation of LDL liposomes by peroxynitrate [103], possibly aiding in the pathogenesis of arteriosclerosis and adding to the oxidative burden within the organism. Another study found that intracellular sUA can induce mitochondrial

dysfunction, which can stimulate NADPH oxidases, leading to endothelial dysfunction and possibly aiding in the pathogenesis of hypertension and vascular disease [104]. Hyperuricemia is epidemiological closely correlated to diseases with a high oxidative burden such as metabolic syndrome, arteriosclerosis, obesity, and hypertension. A randomized placebo-controlled clinical trial found that serum UA levels independently predict cardiovascular events in patients with isolated systolic hypertension [105]. This paradox could be explained as a counterregulatory measure of the body, increasing serum UA levels to deal with a higher oxidative stress. In contrast, hyperuricemia could also be a causative agent in the pathogenesis of these diseases. Mouse models of hyperuricemia have also produced conflicting data. A study using an inducible, liver-specific Glut9-KO murine model of hyperuricemia found no evidence of hypertension after 6 months of an average serum UA of 300 µmol/l [106]. A more recent study using urate oxidase (Uox) knockout mice found development of hypertension and aberrant fat metabolism in female mice and decreased glucose tolerance in male mice [107]. It should be noted, however, that serum UA in the second study was much higher (above 460 µmol/l, a level that is considered hyperuricemic even for humans), that only 40% of the mice survived up to 62 weeks, and that the development of hypertension in the Uox-KO mice could also be explained by a higher level of kidney damage secondary to hyperuricemia. More research is needed to clarify, which properties (antioxidant or oxidant) of sUA overweighs and therefore whether sUA plays a protective or a detrimental role in human metabolism.

Another theory seeking to explain an evolutionary advantage behind the loss of uricase function considers its dependent anti-natriuretic and therefore blood pressure elevating effects, that was observed in a hyperuricemic rat model [108]. Loss of uricase function happened at a time of low sodium availability for humans, and sUA is postulated to maintain blood pressure levels to compensate for dietary sodium deficiencies [108, 109]. Evidence that asymptomatic hyperuricemia leads to increased blood pressure was also provided in an interventional study of hyperuricemic adolescents, where a decrease in blood pressure was observed after treatment with allopurinol was initiated [110]. However, this study is limited by a range of factors including a low number of study subjects (n=30) and further research is needed to establish this causality. If true, however, this second theory explains an evolutionary benefit of sUA in times of low dietary sodium availability in maintaining blood pressure and at the same time its propensity to cause morbidity due to hypertension in times of dietary sodium abundance, as is the case today.

1.4.1 Hyperuricemia in gout

In lower mammals, with retained uricase function, serum UA concentrations never approach the solubility limit. In humans, however, the missing uricase genetically predisposes to hyperuricemia and the precipitation of monosodium UA crystals. The joints are especially predisposed because they are a

bradytroph tissue, with a lower pH and temperature, all of which further increases the likelihood of UA precipitation. The crystals elicit an acute inflammation by triggering NLRP3 inflammasome activation and subsequent secretion of interleukin (IL)-1β [111], leading to leucocyte recruitment, neutrophil activation, and painful inflammation. This is the pathophysiology of acute gouty arthritis. Inflammation is finally resolved by aggregation of neutrophil extracellular traps (NETs), phagocytosis of apoptotic neutrophils by macrophages and release of anti-inflammatory cytokines [112].

The causal relation between hyperuricemia and gout is unquestioned in the literature. In 1859, Alfred Garrod showed in his now legendary publication “The nature and treatment of gout and rheumatic gout” that “the deposited urate of soda may be looked upon as the cause, and not the effect, of the gouty inflammation” [113]. Garrod also developed the first semi-quantitative test for UA in the blood and urine [114]. Much later, in 1963, allopurinol was developed and it was shown that xanthine oxidase inhibition lowers serum UA and effectively prevents gout [115].

Management of gout is based on two different principles: treatment of the acute inflammatory flare and urate-lowering, prophylactic, therapy. In the acute flare, non-steroidal anti-inflammatory drugs (NSAIDs), colchicine, and glucocorticoids are used to aid resolution of inflammation. If the patient has more than one flare per year, tophi, CKD stage 2 or higher, or kidney stones, urate-lowering therapy is indicated [116]. Medication of choice are usually xanthine oxidase inhibitors like allopurinol or febuxostat, but uricosuric agents (via blockade of URAT1 in the kidney) are alternatives. It is important to mention that a rapid initiation of urate-lowering therapy has been described to induce acute flares [117] and anti-inflammatory therapy is recommended as prophylaxis during the first six months of uricostatic therapy.

1.4.2 Hyperuricemia in CKD

Hyperuricemia and CKD are epidemiologically closely related, and many studies aim to elucidate, which of the two causes the other. A lot of these studies aim to devise the role of asymptomatic hyperuricemia in CKD using regression models.

As CKD progresses, there is less kidney elimination of UA, causing serum UA levels to rise. By the time kidney failure is reached and dialysis is initiated, nearly all patients are hyperuricemic [118]. More complex is the question whether hyperuricemia in turn causes or leads to the progression of CKD. Studies of patients with preexisting CKD have found that hyperuricemia does not independently predict its progression [119, 120]. This finding can possibly be explained by the fact that CKD leads to water and sodium retention, therefore causing vascular disease and CKD progression independently and to a greater degree than hyperuricemia alone [121]. Support for this hypothesis comes from several large studies of patients with normal kidney function that have shown hyperuricemia to

independently predict development of CKD and kidney failure [122-124]. Hyperuricemia has also been shown to independently predict progression of CKD in patients with diabetic nephropathy and Ig-A nephropathy [125, 126]. It can be said that hyperuricemia consistently predicts the development but not the progression of CKD. As patients reach kidney failure, there is a J-shaped mortality in patients, as high and low UA levels are associated with a bad outcome [118, 127].

Hyperuricemia is associated with obesity, metabolic syndrome, and insulin resistance [128]. Hypertension has also been shown to cause hyperuricemia by producing kidney vascular constriction, leading to kidney nitrogen retention [129]. This could be an explanation for the observation that hyperuricemia often presents before CKD onset. Others have argued that hyperuricemia can precede these conditions, [121] leading to the same chicken and egg dilemma so frequently encountered when studying hyperuricemia. A high fructose diet and the excessive consumption of meat and beer are also associated with hyperuricemia [130]. Studies have shown that feeding of a high fructose diet can induce features of metabolic syndrome in rats like hyperinsulinemia, hypertension, hyperlipidemia, and hyperuricemia and that administration of allopurinol, febuxostat, or benzbromarone prophylactically prevents hyperinsulinemia [131, 132].

Intoxication of lead blocks kidney excretion of UA, leading to hyperuricemia [133]. Lead exposure, especially long term, low level lead intoxication strongly correlates with CKD [134]. Animal models with preexisting CKD have shown augmentation of kidney disease upon lead intoxication. After administration of allopurinol, a reduction of hypertension was observed in these animals [135].

Another technique to approach the chicken and egg problem concerning hyperuricemia and CKD is to use interventional studies with urate-lowering medication. A study of 54 hyperuricemic patients with CKD found that allopurinol preserved kidney function over the course of 12 months compared to controls, where kidney function deteriorated [136]. Likewise, a study of 113 patients with a GFR below 60 ml/min showed a slow of progression of CKD when treated with 100 mg of allopurinol daily [137]. Another study of patients with diabetic nephropathy secondary to Type II Diabetes showed a reduction of proteinuria after 4 months of allopurinol therapy [138]. A meta-analysis of 11 studies with a total of 753 patients showed that UA lowering therapy leads to a decrease in serum creatinine and an increase of GFR [139]. Another study of 7629 patients showed that hyperuricemia correlated with a falling GFR and an increase in cardiovascular events [140].

Much of the above presented research implies a harmful role of hyperuricemia in cardiovascular and kidney disease. Citing many of these studies, a review by Johnson et. al plead for more clinical trials studying the effect of uricostatic therapy on the progression of CKD or CVD [121]. However, whether asymptomatic hyperuricemia leads to progression of CKD remains to be elucidated. Presently, medical

guidelines do not recommend uricostatic therapy of asymptomatic hyperuricemia, even in patients with CKD.

1.5 Uric acid crystal nephropathy

Two different types of UA crystal nephropathy have been defined in the literature: acute and chronic UA crystal nephropathy. Acute UA crystal nephropathy is caused by acute massive hyperuricemia, as seen in patients with tumor lysis or crush syndrome. Here, the massive decay of cells causes the release of high quantities of UA into the bloodstream. The UA is filtered in the glomerulus and concentrated by the tubule after fluid reabsorption, causing UA to exceed its solubility and precipitates out, leading to tubular occlusion and acute kidney injury. Chronic UA crystal nephropathy is a pathological diagnosis that is usually made incidentally on kidney biopsy. Its hallmarks on light microscopy are medullary UA tophi. These tophi consist of central needle shaped clefts that are left behind by the crystal after it is dissolved out during tissue fixation and surrounding mononuclear inflammatory infiltrate embedded in fibrosis [141].

1.5.1 Acute uric acid crystal nephropathy (in tumor lysis or crush syndrome)

One of the most common medical emergencies in tumor patients, especially in patients with hematologic malignancies, is the tumor lysis syndrome. This occurs when large amounts of malignant cells undergo lysis, often due to cytostatic therapy, and intracellular content is released into the bloodstream. The Cairo and Bishop system is used to classify the tumor lysis syndrome based on metabolic laboratory findings and clinical findings [142]. Two or more of the following laboratory abnormalities are required to complete the criteria for laboratory tumor lysis syndrome: hyperkalemia, hyperphosphatemia, hyperuricemia, and hypocalcemia. Clinical tumor lysis syndrome is defined as laboratory tumor lysis syndrome plus seizures, increased serum creatinine, cardiac arrythmia, or death [142]. Kidney failure in tumor lysis syndrome is caused partly by acute UA crystal nephropathy. Here, purines from the nucleus of the lysed tumor cells are metabolized to hypoxanthine and then oxidized to xanthine, which is in turn oxidized to UA. These oxidation steps are catalyzed by the Xanthine oxidase. The UA is filtered freely in the glomeruli and precipitates out in the tubules, causing tubular occlusion and AKI.

The rapid progression of acute UA crystal nephropathy makes it a medical emergency requiring immediate treatment. Besides volume and shock therapy, a few pharmaceutical options are available for the treatment and prophylaxis of tumor lysis syndrome. Urine alkalization may be used to attempt to elevate the intratubular solubility limit of UA. Rasburicase is a recombinant enzyme that, similarly to the uricase in other mammals, catalyzes the oxidation of UA to the better soluble allantoin, hydrogen peroxide, and carbon dioxide [143]. It is the most effective way to rapidly reduce levels of

UA in the blood, making i.v. rasburicase the treatment of choice for manifest tumor lysis syndrome [144]. Xanthine oxidase inhibition, with allopurinol or febuxostat, is another approach to pharmaceutically prevent acute UA crystal nephropathy in patients that are at risk for tumor lysis syndrome. This medication blocks the production of UA from purines, making it a useful tool in the prevention of acute UA crystal nephropathy; however, it has no effect on existing blood UA burden, therefore making it inferior to rasburicase in the treatment of manifest tumor lysis syndrome [145].

1.5.2 Chronic gouty nephropathy

The pathognomonic feature of chronic gouty or chronic UA crystal nephropathy are UA tophi in the medulla of the kidney. A gouty tophus consists of three layers: On the inside there is a needle-shaped UA crystals, these crystals are usually dissolved by the fixation process, leaving a needle shaped cleft. The UA crystal tophus is surrounded by several epithelioid layers of mononuclear cells, also characteristic of tophaceous granulomas are multi-nucleated giant cells, which are formed by the fusion of macrophages. This complex of crystals and surrounding inflammatory infiltrates is embedded in medullary fibrosis, making up the outer layer of the tophus [146].

First observations of a link between gout and kidney disease date back to the 1500s. In the late 1800s, white streaks of deposit were first observed by Sir Alfred Garrod in the pyramids of a gouty patient's kidney and identified as "soda of urate" [147]. Upon further analysis, Garrod described these deposits to lie within fibrotic tissue between the kidney tubuli, making his, the first account of kidney gouty tophi in literature. In 1952, Modern and Meister described a new clinical entity, which they called "the kidney of gout" [148]. The clinical features of this new entity, which they termed "specific renal lesion of gout" were characterized in three patients and consisted of kidney insufficiency, fixed urinary specific gravity, azotemia, normal blood pressure, and the absence of proteinuria or formed elements in the urinary sediment [148]. An autopsy was performed in one of these patients, and the authors described kidney tophi, tubular atrophy, and interstitial fibrosis.

This newly described kidney manifestation of gout was characterized further in 1950 by Talbott and Terplan. In their study, they reviewed 279 autopsy or pathology reports of patients with articular gout [149]. They described most frequently pyelonephritic scars; intrarenal tophi, which were often surrounded by or obscured by stellate sears; arterial sclerosis; and interstitial fibrosis. Talbott and Terplan found that patients with severe tophaceous articular gout had the most abnormal kidney findings. However, they also noted several individual discrepancies between the severity of gout and the extend of kidney damage [149].

In 1968, Barlow and Beilin studied the kidney biopsies of 25 patients with primary gout. In almost every patient they noted extensive nephrosclerosis, which was present in only 46% of age matched controls

[150]. They also stated that the most specific renal lesion in this collective of gouty patients was the presence of crystalline deposits, which they reported to have found in 90% of gouty kidneys in the form of micro calculi in the collecting ducts and needle shaped medullary deposits often surrounded by inflammatory cells [150]. In a series of non-selected 1733 autopsies, a study from 1981 found medullary UA deposits in 8% [151]. The authors found a statistically significant association between the presence of gouty tophi and a clinical history of articular gout and "renal disease of apparently primary, but not gouty, origin" [151]. However, although there was a statistical correlation, 86% of patients with kidney tophi did not have clinical gout. This study and a similar study showing a large discrepancy between medullary UA tophi and clinical gout lead to the conclusion that the presence of UA tophi cannot be used as a diagnostic for gout.

There is a tight association between hyperuricemia and CKD, and it is known that kidney impairment causes elevated blood UA levels by retention of nitrogen compounds [121]. It has, however, not been established whether chronic mild hyperuricemia in turn causes kidney impairment, and if so, by what mechanism. Many authors have postulated that medullary gouty tophi, which build up due to persistent asymptomatic hyperuricemia with or without articular gout, are one mechanism that could explain this observed relationship [54, 148, 152]. Two large reviews, however, have argued the contrary, supporting the claim that medullary gouty tophi are likely a benign byproduct of metabolism and have no pathological value [147, 153]. Here the authors argue that there is not enough evidence to support the claim that medullary gouty tophi actively cause kidney impairment. On the contrary, the authors declare that kidney damage observed in patients with hyperuricemia and gout can be attributed entirely to confounding factors like hypertension, vascular disease, genetic disorders, or lead intoxication. In the recent years, research on medullary gouty tophi has stagnated, and especially evidence in animal models on chronic gouty nephropathy remains scarce. The exact pathophysiology remains unknown. There are authors that postulate that the crystals within the tophi come from the inside of a ruptured tubule [152, 153] and others that propose they primarily of extra-tubular origin [147]. The elucidation of the pathogenesis of medullary tophi would aid greatly in determining their clinical relevance. Presently there are no treatment recommendation for this finding.

1.6 Animal models of hyperuricemia and uric acid crystal nephropathy

Hyperuricemia and its complications, including gout, are difficult to study in murine models. The main reason behind this being the difference in UA physiology and metabolism of mice or rats compared to humans. Uricase function remains conserved in rodents, leading to a much lower serum UA than in humans. The average serum UA concentration C57BL/6 mice is 1.44 mg/dl [154], whereas in humans the average serum UA is 6-8 mg/dl. Loss of uricase function has led humans to evolve effective excretory mechanisms for UA in the kidney that are not needed and therefore missing in rodents.

Although many of the same UA transporters have been described for human and rodent kidneys, they differ in their affinity for UA and their localization within the nephron.

Human URAT1, with a Km of 370 µM, has a higher affinity for UA than its murine ortholog, called mouse renal-specific transporter (RST) with a K_m for UA of 1200 µM [155, 156]. RST knockout mice have only a very mild increase of FEUA (increase from 3% in healthy to 5% in KO-mice) [157] compared to an extreme increase of FEUA, which rises from 10% in healthy humans to 30-90% in humans with SLC22A12 loss of function mutations [63]. Murine Glut9 differs from human GLUT9 in its localization within the kidney. Human GLUT9 is found only in the proximal tubule and on the basolateral membrane; whereas mGlut9 is also found in the distal tubule and the apical membrane [158], further highlighting differences between mouse and human kidney urate handling at a molecular level.

Murine models of hyperuricemia can be created by knockout or inhibition of the hepatic urate oxidase. Hyperuricemia can also be induced in mice by knockout of Glut9 in the liver, leading to loss of access of UA to the hepatic uricase and therefore indirectly inactivating it. Most mouse models of hyperuricemia lead to an acute UA crystal nephropathy with tubular deposition of crystals and kidney injury, similar to patients with tumor lysis or crush syndrome. This demonstrates the importance of Uox in murine UA metabolism and the inability of proper UA handling by the murine kidney, when the Uox function has been impaired. Hyperuricemia in rodents cannot be achieved without in some way impeding or restricting Uox function; even HPRT-deficient mice, which are used as an animal model of Lesch-Nyhan syndrome (an x-chromosomal dominant disorder that leads to cognitive impairment, self-mutilation and hyperuricemia in humans), are not hyperuricemic because the function of the urate oxidase remains intact [159, 160].

1.6.1 Oxonic-acid induced hyperuricemia

The first rodent models of hyperuricemia were created by administration of oxonic acid and UA p.o. into rats [161]. Oxonic acid inhibits the function of the hepatic urate oxidase, leading to hyperuricemia (above 3 mg/dl), which is further augmented by the additional injection of UA. These rats developed moderate hyperuricemia and severe hyperuricosuria. Acute tubular injury was observed after one month followed by mild chronic interstitial nephritis at 36 to 52 weeks [161]. Oxonic acid has since been frequently used as a non-transgenic animal model of hyperuricemia. It is an easy model to use, and can be applied in rodents as well as other animals, like rabbits, and used with or without augmentation of UA or Adenine [162-165]. In 1975, Bluestone *et al.* were able to produce gouty tophi *in vivo* using an oxonic acid-induced hyperuricemia rat model [161]. However, this was an inconsistent finding as only 10% of rats were found to have gouty tophi after 52 weeks of hyperuricemia.

1.6.2 Uricase knockout

The liver enzyme uricase can also be knocked out, leading to hyperuricemia from birth. Compared to the oxonic acid model, in this model, hyperuricemia is much more profound (above 7 mg/dl) as these mice have no functioning uricase [107]. A systemic uricase knockout causes severe urate nephropathy leading to death in more than half of all born mice before the age of 4 weeks from urate nephropathy unless maintained on allopurinol [107, 166]. This, once again, indicates the importance of uricase function in murine UA homeostasis and shows that rodent kidneys are ill equipped to handle a high UA load. Due to the severity of illness caused by this model and its limited availability, it is rarely used to model hyperuricemia.

1.6.3 Glut 9 Knockout

Glut9, apart from being an important UA transporter in the kidney, also plays an important role in the Uox mediated UA metabolism in rodents. Glut9 mediates the transport of UA across hepatocyte cell membranes. Systemic KO of Glut9 in mice leads to a dual phenotype caused by loss of function of both kidney and hepatic Glut9 [167]. Loss of function of hepatic Glut9 leads to hyperuricemia because plasma UA is unable to cross the hepatocyte cell membrane and cannot be metabolized by the intracellular Uox. Loss of function of the renal Glut9 transporter leads to a near total inability of renal urate reabsorption and thus massive uricosuria. These two mechanisms augment each other: Hyperuricemia is caused by the hepatic loss of Glut9 function leading to uricosuria, which is massively increased by the loss of urate reabsorption due to loss of renal Glut9 function. This leads to an extreme UA nephropathy with massive intraluminal UA crystal deposition [167].

The hyperuricemia mouse model used in this work is an inducible, liver specific, Glut9 knockout that was generated by Preitner et. al. [168]. This model is generated using a floxed Glut9 gene and a cre recombinase that is expressed using the albumin promotor, making the expression of this enzyme liver specific as albumin is expressed exclusively in the liver. When the loss of function is desired, the cre can be activated by an *i.p.* injection of Tamoxifen leading to a knockdown of Glut9. The inducible nature of this phenotype means that hyperuricemia can be induced when a special diet is applied. Therefore, there is no perinatal mortality due to early onset kidney disease in these mice as seen in systemic Glut9 or Uox KO mice. The phenotype of kidney disease and uricosuria is less severe than in systemic Glut9 KO mice because the renal Glut9 mediated UA reabsorption is maintained in these mice thus making this model more physiological and better to study the effects of hyperuricemia. Hyperuricemia and kidney disease can be augmented in this model by feeding the mice inosine and a high fat diet. Inosine, a urate precursor, is metabolized to UA leading to a higher UA burden and plasma UA concentrations of around 8 mg/dl [168]. The high fat diet is used to augment kidney disease by decreasing urine pH and therefore increasing the likelihood of tubular UA crystalluria [168].

2 Objectives and Experimental Strategy

2.1 Objectives

Chronic UA crystal nephropathy, defined as the presence of UA tophi in the kidney parenchyma, is a disease entity that has been controversy discussed in the past. It was previously assumed that kidney UA tophi cause kidney disease and are among the main reasons behind the widely observed association between hyperuricemia and CKD. However, after a series of publications casting doubt on the pathological relevance of medullary tophi [147, 153], the interest in this subject has tailed off and very little further research has been done in this field. Nevertheless, the entity of tophaceous UA nephropathy remains present throughout the literature and is often cited as a cause of CKD [169], as well as the relationship between asymptomatic hyperuricemia and CKD progression. Therefore, it remains to be elucidated whether asymptomatic hyperuricemia or UA crystal granulomas contribute to CKD progression. Previous reports focused only on statistical analysis to correlate markers of kidney injury to the presence of UA crystal granulomas. Currently, no animal model exists to investigate whether these asymptomatic hyperuricemia or hyperuricemia-related UA crystal granuloma causally contribute to the progression of CKD.

The following objectives were set for this study:

1. To characterize the histological abnormalities of diagnostic kidney biopsies with medullary UA crystal granulomas in a retrospective case-control study.
2. To investigate whether hyperuricemia with UA crystal granuloma formation causes or contributes to CKD progression in a novel mouse model of chronic UA crystal nephropathy.
3. To test whether asymptomatic hyperuricemia exacerbates preexisting CKD in mice.

2.2 Experimental Strategy

Through a collaborator, a large series of kidney biopsy reports with described UA tophi and a series of control biopsies were acquired. These were statistically evaluated to look for a correlation between the presence of UA tophi and the extent of described interstitial kidney fibrosis and glomerular sclerosis, a very precise way to measure the extend of chronic kidney damage.

To further study the pathogenesis of medullary gouty tophi *in vivo*, a reliable mouse model for this is first needed. Amongst the available and above described mouse models of hyperuricemia and UA crystal nephropathy, none have been able to reliably model tophaceous UA nephropathy. The UA nephropathy seen in all described models is attributed to the acute intraluminal precipitation of UA and is therefore similar to acute UA nephropathy seen in humans with tumor lysis or crush syndrome.

The idea behind creating an *in vivo* model for tophaceous UA nephropathy was to obtain a mouse model with mild to moderate hyperuricemia and mild UA nephropathy. The model would be run over an extended period with monitoring the GFR until UA crystalluria-induced tubular obstruction progresses to CKD and enough time has passed for interstitial fibrotic transformation of the kidney to commence. These mice would be sacrificed at this point and the kidneys would be histologically examined for tophus formation.

The choice fell upon the Alb-creERT2;*Glut9*$^{lox/lox}$ mouse [168]. Due to it being an inducible mouse model, there is no elevated perinatal mortality. After knockdown of *Glut9* with tamoxifen, these mice remain healthy. Alb-creERT2;*Glut9*$^{lox/lox}$ mice fed a standard chow diet enriched with the UA precursor inosine develop asymptomatic hyperuricemia but without kidney disease. On the other hand, feeding Alb-creERT2;*Glut9*$^{lox/lox}$ mice an acidogenic diet supplemented with inosine results in hyperuricemia and UA crystalluria-associated CKD. The inducibility of both hyperuricemia (by feeding a chow diet with inosine) and tophaceous UA nephropathy with interstitial nephritis (by feeding an acidogenic diet with inosine) make this mouse model the correct choice for the attempt to create *in vivo* kidney UA tophi. The goal was to elucidate the pathogenesis of medullary gouty tophi: is kidney fibrosis a prerequisite for the formation of tophi or do tophi form in a hyperuricemic environment while kidney damage is just beginning?

In order to further test this question, another animal model using aristolochic acid I was set up to induce non-crystalline CKD in mice, which were then made hyperuricemic to test if pre-existing fibrosis causes kidney tophi formation in a hyperuricemic environment. This experiment was also used to test whether hyperuricemia exacerbates preexisting CKD in mice.

3 Materials and Methods

3.1 Materials

3.1.1 Animal experiments

Animals

Alb-creERT2;*Glut9*$^{lox/lox}$ Mouse	Mouse Metabolic Facility, Lausanne, Switzerland

Animal maintenance

H-Temp Polysulfon Cage Eurostandard Typ II	Techniplast, Hamburg, DE
Chow diet	Ssniff Spezialdiäten GmbH, Soest, DE
High fat diet	Ssniff Spezialdiäten GmbH, Soest, DE
High fat diet with inosine supplementation	Research Diets Inc., New Brunswick, USA
Interior lattice cover	Techniplast, Hamburg, DE
Autoclavable filter hood	Techniplast, Hamburg, DE
Polycarbonate drinking bottles	Techniplast, Hamburg, DE
Mouse house red	Techniplast, Hamburg, DE
Litter of aspen wood	Ssniff Spezialdiäten GmbH, Soest, DE

Composition of standard Chow diet

Ingredient	**Quantity**
Gross Energy	16.7 MJ/kg
Metabolizable Energy	13.6 MJ/kg
Dry matter	87.9 %
Crude protein	22.0 %
Crude fat	4.5 %
Crude fiber	3.9 %
Crude ash	6.8 %
N free extracts	50.8 %
Starch	34.0 %
Sugar	5.0 %
Calcium	1.00 %
Phosphorus	0.70 %
Sodium	0.24 %

Magnesium	0.21 %
Potassium	1.02 %
Vitamin A	25,000 IU/kg
Vitamin D_3	1,000 IU/kg
Vitamin E	135 mg/kg
Vitamin K (as menadione)	20 mg/kg
Thiamin (B_1)	86 mg/kg
Riboflavin (B_2)	32 mg/kg
Pyridoxine (B_6)	31 mg/kg
Cobalamin (B_{12})	150 µg/kg
Nicotinic acid	145 mg/kg
Pantothenic acid	60 mg/kg
Folic acid	10 mg/kg
Biotin	700 µg/kg
Choline-Chloride	3,130 mg/kg
Inositol	100 mg/kg
Inosine (only if chow diet included inosine supplementation)	25.6 g/kg

Composition of acidogenic diet

Ingredient	**g%**	**kcal%**
Protein	23	17
Carbohydrate	35	26
Fat	36	58
Total		100
kcal/g	5.6	

Ingredient	**g**	**kcal**
Casein, 80 Mesh	228	912
DL-M ethionine	2	8
Maltodextrin 10	170	680
Sucrose	175	700
Soybean Oil	25	225
Coconut Oil, Hydrogenated	333.5	3002
Mineral Mix S10001	40	0

Sodium Bicarbonate	10.5	0
Potassium Citrate, 1 H2O	4	0
Vitamin Mix V10001	10	40
Choline Bitartrate	2	0
FD&C Red Dye #40	0.1	0
Total	1000.1	5567

Composition of acidogenic diet plus inosine

Ingredient	**g%**	**kcal%**
Protein	22	*17*
Carbohydrate	35	*26*
Fat	35	*58*
Total		*100*
kcal/g	5.4	

Ingredient	**g**	***kcal***
Casein, 80 Mesh	228	*912*
DL-Methionine	2	*8*
Maltodextrin 10	170	*680*
Sucrose	175	*700*
Soybean Oil	25	*225*
Coconut Oil, Hydrogenated	33.5	*3002*
Mineral Mix S10001	40	*0*
Sodium Bicarbonate	10.5	*0*
Potassium Citrate, 1 H2O	4	*0*
Vitamin Mix V10001	10	*40*
Choline Bitartrate	2	*0*
Inosin	26.3	*0*
FD&C Blue Dye #1	0.05	*0*
Total	**1026.4**	***5567***
Inosin (g/kg)	25.6	

Blood extraction

Glass capillaries 32 x 0,8 mm, not heparinized	NeoLab Migge GmbH, Heidelberg, DE
Isofluran Forene®	Abbott, Wiesbaden, DE
Eppendorf-Tubes 1,5 ml	TPP, Trasadingen, CH
Eppendorf-Tubes 2,0 ml	TPP, Trasadingen, CH

Genotyping

DirectPCR® Lysis Reagent Tail	PEQLAB Biotechnologie GmbH, Erlangen, DE
Proteinase K	Qiagen GmbH, Hinden, DE
Quali-PCR-Tubes	Kisker Biotech GmbH, Steinfurt, DE
Taq DNA Polymerase	New England BioLabs, Frankfurt, DE
10X Standard Taq Reaction Buffer	New England BioLabs, Frankfurt, DE
Genotyping Primers	metabion, Martinsried, DE
dNTP Set	Thermo Fisher Scientific Inc., Waltham, USA
Agarose	Invitrogen Ltd., Waltham, USA
peqGREEN DNA/ RNA dye	PEQLAB Biotechnologie GmbH, Erlangen, DE
Low MW DNA Ladder	New England BioLabs, Frankfurt, DE
6X DNA Loading	Thermo Fisher Scientific Inc., Waltham, USA
Tris-HCl	Roth, Karlsruhe, DE
Boric acid	Sigma-Aldrich, Taufkirchen, DE
Ethylene diamine tetraacetate (EDTA) sodium salt	Merck, Darmstadt, DE

Organ extraction

RNAlater	Life Technologies, Darmstadt, DE
Formalin, 4 %	Morphisto GmbH, Frankfurt, DE
Embedding cassettes	NeoLab, Heidelberg, DE
Disposable scalpel No. 11	Feather Safety Razor Co. Ltd., JPN

Intraperitoneal injection and oral gavage

BD Microlance™ 3, 30G	Becton, Dickinson, Franklin Lakes, USA
BD Plastipak™ syringe	Becton, Dickinson, Franklin Lakes, USA
Natural oil (Mygliol®812)	Sigma-Aldrich, Taufkirchen, DE
Tamoxifen	Sigma-Aldrich, Taufkirchen, DE
Ethanol	Merck, Darmstadt, DE

Aristolochic acid I	Merck, Darmstadt, DE
Phosphate buffered saline (PBS)	PAN-Biotech GmbH, Aidenbach, DE
Inosine	Sigma-Aldrich, Taufkirchen, DE
Polyethylene glycol (PEG)	Merck, Darmstadt, DE
Gavage needle	Fisher Scientific UK Ltd, Loughborough, UK

Measurement of glomerular filtration rate

FITC-Sinistrin	Fresenius Kabi, Bad Homburg, DE
Leukoplast® hospital	BSN medical GmbH, Hamburg, DE
NIC-Kidney Patches 3x3cm	MediBeacon GmbH, Mannheim, DE
Rechargable batteries for NIC-Kidney devices	MediBeacon GmbH, Mannheim, DE
Transdermal GFR Monitor	MediBeacon GmbH, Mannheim, DE
Sterile gauze swab	Nobamed Paul Danz, Wetter, DE
Isoflurane CP®	CP-Pharma Handelsgesellschaft mbH, Burgdorf, DE

3.1.2 Histology and microscopy

Slides	Thermo Fisher Scientific Inc., Waltham, USA
Cover glasses for microscopy	Thermo Fisher Scientific Inc., Waltham, USA
Sodium acetate trihydrate	Merck, Darmstadt, DE
3,3'-Diaminobenzidine	Merck, Darmstadt, DE
Antigen Unmasking Solution	Vector Laboratories, Burlingame, USA
Avidin/Biotin Blocking Kit	Vector Laboratories, Burlingame, USA
Biotinylated Lotus Tetragonolobus Lectin	Vector Laboratories, Burlingame, USA
Acetic acid 99-100%	Merck, Darmstadt, DE
Coloring solutions containing hematoxylin	Sigma-Aldrich, Taufkirchen, DE
MACH 1 Universal HRP-Polymer Detection	Biocare Medical, Concord, USA
Skimmed milk powder	Merck, Darmstadt, DE
Methanol	Merck, Darmstadt, DE
Methyl green	Sigma-Aldrich, Taufkirchen, DE
Ethanol	Merck, Darmstadt, DE
Ammonium peroxodisulfate	Carl Roth GmbH + Co. KG, Karlsruhe, DE
Acetone	Merck, Darmstadt, DE
Direct Red 80	Sigma-Aldrich, Taufkirchen, DE
Paraplast® for tissue embedding	Merck, Darmstadt, DE

Xylol	Fisher Scientific UK Ltd, Loughborough, UK
Nuclear Fast Red solution	Sigma-Aldrich, Taufkirchen, DE
Periodic acid	Carl Roth GmbH + Co. KG, Karlsruhe, DE
Proteinase K	Qiagen GmbH, Hinden, DE
Hydrochloric acid	Carl Roth GmbH + Co. KG, Karlsruhe, DE
Schiff's reagent	Sigma-Aldrich, Taufkirchen, DE
Silver nitrate	Carl Roth GmbH + Co. KG, Karlsruhe, DE
VectaMount Permanent Mounting Medium	Vector Laboratories, Burlingame, USA
VECTASTAIN® Elite®ABC-HRP Kit	Vector Laboratories, Burlingame, USA
Hydrogen peroxide	Carl Roth GmbH + Co. KG, Karlsruhe, DE
Rasburicase	EBiosciences, San Diego, USA

3.1.3 Analytical methods

RNA isolation

2-Mercaptoethanol	Sigma-Aldrich, Taufkirchen, DE
Lysing Matrix D, 2 mL Tube	MP Biomedicals, Eshwege, DE
PureLink™ RNA Mini Kit	Life Technologies, Carlsbad, USA
Ethanol 96%	Merck, Darmstadt, DE
Falcon® 5ml Polypropylene Round-Bottom Tube	Corning Science, Kaiserslautern, DE
RNase AWAY®	Sigma-Aldrich, Taufkirchen, DE
RNase-Free DNase Set	Qiagen GmbH, Hinden, DE
Distilled water (DNAse/RNase free)	GIBCO/Invitrogen, Paisley, Scotland, UK

Reverse transcription

Strand Buffer	Thermo Fisher Scientific Inc., Waltham, USA
0.1 M DTT	Thermo Fisher Scientific Inc., Waltham, USA
RNasin® Ribonuclease Inhibitor	Promega GmbH, Walldorf, DE
dNTP Set	Thermo Fisher Scientific Inc., Waltham, USA
Hexanucleotide Mix	Roche Diagnostics, Basel, CH
Linear Acrylamide	Thermo Fisher Scientific Inc., Waltham, USA
SuperScript™ III Reverse Transcriptase	Thermo Fisher Scientific Inc., Waltham, USA

qPCR

10X Taq Buffer	Thermo Fisher Scientific Inc., Waltham, USA
Optically clear adhesive film	Sarstedt AG & Co. KG, Nümbrecht, DE

BioStab PCR Optimizer	Biomol GmbH, Hamburg, DE
96 Well Lightcycler Plate	Sarstedt AG & Co. KG, Nümbrecht, DE
SYBR® Green I nucleic acid gel stain	Sigma-Aldrich, Taufkirchen, DE
Bovine Serum Albumin, PCR grade	Thermo Fisher Scientific Inc., Waltham, USA
Taq DNA Polymerase	New England BioLabs, Frankfurt, DE
$MgCl_2$ 25mM	Thermo Fisher Scientific Inc., Waltham, USA
dNTP Set	Thermo Fisher Scientific Inc., Waltham, USA
PCR primers	Metabion, Martinsried, DE

Primer List

18s RNA	Forward	5‘-GCAATTATTCCCCATGAACG-3‘
	Reverse	5‘-AGGGCCTCACTAAACCATCC-3‘
KIM-1	Forward	5‘-TCAGCTCGGGAATGCACAA-3‘
	Reverse	5‘-TGGTTGCCTTCCGTGTCTCT-3‘
Il6	Forward	5’-TGATGCACTTGCAGAAAACA-3’
	Reverse	5’-ACCAGAGGAAATTTTCAATAGGC-3’
Tnfα	Forward	5‘-CCACCACGCTCTTCTGTCTAC-3‘
	Reverse	5‘-AGGGTCTGGGCCATAGAACT-3‘
Collagen1α1	Forward	5‘-ACATGTTCAGCTTTGTGGACC-3‘
	Reverse	5‘-TAGGCCATTGTGTATGCAGC-3‘
Fibronectin-1	Forward	5‘-GGAGTGGCACTGTCAACCTC-3‘
	Reverse	5‘-ACTGGATGGGGTGGGAAT-3‘
FSP-1	Forward	5‘-CAGCACTTCCTCTCTCTTGG-3‘
	Reverse	5‘-TTTGTGGAAGGTGGACACAA-3‘

Photometric Methods

QuantiChrom™ Uric Acid Assay Kit	BioAssay System, Hayward, USA
Urea FS	DiaSys GmBH, Holzheim, DE
Creatinine FS	DiaSys GmBH, Holzheim, DE
96F microwell plate without lid	Thermo Fisher Scientific Inc., Waltham, USA

Flow cytometry

Zombie NIR™ Fixable Viability Kit	BioLegend, Fell, DE
FBS	Biochrom GmbH, Berlin, DE
Nykodenz	Axis-Shield Diagnostics Ltd., Dundee, GBR

PBS	PAN-Biotech GmbH, Aidenbach, DE
Collagenase (Clostridium histolyticum)	Sigma-Aldrich, Taufkirchen, DE
DNase I	Sigma-Aldrich, Taufkirchen, DE
Pre-Seperation Filter (70 mm)	Miltenyi Biotec GmbH, Bergisch Gladbach, DE
BSA Fraction V	Roche Diagnostics, Basel, CH
Sodudium azide	Carl Roth GmbH + Co. KG, Karlsruhe, DE
AccuCheck Counting Beads	Thermo Fisher Scientific Inc., Waltham, USA
AbC™ Anti-Rat/Hamster Bead Kit	Thermo Fisher Scientific Inc., Waltham, USA

Antibodies for flow cytometry

PE/Cy5 linked anti-mouse CD45	BioLegend, Fell, DE
V450 linked anti-mouse CD11b	BioLegend, Fell, DE
FITC linked anti-mouse CD206	BD Biosciences, DE
PE/Cy7 linked anti-mouse CD11c	BioLegend, Fell, DE
PE/Cy7 linked anti-mouse Gr-1	BioLegend, Fell, DE
BV510 linked anti-mouse MHCII	BioLegend, Fell, DE
PE linked anti-mouse CX3CR1	BioLegend, Fell, DE
PE/Cy7 linked anti-mouse Ly6C	BioLegend, Fell, DE
FITC linked anti-mouse Ly6G	BioLegend, Fell, DE
APC linked anti-mouse CD4	BioLegend, Fell, DE
PE linked anti-mouse CD8	BioLegend, Fell, DE
APC linked anti-mouse F4/80	Bio-Rad Laboratories, Inc., Hercules, USA
Zombie NIR viability dye	BioLegend, Fell, DE

3.1.4 Instruments and devices

Non-disposables

Flow cytometer BD FACS Canto II	BD Biosciences, Heidelberg, DE
Electrophoresis chamber Mini-PROTEANR Tetra System	Bio-Rad Laboratories, Inc., Hercules, USA
PowerPac 300 electrophoresis power supply	Bio-Rad Laboratories, Inc., Hercules, USA
Microwave	Severin, Sundern, DE
GENios Plus Elisa reader	Tecan, Männedorf, CH
Real-Time PCR-System LightCycler 480	Roche Diagnostics, Basel, CH
Homogenizer ULTRA-TURRAXR T 25 basic	IKA® -Werke GmbH & Co. KG, Fulda, DE
Thermomixer 5436	Eppendorf AG, Hamburg, DE

Modular paraffin pouring station EC 350	Microm International GmbH, Dreieich, DE
Spektrophotometer NanoDrop 1000	Thermo Fisher Scientific Inc., Waltham, USA
Water bath 1013	GFL mbH, Burgwedel, DE
Tube Roller SRT6	Stuart Equipment, Staffordshire, UK
Centrifuge Megafuge 1.0R	Heraeus Instruments, Hanau, DE
Centrifuge 5415 C	Eppendorf AG, Hamburg, DE
Rocky-N rocker table	Labortechnik Froebel GmbH, Lindau, DE
Vortex-Genie™ 2 G-560-E	Scientific Industries, Inc., Bohemia, USA
Kryostat CM3000	Leica Biosystems, Wetzlar, DE
Leica DMRBE Research Microscope	Leica Microsystems, Wetzlar, DE
Rotational microtome HM 340 E	Microm International GmbH, Dreieich, DE
Sterile workbench Microflow Biological Safety Cabinet	Nunc GmbH, Langenselbold, DE
Thermo-Cycler Mastercycler® pro	Eppendorf AG, Hamburg, DE
X-ray film developer Curix 60	AGFA, Mortsel, BEL
SurgiVet vaporizer for florane Anesthetic	Smiths Medical, Grasbrunn, DE
Semi-Dry-Blotter Trans-Blot® SD	Bio-Rad Laboratories, Inc., Hercules, USA
Vertical rotator	Bachofer GmbH & Co. KG, Weilheim, DE
pH meter WTW	WTW GmbH, Weilheim, DE
Multipipette Plus	Eppendorf AG, Hamburg, DE
Research Pipette Plus 30 – 300 µl	Eppendorf AG, Hamburg, DE
Pipetman 2, 10, 20, 100, 200, 1000 µl	Gilson, Middleton, US
Pipetus classic	Hirschmann Laborgeräte, Eberstadt, DE

Disposables

Eppendorf tubes 1.5, 2.0 ml	Eppendorf AG, Hamburg, DE
Serological pipettes	BD Biosciences, Heidelberg, DE
Pipette tips 10 – 1000 µl	Peske, Aindling-Arnhofen, DE
Vacuum filtration system 150 ml, 500 ml	TPP, Trasadingen, CH
Falcon tubes 15, 50 ml	BD Biosciences, Heidelberg, DE
Needles 16, 18, 20, 22, 24, 26 G	BD Biosciences, Heidelberg, DE
Tissue culture dishes	TPP,Trasandigen, CH
Ultra-cut	Leica Microsysteme, Wetzlar, DE
Diskardit II syringe 1 ml, 2 ml, 5 ml	BD Biosciences, Heidelberg, DE
Tweezers	Angiokard Medizintechnick, Freiburg, DE

SuperFrost Plus ™ adhesive slides	Fisher Scientific GmbH, Schwerte, DE
Pipette tips ep T.I.P.S	Eppendorf AG, Hamburg, DE
ELISA 96-well plate	Thermo Fisher Scientific Inc., Waltham, USA
X-ray films	Sigma-Aldrich, Taufkirchen, DE
Embedding cassettes	ISOLAB, Wertheim, DE

3.1.5 Software

ImageJ	Wayne Rasband, USA
Prism	Graph Pad, San Diego, USA
Microsoft Excel	Microsoft Corp., Redmond, USA
Microsoft PowerPoint	Microsoft Corp., Redmond, USA
Microsoft Word	Microsoft Corp., Redmond, USA
SPSS 24	IBM, Armonk, USA

3.2 Analysis of human biopsy reports

3.2.1 Database search and acquisition of diagnostic biopsy reports

The kidney biopsies at the Arkana Laboratories, Little Rock, were examined by experienced kidney pathologists using standardized methods. The tissue cylinder was fixed in Michel's fixative or in 10% neutral buffered formalin. Sections were then stained with period acid-Schiff (PAS), hematoxylin and eosin (H&E) or silver stain according to standard protocol. Representative images were taken. The Arkana Laboratories archive up to June 2016 was searched with the key words: HU, gouty arthritis, UA tophi, UA urolithiasis and UA nephropathy and the presence of UA tophi on kidney biopsies. This search yielded 199 pathology reports from patients with UA-related pathologies (patients with medullary UA tophi that were found in the biopsy of patients with previously diagnosed hyperuricemia or hyperuricemia-related conditions). The biopsy reports were anonymized before being subjected to qualitative and quantitative case-control analysis. This study was approved by the local Ethics Board of the Medical Faculty at the Ludwig-Maximilians University Munich, Germany (17-588 UE).

The aim of my study was to examine the influence of kidney tophi on histological-morphological features, such as interstitial fibrosis. Therefore, two groups were needed for the comparison. The experimental group consisted of 84 cases in which the examining pathologists found UA tophi. To allow for a retrospective case-control-study with equal group sizes, 84 cases were selected at random of the 115 case reports with hyperuricemia (see section 4.1.1, Figure 11). A retrospective analysis was performed using these standardized kidney biopsy reports (84 cases with UA tophi versus 84 cases with hyperuricemia or hyperuricemia-related pathologies but without UA tophi).

For statistical comparison of the diagnostic kidney biopsies with and without UA tophi, the biopsy reports were anonymized and then subjected to statistical analysis. Interstitial fibrosis and tubular atrophy, arterial and arteriolar nephrosclerosis were evaluated and scored by the pathologists as absent (<5% of area involved), mild (6-25% of area involved), moderate (26-50% of area involved), or severe (>50% of area involved) [170]. To assess the ratio of glomerulosclerosis between the two groups, the number of globally sclerosed glomeruli was divided by the total number of glomeruli present. UA crystal deposits appeared as empty spaces in form of needle shaped or feathery clefts representing dissolved UA crystals after formalin fixation and tissue processing.

3.2.2 Statistical evaluation and comparison of the groups

An Excel table was generated in which all variables were recorded for all cases. Examples include sex, age, grading of interstitial fibrosis, serum creatinine (if reported), etc. From this an SPSS document was produced in which the variables were numerically coded for all cases and were thus ready for statistical analysis. The Mann-Whitney-U test was used to compare metric data. The χ^2 test for trend was used to compare ordinally scaled data. The χ^2-test was used to compare nominally scaled data. If nominal data was present on a 2x2 spread, Fisher's exact test was used. An $\alpha = 0.05$ was assumed. The term "significant difference" in the text of this work is equivalent to its statistical meaning. In the graphics, the p-value is abbreviated as follows: $p < 0.05$ with "*", $p < 0.01$ with "**", and $p < 0.001$ with "***".

3.3 Animal experiments

3.3.1 Animal housing and care

The experimental animals used in the present work were exclusively mice, obtained from a collaborator, the Mouse Metabolic Facility in Lausanne, Switzerland, and then bread to acquire the desired genetic background in our laboratory. The genetic modification used in this model were created and described by Preitner et. al [168] in a C57BL/6N genetic background. The mice were judged healthy based on FELASA recommendations [171].

The provisions of the German Animal Welfare Act (Tierschutzgesetz) were always applied during the experiments. All animal experiments used were explicitly approved by the government (Regierung von Oberbayern) prior to the study (AZ: ROB-55.2-2532.Vet_02-15-189) or II LKE in Krakow (reference number: 70/2018, 257/2018) based on the EU directive for the Protection of Animals Used for Scientific Purposes (2010/63/EU) and reported according to the ARRIVE guidelines [172].

The mice were kept in groups of up to 5 animals inside polypropylene and cellulose cages containing a red plastic mouse house and aspen wood litter. The mouse facility was kept at 22±2°C and a 12-hour light / dark cycle. Water and standard chow (ssniff-Spezialdiäten GmbH) was available to the animals

ad libitum. The cages of the mice were changed once a week by a trained laboratory animal keeper. Cages, lids, bedding, houses, iron inlays, food, and water (ddH2O) were sterilized by autoclaving at 120°C and 1 bar pressure for 20 minutes. The transfer of the animals into fresh cages procedures on the animals were carried out under sterile conditions.

3.3.2 Mouse model of chronic uric acid nephropathy

The Alb-creERT2;*Glut9*$^{lox/lox}$ mice were created and kindly provided by Frederic Preitner and Bernhard Thorens from the Center of Integrative Genomics in Lausanne, Switzerland [167, 168]. These mice contain a genomically integrated albumin promotor (Alb) that set is before the exon sequences of a cre recombinase coupled with an estrogen receptor (ERT2). Albumin is the most abundant serum protein and its function is the creation and maintenance of intravascular oncotic pressure and the blood transport of low molecular substances. Albumin is expressed exclusively in the liver, leading to a liver-specific expression of cre and ERT2 in these mice. Cre is an enzyme that recognizes and cuts loxP sites in the genome. In this mouse model, cre is attached to the estrogen receptor ERT2, keeping the recombinase outside of the nucleus. When knockout induction is desired, tamoxifen is given. Tamoxifen binds to ERT2, leading to conformational changes within the protein, allowing the compound protein to enter the nucleus, where the cre recombinase can cut the loxP sites in the DNA.

In this mouse model, the *Glut9* is flanked by two loxP sites that act as a DNA recognition pattern for the cre recombinase. Glut9 is a transmembrane channel for UA that is used in the liver by mice to internalize UA for enzymatic degradation. Glut 9 is not a liver specific protein; in the mouse kidneys it is used to reabsorb UA. Due to the presence of the albumin promoter before the cre-ERT2 protein complex, the knockout is liver specific and does not have systemic consequences. Figure 5 provides a graphic overview.

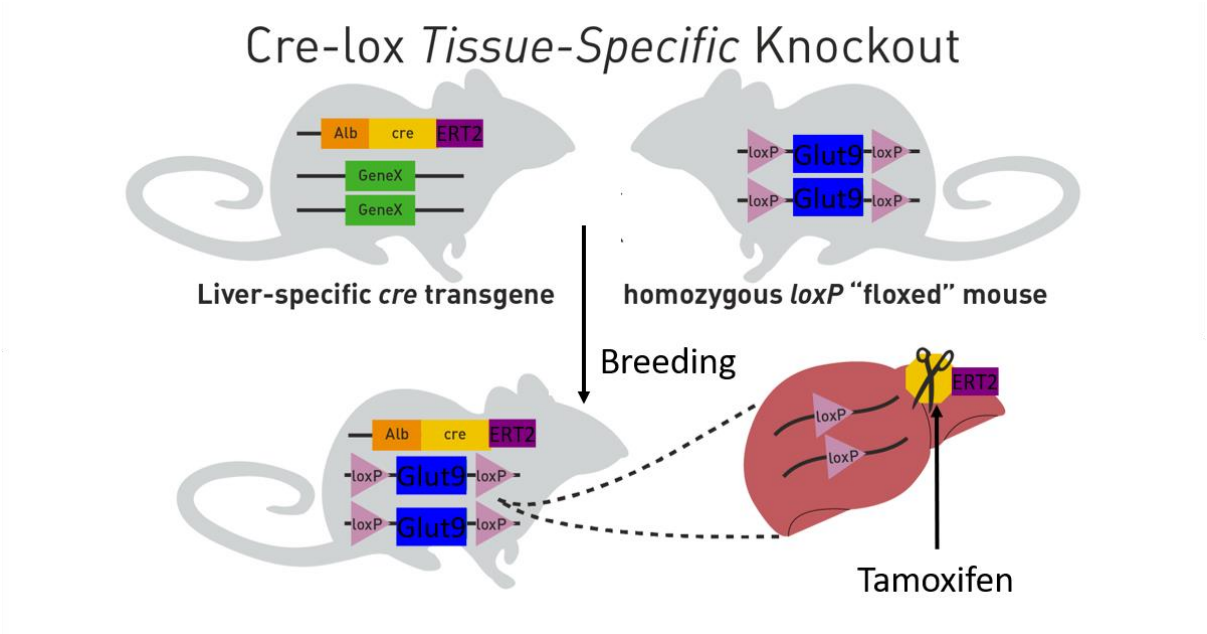

Figure 5. The Alb-creERT2;*Glut9*$^{lox/lox}$ mouse explained
The Alb-creERT2;*Glut9*$^{lox/lox}$ mouse is created by crossing an Alb-creERT2 mouse with a *Glut9*$^{lox/lox}$ mouse and breeding until the desired genotype (homozygous Alb-creERT2(ki/ki);*Glut9*$^{lox/lox}$) is created. The liver specific Glut9 knockout remains dormant until tamoxifen is injected into the mouse. Once tamoxifen is administered, the cre recombinase is able to cross the nuclear membrane and cut the DNA double strand at the loxP sites, leading to a loss of the *Glut9* gene and the activation of the knockout. Modified after https://www.jax.org/news-and-insights/jax-blog/2011/september/cre-lox-breeding [173].

The Alb-creERT2;*Glut9*$^{lox/lox}$ mice were intraperitoneally (i.p.) injected with tamoxifen at around 5 weeks of age. Tamoxifen was administered a total of three times every alternate day, with a daily dose of 1 mg. The tamoxifen crystals (Sigma-Aldrich) were weighed out to 15 mg on a microscale inside a 15 ml Falcon tube. The 15 mg of tamoxifen was then dissolved in 150 µl of 99.9% Ethanol and 1,350 µl of natural oil (Mygliol®812). This made a solution with a total volume of 1,500 µl and 1 mg of tamoxifen per 100 µl. Each mouse received 100 µl of this solution per injection.

To investigate whether UA crystal deposits can trigger acute uric acid crystal nephropathy, Alb-creERT2;*Glut9*$^{lox/lox}$ and *Glut9*$^{lox/lox}$ control mice were injected with tamoxifen to knock out *Glut9* in hepatocytes and placed on an acidogenic diet (ACD) for 6 weeks. On day 42, 43, and 44, both groups of mice received an oral administration of the precursor inosine [168].

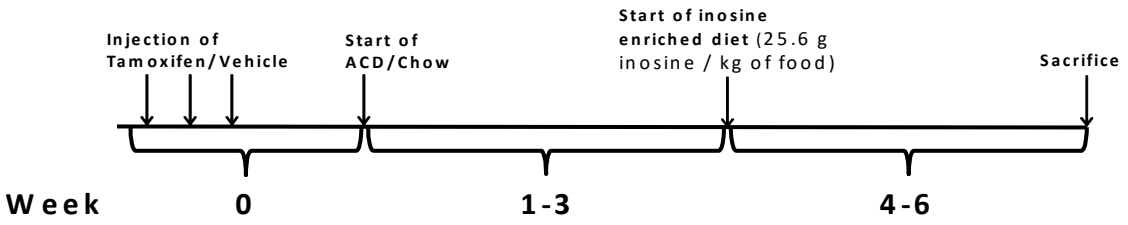

Figure 6. Experimental Timeline
On Monday, Wednesday, and Friday of week 0, the mice received an i.p. injection of either 15mg tamoxifen or the natural oil/ethanol vehicle. On Monday of week 1, the diet was changed to a acidogenic diet in the ACD groups. On Monday of week 4, daily gavage of 40mg of inosine was started. On Sunday of week 6, the mice were sacrificed and the experiment was ended.

3.3.3 Aristolochic acid mouse model

Aristolochic acid (AA) was used to induce CKD in Alb-creERT2;*Glut9*$^{lox/lox}$ and *Glut9*$^{lox/lox}$ control mice before making them hyperuricemic. The experiments using AA in mice were kindly performed by Maciej Lech in Krakow, Poland (reference number of approved animal clearance: 70/2018, 257/2018). As described in section 1.1.1, AA causes rapid progressive tubular necrosis and fibrosing interstitial nephritis. In a very short period, the mice develop relevant amounts of kidney fibrosis. AA was administered a total of six times every alternate day as described in Honarpisheh et. al [35]. Aristolochic acid I (AAI) was dissolved in 500 µl D-PBS and injected at 5 mg/kg bodyweight. The control group received injections of the D-PBS vehicle without the dissolved AAI salt. AA was administered via intraperitoneal injection every other day for a total of 6 injections.

Experimental setup and timeline

The relationship between hyperuricemia and CKD were investigated in three experimental groups. The phenotypes were distributed amongst the three groups as followed: CKD and asymptomatic hyperuricemia (HU) were induced in Group A, only CKD was induced in group B, and only asymptomatic hyperuricemia was induced in group C. HU was created using Alb-creERT2;*Glut9*$^{lox/lox}$ genetic background described in the previous section and induced a total of three 1 mg i.p. injections of tamoxifen every other day. CKD was induced by i.p. injections of 5 mg/kg of aristolochic acid I salt in D-PBS a total of six times every alternate day. Mice in group B carried only a floxed *Glut9* gene but no cre recombinase (+/+ *Glut9*$^{lox/lox}$), therefore the knockout was not induced upon tamoxifen injection and the mice remained normouricemic. Mice in group C received only the D-PBS vehicle per i.p. injection without AAI. Figure 7 gives an overview of the experimental setup and the phenotypes of the three groups. Baseline blood was collected before the phenotype induction with AAI and tamoxifen

and on day 42 shortly before mouse sacrifice. The measurement of GFR was performed at baseline (before phenotype induction), on day 21 and 42.

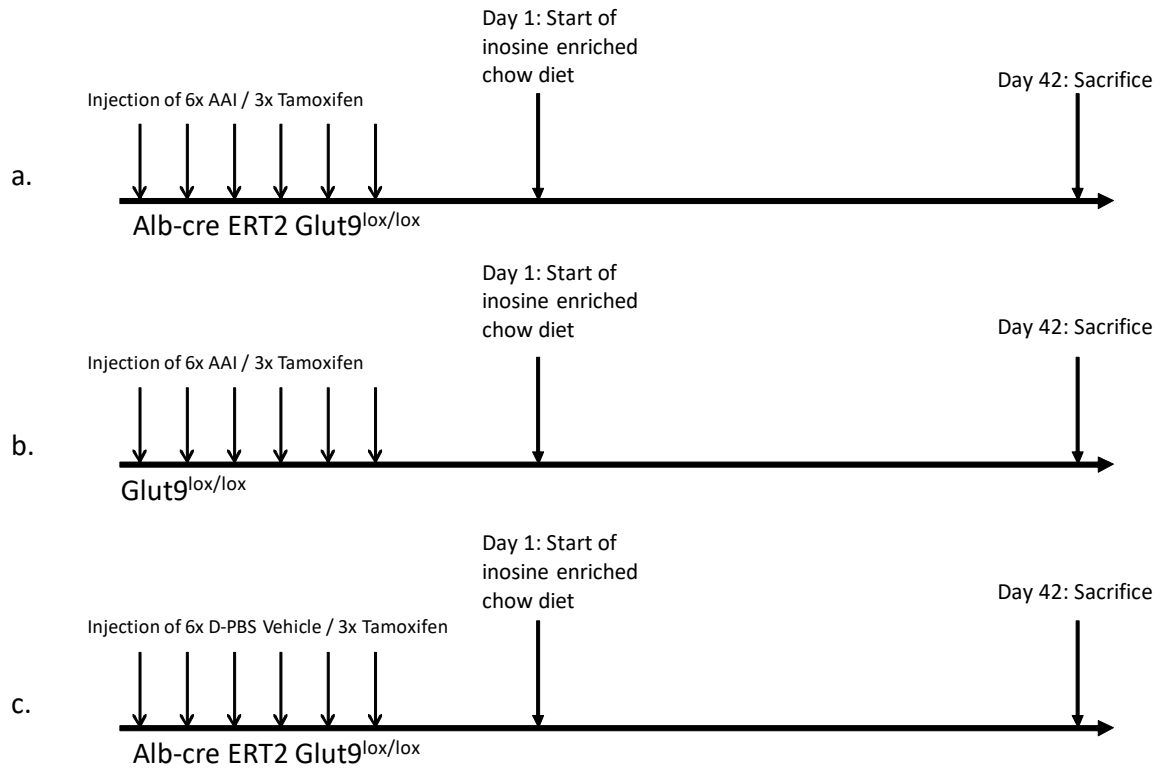

Figure 7. Experimental setup and timeline
(a) Group A (HU + CKD): The Alb-creERT2;*Glut9*$^{lox/lox}$ mice received a total of six i.p. injections of AAI (5 mg/kg) to induce CKD and a total of 3 i.p. injections of tamoxifen to induce hyperuricemia (HU). (b) Group B (CKD only): The mice carried +/+ *Glut9*$^{lox/lox}$ background and received total of six i.p. injections of AAI (5 mg/kg) to induce CKD and a total of 3 i.p. injections of tamoxifen without inducing the Glut9 knockout due to a missing Alb-creERT2 recombinase. (c) Group C (HU only): The Alb-creERT2;*Glut9*$^{lox/lox}$ received three injections of 100mg tamoxifen to induce hyperuricemia and 6 i.p. injection of the D-PBS vehicle without AAI. Inosine enriched chow diet was started on day 1 of the experiment. The mice were sacrificed on day 42.

3.3.4 Breeding and genotyping

Mice were kept as Alb-creERT2;*Glut9*$^{lox/lox}$ (ki/ki)and *Glut9*$^{lox/lox}$ (+/+) mice. In preparation of the mouse experiments, mice had to be bread to the desired genotype (Alb-creERT2;*Glut9*$^{lox/lox}$). Several generations of breeding were required to obtain homozygous Alb-creERT2;*Glut9*$^{lox/lox}$ and *Glut9*$^{lox/lox}$ (without cre) mice to start an experiment. Genotyping for both genes cre and Glut9 loxP was required in all mouse pups. The inheritance of both genes followed simple Mendelian principles.

Genotyping is performed using a polymerase chain reaction (PCR). The principle of PCR is to reproduce a short section of DNA exponentially using a heat stable, DNA-dependent DNA polymerase (Taq

Polymerase). First, the free-floating double stranded DNA is denatured at 94°C. Secondly, the solution is cooled, allowing the abundantly added primers to attach to their complementary sequence (annealing), this step is performed at 59°C. In the third step, the Taq polymerase attaches to the 3' end of the primer and extends the DNA strand complementary to the matrix strand. This final step is done at optimal reaction temperature for the polymerase, in this case at 72°C. The cycle is repeated 38 times, leading to an amplification of $x2^{38}$ of the initial DNA strand. This highly copied piece of DNA can later be made visible, allowing conclusions to be made regarding its original quantity (qPCR) or presence (endpoint PCR). Table 2 shows the temperature program for the genotyping endpoint PCR.

Table 2. PCR program for genotyping

Program	Initial DNA denaturation	Denaturation	Annealing	Extension	Cool down
Repetitions	1	38			1
Target temperature (°C)	94	94	59	72	10
Duration	5 min	30s each			Until temperature is reached

Genotyping was kindly performed by Mrs. Janina Mandelbaum, a medical technical assistant in the Anders working group, as part of the routine genotyping of mice. Young mice, at an age of around 3 weeks, received an ear puncture as a label during the breeding process. With this label, mice could be identified correctly for further breeding after genotyping was performed. The piece of ear tissue removed during labeling was used for PCR genotyping. The punched-out piece of tissue was either stored at -20°C or added directly to 150 µl Direct PCR Tail Peqgold (Peqlab) and 1 µl Proteinase K (Qiagen). This mixture was incubated inside a thermomixer for 3 to 4 hours at 55°C and 800 rpm until the tissue lysis was completed. Subsequent denaturation of proteinase K was achieved by a further incubation the solution at 85°C for 45 minutes. If processed within the next 24 hours, the lysate was stored at 4°C, otherwise it was stored at 20°C.

An endpoint PCR was then carried out for both cre and the Glut9 loxP. For this purpose, a master mix shown in Table 3 was made for each reaction [174]. Each reaction consisted of 24 µl of the master mix and 1 µl of the Lysates and was prepared in 0.2 ml Quali-PCR tubes. The mixture was centrifuged briefly to make sure all the liquid gathers at the bottom of each tube and PCR was then performed under the

conditions given in Table 2 in a Mastercycler R (Eppendorf). The primers used for each reaction are shown in Table 5 and Table 6.

Table 3. Master mix for the endpoint genotyping PCR of one sample

Reagent	Volume (µl)
H_2O	15.3
10x PE Buffer	2.5
11,25 mM dNTPs	4
Forward primer	1
Reverse primer	1
Taq DNA Polymerase	0.2
Total master mix	24
Sample volume	1
Total reaction volume (1 sample)	25

The reaction product was made visible using gel electrophoresis. Here, the samples containing the amplified DNA were run across an agarose gel using a current. The negative charge of DNA caused the molecules to move through the gel toward the cathode, separating the DNA based on the length of the amplified product. To produce a 2% agarose gel, 3 g of agarose were weighed into an Erlenmeyer flask, 150 ml of 0.5 X TRIS-Borate-EDTA buffer (TBE buffer, Table 4) was added and the solution was heated in the a microwave until the agarose was completely dissolved. The solution was cooled to around 60°C inside the Erlenmeyer flask under running water. At this point, 12 µl of pegGREEN, an intercalating DNA dye, was added to the solution. The solution was then poured into the gel chambers, avoiding the formation of any air bubbles.

Table 4. 5x TBE-Buffer

Substance	Concentration (mM)
Tris (hydroxymethyl) aminomethane	890
Ethylene diamine tetraacetate (EDTA) sodium salt	20
Boric acid	890

After 20-30 minutes the gel had hardened and was covered with TBE buffer and placed in the appropriate electrophoresis apparatus. 5 µl of 6X DNA Loading was added to the PCR product. 12 µl of this mixture were pipetted into the gel bag. Together with the samples, a standard DNA latter (Low MW DNA Ladder, New England Biolabs R Inc.), a positive and negative control were pipetted into adjacent gel bags. The DNA latter contains a mix of oligonucleotides with known length and is used to

approximate the base length of the PCR product. The electrophoresis was started using the electrophoresis power supply and run at 200V for 30 minutes. The separated PCR products were then made visible using a UV transilluminator and photographed.

Table 5. Glut9 loxP primers

SL25	5'-CTGTCCAGATGTTGTCTAGG-3'
SL26	5'-CTGTAAACCTCACTCCCTTGG-3'
SL29	5'-GTTATGATGCAGGAGCTTAGC-3'

Table 6. Alb-creERT2 knock-in primers

ABT290	5'-ATCCATTTCTTTGTTTTCAGG-3'
ABV93	5'-GGAACCCAAACTGATGACCA-3'
ABT294	5'-TTAAACAAGCAAAACCAAAT-3'

Table 7. Genotyping PCR Results

Glut9	**+/+**	**flox/+**	**flox/flox**
SL25/Sl29	341 bp	460 / 341 bp	460 bp
SL25/SL26	1684 bp	1684 bp	>2 kbp
Alb-creERT2	**+/+**	**ki/+**	**ki/ki**
ABT290/ABV93	229bp	229bp	-
ABT294/ABV93	-	444bp	444bp

3.3.5 Procedures on mice

Anesthesia

Mice were anesthetized whenever a procedure causes unreasonable pain or stress. Mice were also anesthetized if a procedure required immobilization. This includes taking blood or shaving the back of mice before GFR measurement. Short-term isoflurane inhalation anesthesia was used exclusively in this project. Long-term anesthesia was possible in the laboratory, however for all procedures done in this project only a brief incapacitation of the mice was required. To anesthetize a mouse using isoflurane, the mouse was put into a closed anesthesia chamber and 3% isoflurane in oxygen (4 l/min) were passed into the chamber. Depending on the size and age of the mouse or the desired depth of anesthesia, the animal was left in the chamber for a few seconds to a few minutes. Afterward, the mouse was removed from the anesthesia chamber, the procedure was performed immediately, and the mouse placed back into the cage and observed until it completely woke up.

Blood collection

Blood collection was done during the ongoing experiment and at the end, shortly before the mouse sacrifice. When taking blood during an experiment, only drops of blood were collected by puncturing the tail vein. Care was taken that no more than 5% of the weight of the mouse was removed in blood. As the average mouse weighed around 25 g, no more than 1.25 g of blood was removed. The tail vein puncture was performed without anesthesia. The mouse was led into a small tube, which restricted its motions but allowed for an adequate supply of oxygen. When the tail was fixed to make excessive tail movement impossible, the tail vein was punctured with a 30G needle and the blood drops were collected in 1.5-ml Eppendorf tubes. After the blood was collected, the bleeding was stopped by applying pressure with a sterile gauze. At the end of an experiment, the mice were put into the isoflurane anesthesia chamber until a deep narcosis was achieved. Using a round glass capillary that was open on both sides, the retrobulbar venous plexus was punctured and the blood was collected in 1.5- or 2.0-ml Eppendorf tubes. This way the maximum possible amount of blood was extracted, and the mice were euthanized before awakening from the anesthesia. The collected blood was allowed to coagulate for 1 hour at room temperature. Afterwards, the tubes were centrifuged at 10,000 g for 10 minutes and the blood serum was pipetted into clean Eppendorf tubes. The red blood cells were discarded, and the serum stored for further processing at -20°C.

Urine collection

To calculate the urine UA to creatinine ratio, the UA and creatinine concentrations had to be determined in the urine. To collect the urine samples, the mouse was taken from the cage in a stress-free and quiet environment under a laminar flow mouse handling hood. The mouse was put into the neck handle. A 1.5- or 2.0-ml Eppendorf tube was used as collecting vessel and held close to the mouse genitalia. Using the index finger, the mouse bladder was palpated and gently massaged until the mouse began to urinate into the Eppendorf tube. Once the bladder was empty, the mouse was returned into the cage. At the end of an experiment, the urine collection was performed after the mice were euthanized. Here, the bladder was identified after the abdomen of the sacrificed mouse had been opened. The bladder was then punctured using a syringe with a 30G needle and the remaining intravesical urine was aspirated and transferred into and Eppendorf tube. The sample tubes were labeled and stored at 20°C until further processing.

Intraperitoneal injection

For the mouse experiments in this project, tamoxifen and aristolochic acid had to be administered systemically. This was done via intraperitoneal injection. Before entering the mouse facility, the solution that was to be injected was put into the syringe. A 30G needle was put onto the syringe under

the exclusion of any air bubbles. The mouse was taken out of its cage under a laminar flow mouse handling hood in a quiet environment and put into a neck hold, exposing its abdomen. The needle was introduced into the abdomen in the right lower quadrant and the solution was injected. The injected mouse was watched a few minutes and then returned into the cage.

Measurement of GFR

The glomerular filtration rate (GFR) is a measurement of volume that is filtered by the glomeruli in a given timeframe. It is directly proportional to the number of functioning nephrons in an organism and therefore a very accurate measurement of kidney function. In humans, the GFR can be approximated using equations like the Cockcroft- Gault formula that takes age, sex, serum creatinine, race, and bodyweight into account. In experimental mice, the GFR can be calculated by optically measuring the elimination rate of sinistrin in the bloodstream transcutanously. Sinistrin is a compound that, similar to creatinine, is filtered in the glomerulus and neither reabsorbed nor secreted in the tubulus. For this measurement, sinistrin, coupled with Fluorescein isothiocyanate (FITC), a green fluorescent dye, is injected intravenously into the mouse. The relative intravenous concentration of FITC-sinistrin was measured using a miniaturized light signal sensor that consisted of a light-emitting diode (LED) and a photodetector that were equipped with blue or green bandpass filters. A removable battery pack provided a power source for the light signal sensor.

To prepare for the measurement, the test animal was first subjected to inhalation anesthesia. After a minute, the test animal was removed from the anesthesia chamber and the back hair at the level of the thorax was shaved using a commercially available disposable wet shave razor. The back area that was shorn was approximately 2.5x2.5 cm large. The light signal sensor was attached to its battery pack and it was made sure that the light began flashing. The sensor was then attached to the bare skin of the mouse using a windowed double-sided adhesive tape and additionally secured using a thin strip of leucoplast. This strip of leucoplast encompassed the thorax of the mouse once and care was taken that the shoulder girdle was free so as not to impair movement of the animal. Five minutes after the sensor began recording, the mice were injected with 120 mg/kg bodyweight FTIC-sinistrin solution intravenously. The mice were fixed with the same restrainer that was used for blood collection. The tail vein was sought out using a 1 ml syringe with a 30G needle around 100 µl of solution was administered intravenously. Afterwards, the mice were put into individual, freshly autoclaved cages, where they remained for around 90 minutes until the measurement was complete. The measured fluorescence curves were read on the PC using the MPD-Lab application. The drop in the fluorescence signal over time was used to calculate the plasma half-life of FITC-Sinistrin (Figure 6). The GFR was calculated using an empirically determined conversion factor, the mouse body weight (BW) and the

sinistrin half-life with the formula shown below [175]. Figure 8 shows an example of a FITC fluorescence curve.

$$GFR\ (\mu l/min) = \frac{146.1680\ (\frac{\mu l}{100g\ BW}) * BW\ (g)}{t_{1/2}\ (\text{min})}$$

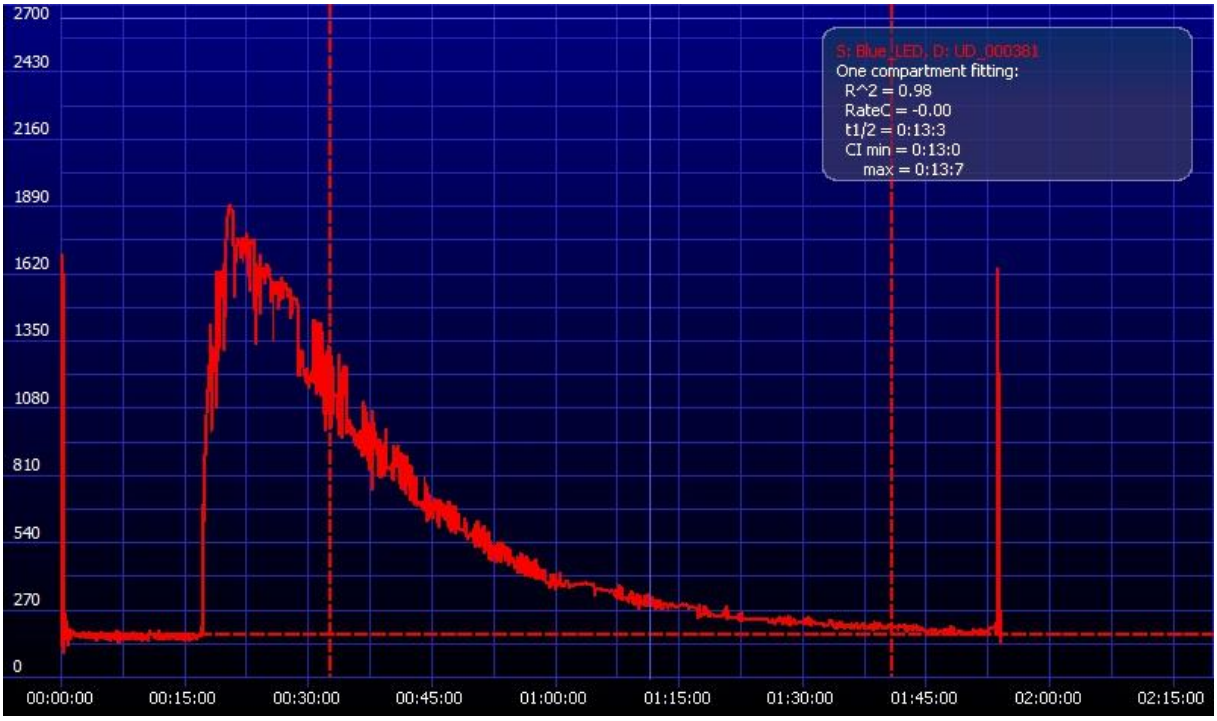

Figure 8. GFR fluorescence curve example of a healthy mouse.
The curve shows the fluorescence intensity (y-axis) measured across time (x-axis). The fluorescence intensity correlates with the amount of sinistrin in the body. The half-life of sinistrin in the mouse body is calculated using a regression model of this fluorescence curve. The GFR of is then calculated using the determined half-life.

Mouse euthanasia and removal of kidneys

The mice were euthanized by cervical dislocation after the experiment was completed. If blood collection was needed, the mice were first anesthetized in the isoflurane chamber. After euthanasia, the abdomen was opened, and the kidneys were visualized and removed. The fibrous kidney capsule was removed gently by peeling using the fingers. The kidneys were photographed if needed and then divided into three parts using a scalpel as shown in Figure 9. The kidney poles for PCR analysis were put into an Eppendorf tubes with 0.5 ml RNAlater, a solution to protect RNA from enzymatic degradation, and then stored at -20°C. The central parts for histology were put into biopsy cassettes and immediately fixed in 4% formaldehyde. The kidney pole used for flow cytometry, labeled as FACS in Figure 9 was processed immediately as described in section 3.4.5.

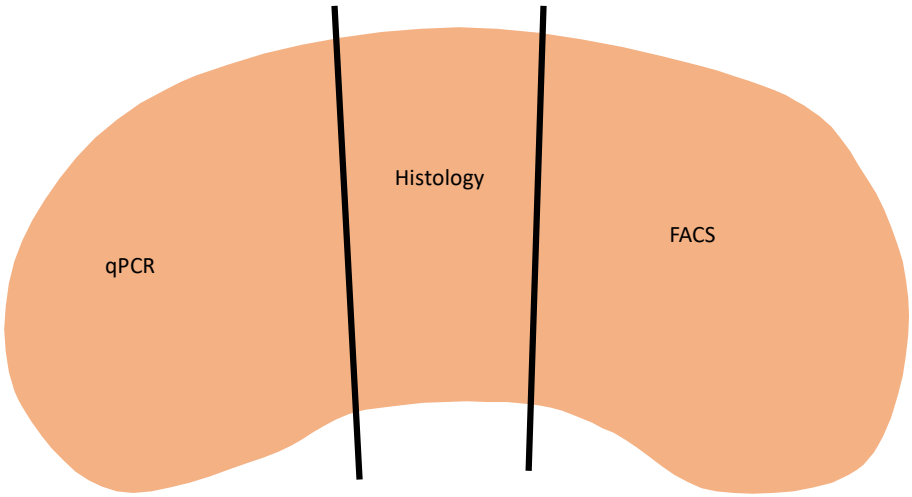

Figure 9. Kidney division for tissue analysis.
The kidneys were cut transversely, a small section in the middle was processed for histological purposes. The larger pole caps were used for RNA isolation and qPCR or for FACS analysis.

3.4 Analytical methods

3.4.1 Analysis of RNA expression by qPCR

A cell requires two large steps to create a protein from an exon sequence of DNA. The first step is the transcription of exon DNA to messenger ribonucleic acid (mRNA). This step is done by DNA dependent RNA polymerases. The completed mRNA travels from the nucleus into cytoplasm. Using cytoplasmatic protein complexes called ribosomes, the second step, translation, is performed. Translation is the decoding of mRNA sequence into a polypeptide chain. This polypeptide undergoes post-translational modification to form the final protein. Both transcription and translation are subjected to a large amount of regulatory processes that the cell uses to control its protein signature. Regulation of transcription happens to such a large extend that the amount of mRNA of a specific protein inside the cell correlates with the amount of protein that a cell generates from that mRNA. For this reason, revere transcription quantitative polymerase chain reaction (qPCR), which is a measurement of the cell's expression a specific mRNA relative to a highly ubiquitous mRNA, is a commonly practiced laboratory method that allows the investigator to draw conclusions about the protein content of a cell or tissue. Three steps are required for the analysis of mRNA expression of a tissue: RNA isolation, reverse transcription, and finally, qPCR.

RNA isolation

All work described below was carried out on ice. Before RNA isolation, all surfaces, pipettes, racks, and other working materials were treated with RNase AWAY® for 20 minutes if possible and then cleaned with 70% ethanol. Work with 2-mercaptoethanol was carried out with appropriate protective clothing

under a fume hood. The RNA was isolated from the above described kidney pole using the PureLink™ RNA Mini Kit (life technologies). The tissue piece stored at -20°C in RNAlater was transferred to a 2 ml Eppendorf tube, which already contained 1.5 ml of the kit's own lysis buffer containing 1% 2-mercaptoethanol. Using the ULTRA-TURRAX R®, the kidney pole was homogenized into a fine liquid suspension for 30 seconds. If necessary, a second homogenization was carried out after 5 minutes. The rotor blade of the ULTRA-TURRAX R® was cleaned with 70% ethanol and then with ddH2O after each processed sample to avoid cross-contamination. 700 µl of the tissue suspension were pipetted into a fresh 1.5 ml Eppendorf tube containing 700 µl of 70% analytical alcohol and vortexed thoroughly for one minute. 700 µl of this mixture was applied to the PureLink™ spin cartridge with integrated RNA-capturing membrane and centrifuged at 12,000 g for 30 seconds. This was repeated until the entire sample had passed through the membrane. The RNA bound to the membrane was washed once with 700 µl of wash buffer 1 by centrifugation at 12,000 g for 30 seconds. 500 µl of wash buffer 2 was added to the membrane and centrifuged at 12,000 g for 30 seconds. The membrane was washed a second time using 500 µl of wash buffer 2. The membrane was then dried by centrifuging at 12,000 g for 2 minutes. The collecting container of the spin cartridge was exchanged for an RNase / DNase-free 1.5 ml Eppendorf tube and 35 µl RNase-free water from the kit was pipetted onto the membrane. The spin cartridge was incubated for 1 min at RT to allow the water to absorb into the membrane. The RNA that was bound to the membrane was eluted in the water by centrifugation at 20,000 g for 2 minutes and collected in the Eppendorf tube. The purified RNA was either stored at -80°C or put on ice for immediate further processing. If possible, transcription to cDNA was initiated immediately after the RNA isolation to lower the risk of enzymatic RNA degradation.

The quality and quantity of RNA extraction was tested using a NanoDrop 1000 spectrophotometer (Thermo Scientific). For this purpose, 1 µl of the sample was examined and the absorbance between 220 and 350 nm was measured. The purity of the sample was estimated using the 260/280 nm ratio. Only RNA samples with a 260/280 ratio of 1.8 to 2.2 were considered pure enough and processed further. Most of the samples used in this project had 260/280 ratio values between 1.95 and 2.19. The NanoDrop also measured RNA concentrations. Samples with concentrations below 150 ng/ml also could not be adequately transcribed to cDNA and were discarded. Most RNA samples isolated for this project contained an RNA concentration of around 1.0 mg/ml.

Reverse transcription to cDNA

In the following step, the isolated RNA was transcribed into complementary DNA (cDNA) using a reverse transcriptase. cDNA is less vulnerable to enzymatic degradation than RNA. Therefore, this step was usually done immediately following the isolation of RNA. The eluted RNA of all samples was dilated with RNase free water to a standardized concentration of 0.133 µg/µl. These dilutions were treated in

a thermocycler (Mastercycler® pro, Eppendorf) for 10 minutes at 65°C to linearize the RNA. Afterwards the tubes were immediately cooled on ice to 4°C and the master mix for the reverse transcription reaction was prepared. The master mix consisted of randomized hexanucleotide primers, an equimolar deoxyribonucleoside triphosphate mix (dNTPs), a reverse transcriptase with its corresponding buffer, an RNase inhibitor, acrylamide and dithiothreitol (DTT). Table 8 shows the composition of the master mix for the reverse transcription reaction of one RNA sample [174]. RT (-) controls were made for each sample using same reagents but without SuperScript™ II Reverse Transcriptase, and in its place the same quantity of ddH_2O. This control was used to make sure no relevant amount of contamination is present in the qPCR samples that could falsify the result.

Table 8. Master mix for the reverse transcription of mRNA to cDNA of one reaction

Reagent	Volume (µl)
RNasin® Ribonuclease Inhibitor	0.5
Hexanucleotide Mix	0.25
dNTPs (25mM each)	0.45
5x First Strand Buffer	4.5
SuperScript™ II Reverse Transcriptase	0.5
Acrylamid 15 mg/ml	0.25
DTT 0.1 M	1.0
Total master mix	7.45
Sample volume (0.133 µg/µl)	15
Total reaction volume (1 sample)	22.45

After the master mix was completed, 15 µl of diluted RNA (a total of 2 µg) were added to 7.45 µl of master mix inside Quali-PCR tubes. The reaction was started in a Mastercycler® pro (Eppendorf) at the conditions described in Table 9 and the final product was stored at -20°C for further processing.

Table 9. Thermocycler conditions for reverse transcription reaction in Thermocycler

Program	Reverse transcription	Reaction termination	Cooling
Repetitions	1	1	1
Target temperature (°C)	42	85	4
Duration	120	5	Until temp is reached

Quantitative polymerase chain reaction

A LightCycler 480 Real-Time PCR system (Roche Diagnostics) using a 96-well plate format was used to quantify the mRNA transcripts of specific target genes in the mouse kidney. This method enables the kinetic quantification of PCR product double strands with the help of the DNA-intercalating green fluorescent dye SYBR® Green I. The emission intensity of SYBR Green forms an exponential curve that emerges from the background earlier the more template cDNA is present. The emission intensity for each sample is determined by the device at the end of each cycle. The cDNA transcribed from mouse kidney RNA serve as templates for the PCR. 3 µl of the previously prepared cDNA was diluted in 126.6 µl RNase and DNase free ddH_2O. Of this diluted cDNA solution, 8.64 µl (corresponding to 0.2 µl undiluted cDNA) were used for one qPCR reaction. For the creation of the master mix, the SYBR Green pre-master mix solution first had to be made. Care was taken that enough of this solution was made to make the gene specific master mix in the next step. Table 10 shows the reagents used to make the pre-master mix solution.

Table 10. SYBR Green pre-master mix solution

Reagent	Volume (ml)
PCR Optimizer	30
10X Taq Buffer without Detergent	15
$MgCl_2$ 25mM	18
ddH2O	9.075
BSA, PCR grade	1.5
dNTPs (25mM je Base)	1.125
SYBRR Green I	0.3
Total	75

Once the pre-master mix solution was made, the gene specific master mix was prepared. Table 11 shows its protocol of preparation for one reaction. The process of making SYBR Green pre-master mix followed by a gene specific master mix was first described in [174].

Table 11. Gene specific master mix solution for one reaction

Reagent	Volume (µl)
Pre-master mix	10
Taq DNA Polymerase	0.16
Forward primer 10 mM	0.6
Reverse primer 10 mM	0.6
Total	11.36

The qPCR was planned on a 96 well plate *in silico*. The cDNA samples were distributed to one per two columns and the genes were distributed to one per row, allowing each sample to have two reactions with each gene primer (duplicates), always including one row with the 18S rRNA gene primer. The RT (-) samples distributed similarly but without duplicates. The expression of each gene was later determined relative to the expression of this "housekeeper" 18S rRNA, as this highly ubiquitous rRNA is expressed by cells at constant rates in all tissues. The design was then carried out on the 96 well qPCR plate. For each reaction, 8.64 µl of diluted sample and 11.36 µl of gene specific master mix was added to one well. After sealing the 96-well Lightcycler plate with a suitable transparent adhesive film (Sarstedt), the plate was centrifuged at 500 g for 30 seconds. The reaction was then carried out in the LightCycler 480 as shown in Table 12.

Table 12. LightCycler 480 program for qPCR

Program	Repetitions	Target temperature (°C)	Duration
Initial DNA denaturation	1	95	5 min
Denaturation	40	95	15 s
Annealing		60	15 s
Extension		68	20 s
Melting curve	1	65 to 95	n.a.
Cool down	1	40	30 s

The quality of each reaction was checked by melting curve analysis. Only samples with a single clearly defined temperature peak were used for crossing point (CP) analysis. The RT (-) controls were checked to make sure no relevant PCR product emerged. The crossing point was determined by the LightCycler® 480 software for each reaction and is equal to the maximum of the second derivative of the exponential fluorescent curve. It corresponds to the cycle number in which the fluorescence signal emerges from the background. Using the mean CP of the duplicates of the target gene and the 18S rRNA, the relative expression of each gene was calculated for each sample using the formula below. This formula assumes that the PCR product doubles in every cycle.

$$Relative\ mRNA\ expression = 2^{-(CP\ 18S - CP\ Target\ Gene)}$$

3.4.2 Measurement of creatinine

Creatinine is a metabolic end-product that is produced in muscular tissue by degradation of creatine phosphate. It is released at constant rates by the muscle, depending on the overall muscle mass. Creatinine is eliminated by the kidney and can be used as a parameter for kidney function. Creatinine is suitable for this because it can only be eliminated by the kidney, it is filtered freely in the glomerulus and it undergoes *virtually* no tubular secretion or reabsorption. Creatinine was measured with the Jaffe reaction using the Creatinine FS (DiaSys) kit. The Jaffe reaction is a colorimetric approach to measuring creatinine. The test sample containing creatinine is exposed to picric acid in an alkaline environment, leading to the formation of creatinine picrate complexes, which induce an orange-red color change that is proportional to the concentration of creatinine in the sample. The kit included a creatinine standard that was used to create a linear standard curve. This standard was tested at different volumes (0, 5, 10, 15, and 20 µl), using ddH_2O to compensate volume differences for the standard reactions. A picric acid containing standard master mix was created using four parts of reagent 1 and one part of reagent 2, both of which were supplied with the kit. Each sample was added at 10 µl per well to a 96 well plate in duplicates. Using a multi-channel pipette, 200 µl of the standard mast mix was added to each well, commencing the reaction. The absorption was measured at 492 nm wavelength after an incubation time of 60 seconds and a second time after and 120 seconds. To analyze the data, the absorption at 60 seconds was subtracted from the absorption at 120s for all samples and standards and the means of all duplicates were calculated. A standard curve was creating using linear regression of the absorption differences of the standard samples. Using this best fit line, the concentration of creatinine in mg/dl was calculated for each sample.

3.4.3 Measurement of blood urea nitrogen

Serum blood urea nitrogen (BUN) was measured in experimental mice as an additional analytical method to approximate kidney function in this project. Urea, similar to creatinine, is a metabolic end product that must be eliminated by the kidney. Urea is created via the urea cycle from the highly toxic ammonia (NH_3). Urea is used by cells as a vehicle to eliminate nitrogen that falls on in protein metabolism. Unlike creatinine, urea does undergo tubular secretion and reabsorption in relevant quantities. However, urea is more sensitive to small changes in kidney function as it does not have a "blind area". BUN was measured indirectly via a double enzymatic conversion using the Urea FS DiaSys kit. The urea in the sample is split in the first reaction by urease into ammonium ions and hydrogen carbonate. In the second step, α-ketoglutarate is aminated using the ammonium ions created in the first reaction by a glutamate dehydrogenase using the redox partner NADPH. The decrease in NADPH concentration can be measured photometrically as a decrease in absorption at 340 nm, which is

proportional to the amount of urea in the sample. The samples were measured undiluted and analyzed according to the manufacturer protocol.

3.4.4 Measurement of uric acid

The UA concentration was measured in the serum as a functional parameter to check knockout induction and to approximate the UA burden of Alb-creERT2;*Glut9*$^{lox/lox}$ mice. It was also measured in the urine to form a urine UA to creatinine ratio as a measurement of the extend of uricosuria. Section 1.2 gives an overview of UA metabolism and hyperuricemia. UA concentration in liquid samples measured using the QuantiChrom™ Uric Acid Assay Kit (BioAssay Systems). The assay contains iron (Fe^{3+}) ions that are reduced to iron (Fe^{2+}) ions in the presence of UA. Fe^{2+} forms a blue colored complex with 2,4,6 - tripyridyl-s-triazine that can be measured photometrically at 590 nm. The absorption is linearly proportional to the concentration of UA in the sample. The serum samples were measured undiluted according to the manufacturer protocol and the UA concentration was calculated using the formula below.

$$UA\ concentration\ \left(\frac{mg}{dl}\right) = \frac{Absorption\ sample - Absoption\ blank}{Absorption\ standard - Absorption\ blank} * 10mg/dl$$

3.4.5 Flow cytometry

Flow cytometry is a method in which cells are characterized by phenotype, size and granularity. The cells are sucked through a narrow microchannel and separated into a single file. The cells are then illuminated by laser beams at different wavelengths and the emission values are assessed using a detector. The forward scattered light (forward scatter) is proportional to the size of the cell, the larger diameter of the scattered light, the larger the cell. The side scatter light allows an assessment of cell granularity and cell surface. The more light is scattered sideways, the more uneven the surface and the higher the granularity of the cell. Additionally, cell surface markers or even intracellular proteins can be detected via labeling with antibodies that are conjugated to fluorescent markers. Depending on the flow cytometer, varying amount fluorescent dyes can be detected. Figure 10 gives an overview of the function of a flow cytometer. Flow cytometry was used in this project to precisely determine the composition of the intrarenal immune cell populations. A FACSCanto II (BD Biosciences) flow cytometer was used in this project. The following flow cytometry protocol was first described in [174].

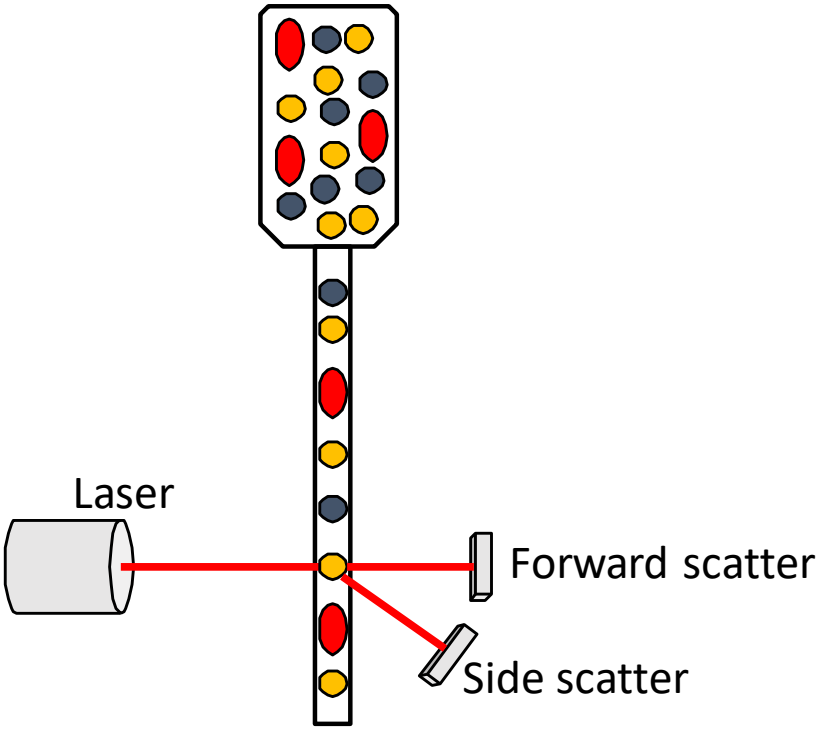

Figure 10. Simplified principle of flow cytometry
The cell suspension is sucked into a microchannel, creating a single file of cells. The laser beam scans each cell individually. The forward and side scatter are determined by individual sensors, providing information about the size, granularity and texture of the cell. Fluorescent labeling of the cell is also detected using this laser.

Sample preparation for flow cytometry

The kidneys were harvested as shown in Figure 9. The piece intended for flow cytometry was put into 2 ml digestive buffer, consisting of 8 mg collagenase and 2000 IU DNase I in PBS. Using the plunger of a 2 ml syringe, the tissue was carefully ground into small pieces. This suspension was incubated at 37°C for 40 minutes. In order to create single cell suspension, the pretreated tissue was passed several times through a 20G and later a 25G needle using a syringe. Finally, the suspension was passed through a mesh filter with a pore size of 70 µm into a 15 ml Falcon tube and 10 ml of PBS were added. The samples were centrifuged at 400 g for 5 minutes and the supernatant was decanted. The cells were resuspended in 5 ml Nycodenz solution. 2 ml of FBS were carefully added to this solution under the formation of a phase boundary. The Nycodenz solution is a density gradient medium, allowing the separation of cells or subcellular organelles based on their relative density. In this case it was used to separate the denser kidney parenchymal cells and any remaining red blood cells from the less dense immune cells. The Nycodenz solution for this purpose was created using the ingredients in Table 13. The probes were centrifuged at 520 g for 20 minutes without using the brake. The immune cells formed a well-defined film between the Nycodenz and FBS phases. The majority of the kidney parenchyma cells remained as a pellet on the bottom of the falcon tube.

Table 13. Nycodenz solution ingredients

Ingredient	Amount
NaCl	9.0 g
TRIS	0.601 g
KCl	0.227 g
EDTA	0.112 g
Nycodenz AG	33.55 g
ddH_2O	1220 ml

The leukocyte film was transferred into a fresh 15 ml Falcon tube, resuspended in 10 ml PBS and centrifuged for 5 minutes at 300 g. The cell suspension was then resuspended in 0.5 to 1.0 ml of PBS and distributed to 5 ml polystyrene falcon tubes. Three 5 ml falcon FACS tubes were filled per sample. One was for an unstained flow cytometer analysis of cells. This analysis was done to determine the autofluorescence of cells in order to perform gating correctly. The second FACS tube was used for antibody staining. Counting beads were added to the third tube of each sample to determine the absolute number of cells in the sample. The cells in the second tube that were subsequently stained with fluorochrome-labeled antibodies were first incubated for 10 min with a zombie NIR dye, an APC-Cy^{TM}7 DNA stain that is unable to penetrate an intact lipid bilayer, staining only DNA of dead cells with permeable cell membranes. The staining was carried out according to the manufacturer's instructions. After staining with zombie dye, 2 ml of FACS buffer were added to each tube. Table 14 shows the ingredients of FACS buffer.

Table 14. Ingredients for FACS buffer

Ingredient	Amount
Phosphate buffered saline (PBS)	500 ml
Bovine serum albumin (BSA)	5 g
Sodium azide	0.5 g

The suspension was centrifuged at 400 g for 5 minutes. The supernatant was decanted, and the cells were resuspended in 2 ml FACS buffer. The cells meant for antibody staining were incubated with anti-CD16 / CD32 (Fc receptor block) for 10 minutes according to the manufacturer’s instructions. The Fc receptor block was done to avoid unspecific, reverse binding of staining antibodies to the Fc receptor. The desired staining antibodies were then pipetted into the tube designated for staining and incubated for 40 minutes. The cells were then washed with 2 ml FACS buffer and centrifuged at 400 g for 5 minutes. The supernatants were decanted, removing any unbound fluorochrome-labeled antibodies. The cells in the unstained tube and in the tube meant for fluorochrome staining were resuspended in

300 µl FACS buffer. The tube for cell counting was resuspended in 100 µl FACS buffer and shortly before measurement, 100 µl of counting beads solution (Life Technologies Corporation) was added.

Compensation, counting, and measurement

Compensation was done on the flow cytometer before measurement using compensation beads according to the manufacturer's instructions (AbC™ Anti-Rat / Hamster Bead Kit). This is a procedure that is important especially if many fluorochromes are used to stain one sample of cells. The fluorescence of the used fluorochrome can spill over and excite sensors measuring at other wavelengths. In compensating, one detects and corrects this spectral spillover and can therefore make more accurate assignments of emission signals to the labeled antibodies and thus to the surface markers. The sensitivity of the detectors for forward and sideward scatter was also adjusted before the measurement, allowing a more optimal assessment of the size and granularity of each measured cell. After these steps had been taken, a gating strategy was conceived using the labeled probes and the fluorochrome labeled cells were measured. Care was taken to ensure that at least 100,000 events were recorded whose forward and sideward scatter profile corresponds to that of immune cells.

In the last and final step of measurement, the samples containing the counting beads were measured. The settings had to be adjusted for this measurement, as the counting beads had a higher signal of side scatter. Care was taken that at least 10,000 counting beads were analyzed by the flow cytometer. The counting bead solution contained the same amount of two different types of counting beads: A and B. These counting beads could be differentiated by the flow cytometer based on a difference in fluorescence properties. Both beads had to be counted at the same rate; if not, the suspension of cells and beads was not homogenous, and the result of the affected probe was not used in the final analysis. Since the quantity of counting beads per sample was known, the exact number of immune cells could be calculated. This in turn allowed the calculation of the quantity of each measured subtype of immune cell. The analysis of data was done using FlowJo software (Tree Star Inc.).

3.5 Histological methods

The preparation of histological samples described below as well as the histochemical staining were kindly carried out by Ms. Janina Mandelbaum and Mr. Dan Draganovici (medical technical assistants, Institute for Clinical Biochemistry, Medical Clinic and Polyclinic IV of the University of Munich).

3.5.1 Formalin fixation and paraffin embedding

As described in section 3.3.5, the middle pieces of the mouse kidneys were used to make histological samples. They were placed inside an embedding cassette and immediately stored in 4% formalin for a total of 24 hours to begin the fixation process. The embedding cassettes were then transferred into a

solution of 70% ethanol, where they remained for a minimum of 5 hours to a maximum of several days. Following this step, the sample was sequentially dehydrated in increasing concentrations of ethanol inside a carousel tissue embedding machine. After the treatment steps with increasing ethanol concentration were completed, the samples were treated in a xylol solution and later in a paraffin solution. The embedding cassettes were removed at the end of the dehydration protocol and embedded in the paraffin at a paraffin pouring station. Using a rotary microtome, the samples were then cut to 2 µm into a water bath. From this water bath, the cut samples were transferred to microscopy slides and dried overnight. The samples were then rehydrated using by performing the dehydration steps in reverse order. The slides were first placed into a xylol solution, then decreasing concentrations of ethanol and finally in distilled water. After the rehydration procedure, the slides were ready to be stained.

3.5.2 Periodic acid-Schiff (PAS), Silver, a Sirius red staining

PAS is a stain that is commonly used to stain kidney samples. It is sensitive in the detection of polysaccharides like glycogen and mucins like glycolipids and glycoproteins, giving these compounds a rich magenta color. The deparaffinated and rehydrated sample cuts were covered with 0.5% periodic acid for 5 minutes, washed with ddH2O and incubated for another 5 minutes with Schiff's reagent. Afterwards the stained slides were washed three times for 2 minutes in a 37°C water bath. A counterstain of hematoxylin was performed to stain the cell nuclei. For this, the slides containing the tissue samples were emerged in hematoxylin staining solution for 2 minutes. Afterwards the stained slides were washed for 5 minutes in warm water. The periodic acid oxidizes vicinal diols in polysaccharides or mucins creating a pair of aldehydes at the tips of the broken saccharide ring. These aldehydes then react with Schiff's reagent to form the magenta color. The hematoxylin nuclear counterstain works as a stain in a basic environment. The staining solution is kept in an acidic environment (pH 3-4). When the slides are emerged into the hematoxylin staining solution, the hematoxylin binds to the anionic phosphate groups within DNA. This binding is strong enough to withstand subsequent washing steps. The rise in pH (to around 7) by the washing with ddH_2O causes the hematoxylin basic stain to turn violet-blue.

The mouse kidney sections in this project were stained for fibrosis using a Sirius red stain. The deparaffinated and rehydrated sample cuts were stained with haematoxylin for 8 minutes, and then washed for 10 minutes in running tap water. The sections were then stained using Sirius red (Direct Red 80, Sigma) according to the manufacturers protocol.

The Jones methenamine silver stain was used to stain human sections for fibrosis. This was performed as part of clinical routine at Nephropath as described in [176]. The silver stain used on the kidney sections for acute UA nephropathy was performed in our laboratory as previously described in [177].

3.6 Statistical analysis

The statistical analysis for the *in vivo* part of this project was performed using Microsoft Excel or GraphPad Prism. The data for the *in vivo* part of this project was shown as the arithmetic mean ± standard error of the mean (SEM). The Kolmogorov-Smirnov test was used to test the data for normal distribution. Student's *t*-test for independent samples was used for the comparison of two groups with normally distributed data. The one-way analysis of variance (one-way ANOVA) was performed if more than two normally distributed groups were statistically compared and Tukey's post-hoc test was used to determine the p-values of comparison between the groups. Non-normally distributed data was compared using the Wilcoxon-Mann-Whitney-test for two groups and the Kruskal–Wallis one-way analysis of variance with the Nemenyi post-hoc-test for three or more groups. The significance level, α, is the probability of falsely rejecting the null hypothesis for a statistical test and was set for this project at 5%. P-values below 0.05 were therefore considered statistically significant and in such cases, the null hypothesis was rejected. P-values above 0.05 were considered not statistically significant and the null hypothesis (no difference between the tested groups) was accepted. The following symbols were used in the graphs to dente different p-values:

n.s. = not statistically significant

* = $p<0.05$

** = $p<0.01$

*** = $p<0.001$

4 Results

4.1 Medullary gouty tophi associate with kidney fibrosis and tubular atrophy

To answer the question whether medullary gouty tophi could be a cause for kidney function impairment, confirmation was first needed that gouty tophi associate with kidney damage in humans. Therefore, a histological case-report based study on the presence of kidney UA tophi in a large cohort of biopsy reports was performed, which has not been done before. The goal was not only to establish the relationship between gouty tophi and histological correlates for CKD such as glomerular and interstitial fibrosis, but also to characterize the cohort and to screen for histological finding that may be associated with medullary tophi that have previously not been described. In collaboration, the Arkana Laboratories database being the world largest collection of written kidney pathology reports was searched. In the first part of this study, a case-control study of these written biopsy reports was designed with the aim to investigate a potential association between kidney impairment and the occurrence of gouty tophi.

4.1.1 Database search and biopsy prevalence of UA tophi

At that time, the Arkana Laboratories database contained a total of 81,200 diagnostic kidney biopsy reports and was searched for “gouty tophi”. This search yielded a total of 84 biopsies in which the nephropathologist found gouty tophi. This made a total gouty tophus prevalence of 0.1% of all biopsies, meaning that 1 in 1000 kidney biopsies contained at least one visible UA tophus. To allow for an adequate statistical comparison and because of this relationship, the same database was searched for biopsy reports of other UA-related pathologies, namely hyperuricemia or hyperuricemia-associated conditions like gout. The reason for having a hyperuricemic control group is to take out the effect of hyperuricemia on observed differences. Hence, all observed differences between the groups must be related to UA tophi and cannot be due to hyperuricemia. The group of biopsy reports with hyperuricemia was very small (115 out of 81,200) compared to what would be expected out of such a large database. The reason behind this is that hyperuricemia had to be reported by the clinician to the nephropathologist together with other relevant clinical information related to the specific case. Preexisting hyperuricemia was often not deemed relevant information by the clinician and was therefore rarely reported. This fact, however, should not lead to any kind of group bias. To have a matching group size, 84 cases were selected at random of the 115 cases with other UA pathologies. Figure 11 provides an overview of the database search. Additionally, pictures and stained and unstained slides with paraffin embedded tissue of kidney biopsies with UA tophi were received from

the Arkana Laboratories. These were used for morphological characterization of the tophus and of related histopathological abnormalities.

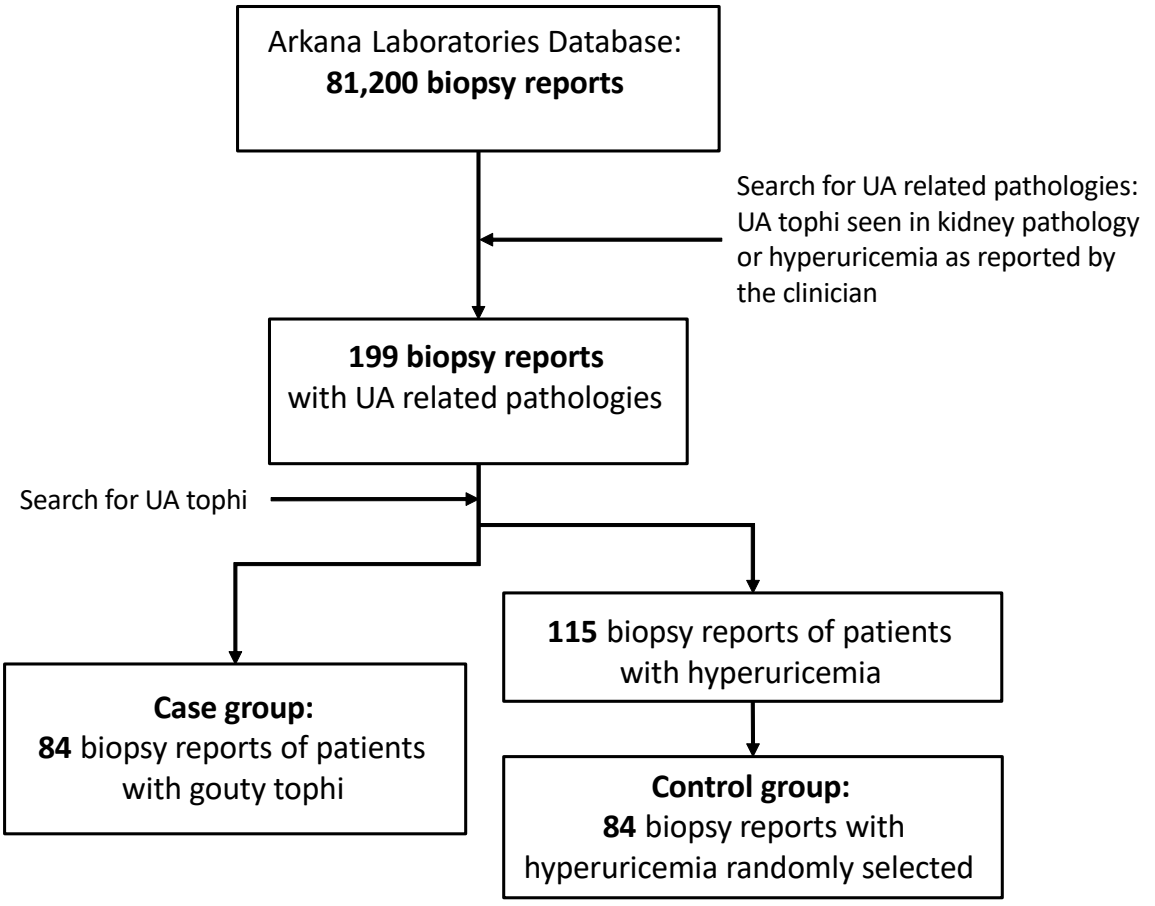

Figure 11. Database search synopsis.
The database of Arkana Laboratories, consisting of a total of 81,200 at the time of search, was searched for biopsy reports with gouty tophi, hyperuricemia, gout, or UA urolithiasis. This search yielded a total of 199 biopsy reports. Of these, 84 reports contained gouty tophi, making up the case group. Of the remaining 115, 84 cases were selected at random to make up the control group of patients with other UA-related pathologies.

4.1.2 Morphology features of human medullary gouty tophi

Typical UA crystal granulomas were identified in all positive biopsies as shown in Figure 12. UA crystal granulomas are most commonly found in the kidney medulla. There are three characteristic layers of a tophus. UA crystals are needle-shaped and form the innermost layer of the tophus and often dissolved upon the fixation process (Figure 12a,c,d,g,h). In other cases the crystal masses remained intact and were visualized directly (Figure 12i), or using polarized light (Figure 12e,g). The UA crystal masses were surrounded by several epithelioid layers of mononuclear cells. Such inflammatory infiltrates consisted mostly of macrophages, some of which fused to create multinucleated giant cells. Figure 12a shows a large giant cell in the process of consuming smaller UA crystals (shown as

intracellular needle shaped clefts). The outmost layer, surrounding the inflammatory infiltrate consists of fibrosis and non-functional kidney interstitium. Figure 12g, a silver stain, shows the black stained fibrosis surrounding clefts and inflammatory infiltrates including multi-nucleated giant cells. Figure 12b and 12c show severely scarred medullary tissue with massive tubular atrophy and PAS-positive intratubular casts surrounding a kidney tophus. Figure 12h shows an aesthetically pleasing star-shaped medullary tophus with a massive surrounding inflammatory reaction. Figure 12i is a low power picture of the bioptic kidney cylinder containing a gouty tophus with undissolved crystals in the top right corner.

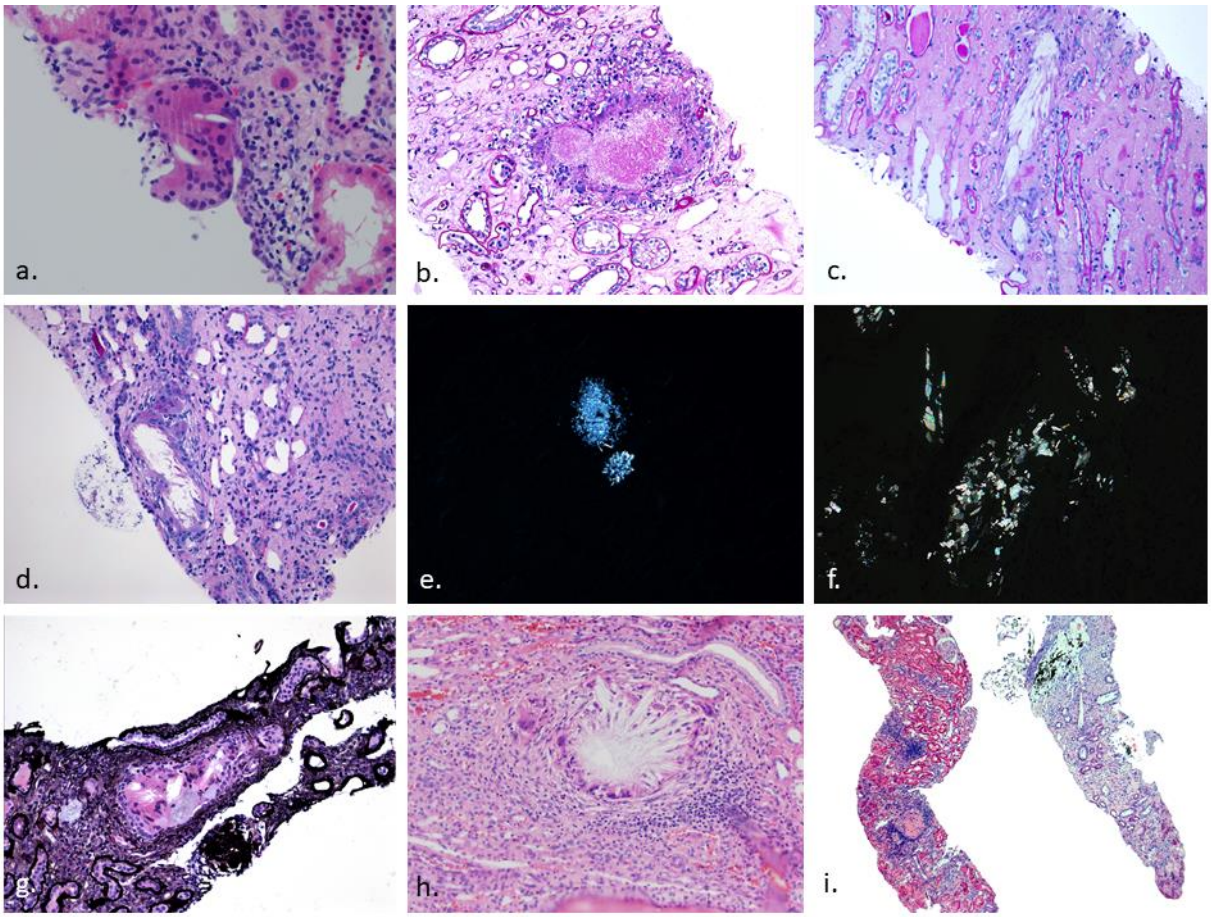

Figure 12. Morphology of human gouty tophi in the kidney medulla.
Hematoxylin and eosin (HE) stains were used in a, d, h, and i. Periodic acid-Schiff reaction (PAS stain) was used in b and c. Silver stain with a basis of hematoxylin and eosin was used in g. E and f show undissolved crystals under polarized light.

4.1.3 Clinical characteristics and main pathological diagnoses

On every pathology report, the age and gender of the patient was reported. Age (p=0.5, t-test) and gender (p=0.63, Fisher's Exact Test) were similar in both groups (Table 15). Some, but not all, pathology reports contained information on the ethnicity of the patient. No comparison was made for Ethnicity due to the lack of Chi-squared distribution (Table 15).

Table 15. Cohort characteristics.
The age in the case group ranged from 16 to 83, with a mean of 52.3. The age in control group ranged from 9 to 78 with a mean of 50.7. The data was compared using the test indicated in the right hand column.

Descriptive Data		w/ Tophi	Control	Total	p=	Test
Age (years)		n=84	n=84	n=168	0.5	t-test
	Range	16 to 83	9 to 78	9.0 to 85.0		
	Mean	52.3 ± 16.5	50.7 ± 15.9	51.3 ± 16.2		
Sex		n=84	n=84	n=168	0.63	Fisher's Exact Test
	Male	56	52	108		
	Female	28	32	60		
Ethnicity	White	26	26	52		
	Black	6	13	19		
	Hispanic	8	3	11		
	Asian	5	3	8		
	Native American	1	0	1		
	Total	46	45	91		

The nephropathologist attributed the kidney damage in every biopsy to one or more main pathological diagnoses. These main pathological diagnoses were diabetic nephropathy (DN, 15.5%), arterionephrosclerosis (ANS, 28.6%), focal segmental glomerulosclerosis (FSGS, 31.5%), IgA nephropathy (IGA, 16.1%), acute tubular injury (ATI, 20.8%), lupus nephritis and other forms of glomerulonephritis (LN+GN, 13.7%), tubulointerstitial nephritis (TIN, 7.1%), lymphoproliferative related renal disease (LPRRD, 3.6%), thrombotic microangiopathy (TMA, 2.4%), and other pathologies (9.5%) (Figure 11). There was no distinction between primary and secondary FSGS. The differences in prevalence of the individual diagnoses between the groups were compared using Fisher's Exact Test. Diabetic nephropathy (p=0.018) and acute tubular injury (p=0.022) were significantly less prevalent in the group with UA tophi than in the control group. Otherwise, the main pathological diagnoses were similar in both groups. No biopsy report carried solely the diagnosis 'gouty nephropathy'. In all patients with medullary tophi, there was at least one other underlying main diagnosis. Often the biopsy reports carried more than one main pathological diagnosis, making the total more than 100% within each group.

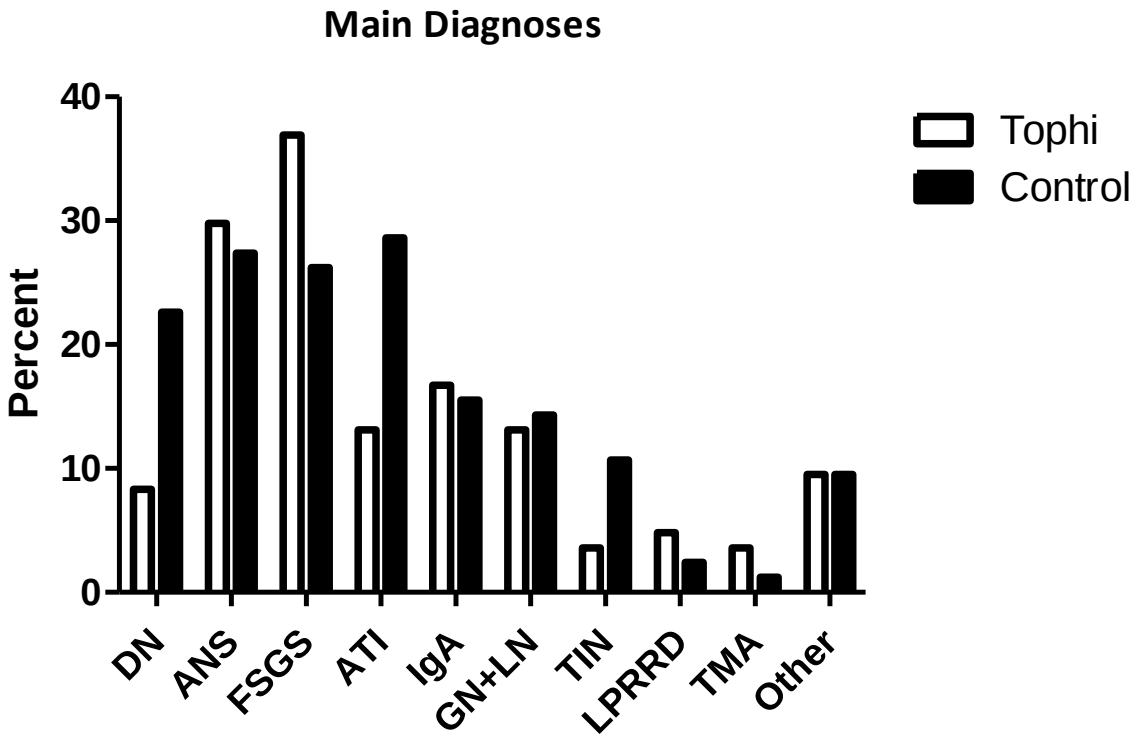

Main diagnoses	Tophi n=84	Control n=84	Total n=168	p=
Diabetic nephropathy	8.3%	22.6%	15.5%	0.018
Arterionephrosclerosis	29.8%	27.4%	28.6%	0.865
Focal segmental glomerulosclerosis	36.9%	26.2%	31.5%	0.184
Acute tubular injury	13.1%	28.6%	20.8%	0.022
IgA Nephrophathy	16.7%	15.5%	16.1%	1
Lupus nephritis and other glomerular diseases	13.1%	14.3%	13.7%	1
Tubulointerstitial nephritis	3.6%	10.7%	7.1%	0.131
Lymphoproliferative-related renal disease	4.8%	2.4%	3.6%	0.682
Thrombotic microangiopathy	3.6%	1.2%	2.4%	0.62
Other	9.5%	9.5%	9.5%	1

Figure 13. Main pathological diagnoses
In all biopsy reports, the nephropathologist gave one or more main pathological diagnosis. The most frequent diagnoses were arterionephrosclerosis (ANS), focal segmental glomerulosclerosis (FSGS), and acute tubular injury (ATI). The prevalence of each diagnosis was compared between the two groups in a 2x2 spread using Fisher's exact test.

4.1.4 Medullary gouty tophi associate with glomerulosclerosis and interstitial fibrosis

In describing the kidney biopsy, the examining nephropathologist counted all visualized glomeruli including globally and segmentally sclerosed glomeruli. To approximate the ratio of glomerular lesions in the biopsied kidney, the number of globally sclerosed glomeruli visualized was divided by the total number of glomeruli visualized. Likewise, the total number of segmentally sclerosed glomeruli visualized was divided by the total number of glomeruli visualized to form the ratio of glomeruli with segmental lesions. Significantly more global glomerulosclerosis was found in the biopsies with gouty tophi than in the control group (Figure 14a). However, there was no difference in segmental lesions between the two groups (Figure 14b). Interstitial fibrosis was graded semi-quantitively by the nephropathologist, each biopsy received a score of none, mild, moderate, or severe interstitial fibrosis. Biopsies with gouty tophi were more likely to have moderate or severe interstitial fibrosis and less likely to have no or mild interstitial fibrosis than biopsies without tophi (Figure 14c). These findings indicate that gouty tophi are associated with substantial kidney atrophy.

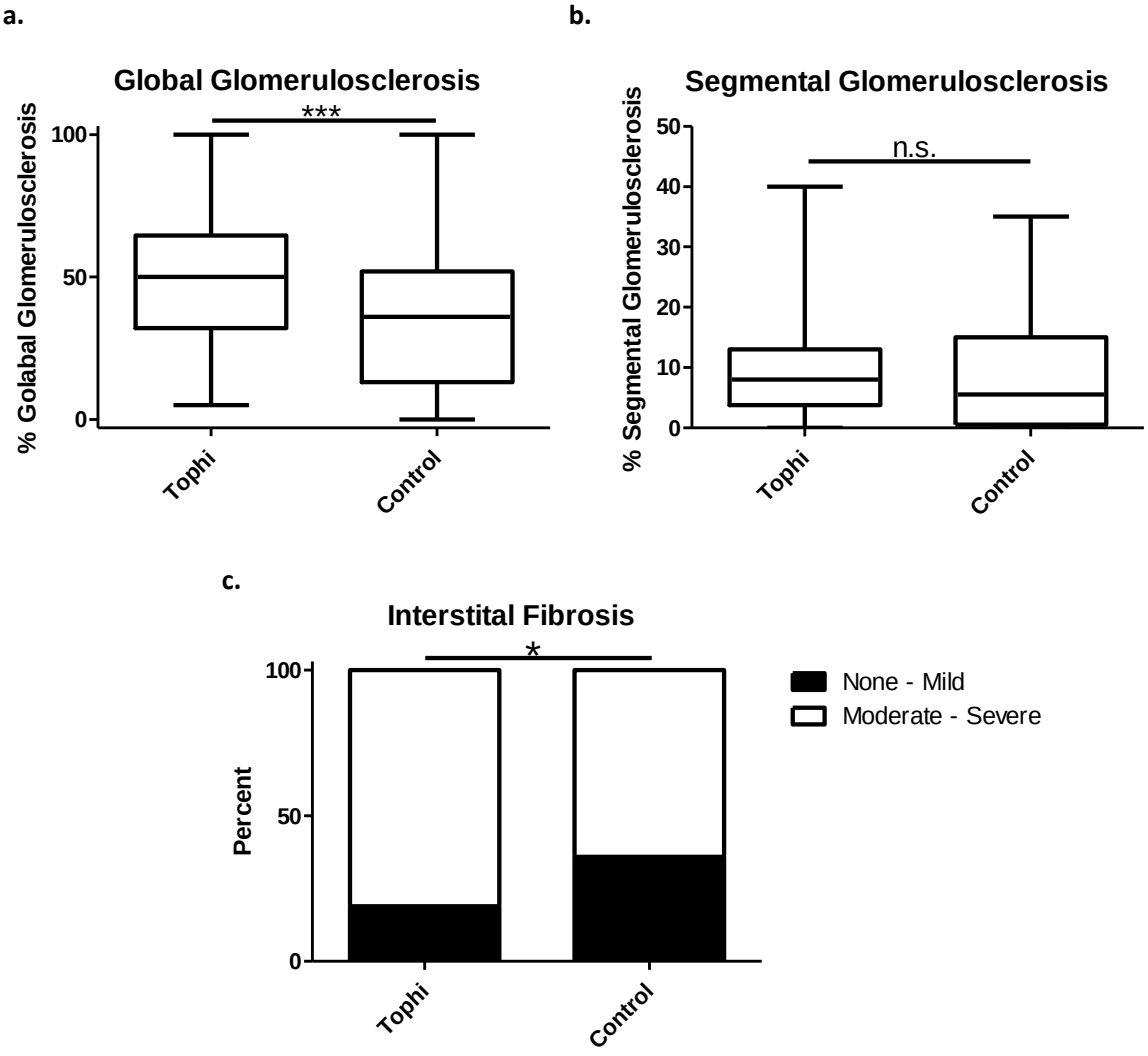

Figure 14. Gouty tophi associate with kidney fibrosis.
(a) The ratio (in percent) of global glomerulosclerosis was formed by dividing all globally sclerosed glomeruli by the total number of glomeruli visualized and multiplying by 100. The percent global glomerulosclerosis was compared using the Mann-Whitney-U test. (b) Similarly, the percent ratio of segmental sclerosis was formed by dividing all segmentally sclerosed glomeruli by the total number of glomeruli visualized and multiplying by 100. The two groups were also compared using the Mann-Whitney-U test. (c) Interstitial fibrosis was graded by the nephropathologist as none, mild, moderate, or severe. The distribution was compared on a 2x2 spread using Fisher's Exact Test. The graph shows the distribution of each trait in percent of the total number of cases in each group. n.s. = not statistically significant, * = $p<0.05$, *** = $p<0.001$

4.1.5 Gouty tophi associate with arteriosclerosis but not arteriolosclerosis

The examining nephropathologist graded the severity of arteriosclerosis and arteriolosclerosis visualized on the biopsy as none, mild, moderate, or severe. Using the chi-squared test for trend, (Cochrane-Armittage trend test) the severity of arteriosclerosis and arteriolosclerosis between the two groups was compared. Biopsies with tophi contained more arteriosclerosis than biopsies without (Figure 15a). However, there was no difference in the severity of arteriolosclerosis (Figure 15b). These findings indicate that gouty tophi associate with (macro)-vascular aging.

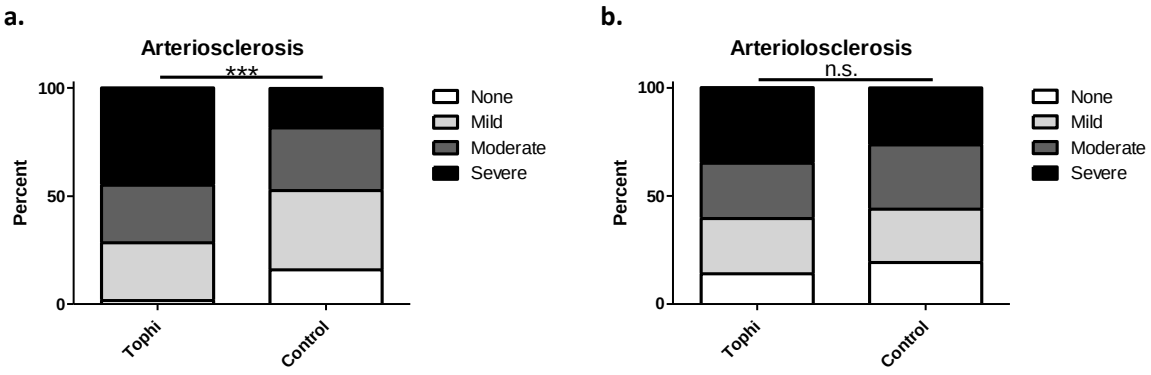

Figure 15. Gouty tophi associate with macrovascular aging.
The degree of arteriosclerosis (a) and arteriolosclerosis (b) was graded none, mild, moderate, or severe by the nephropathologist. The groups were compared using the chi-squared test for trend (Cochrane Armitage test for trend). The graphs show the distribution of severity as percent of the total number of biopsies in each group. n.s. = not statistically significant, *** = $p<0.001$.

4.1.6 Gouty tophi associate with foot process effacement but not with GBM thickening

On electron microscopy, the nephropathologist examined the severity of podocyte foot process effacement and thickness of the glomerular basement membrane. The severity of foot process effacement was also scored as none, mild, moderate, or severe. The glomerular basement membrane (GBM) thickness was measured and regarded either normal or thickened. There was significantly more podocyte foot process effacement in the gouty tophi group than in the control (Figure 16a). Foot process effacement is typical of proteinuric diseases such as FSGS, minimal change disease, IgA nephropathy, or diabetic nephropathy [178]. The rate of GBM thickening was similar in both groups as shown by Fisher's exact test (Figure 16b). GBM thickening is an early change in kidneys of patients with diabetic nephropathy [179].

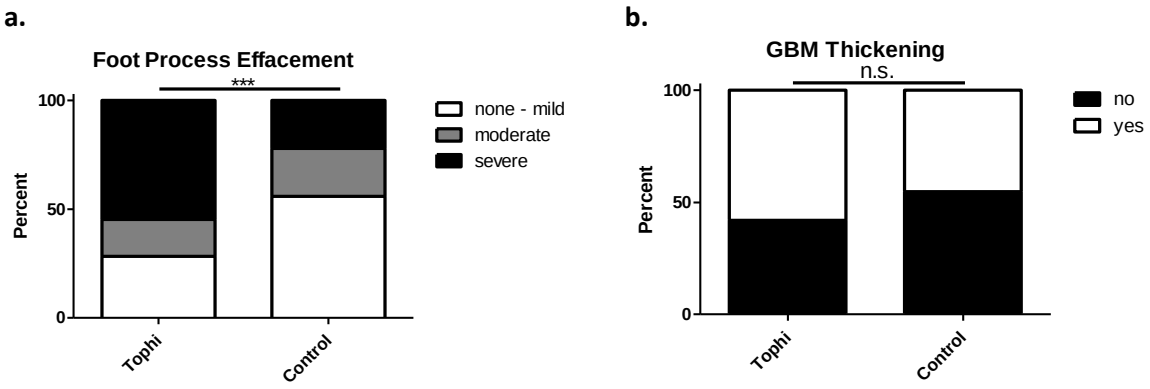

Figure 16. Foot process effacement and glomerular basement membrane thickening.
The examining nephropathologist rated glomerular foot process effacement and GBM thickening viewed with electron microscopy as none, mild, moderate, or severe. The groups were compared using the chi-squared test for trend (Cochrane Armitage test for trend). The graphs show distribution of foot process effacement (a) or GBM thickening (b) as percent of the total number of biopsies of each group. n.s. = not statistically significant, *** = p<0.001

4.1.7 Gouty tophi associate with proteinuria but not with increased serum creatinine

Although the previous medical history of the patients was limited to the information that was given to the nephropathologist by the clinician, the serum creatinine (in mg/dl) and the amount of proteinuria (in g/day) was reported often enough for statistical comparison. Patients with gouty tophi (n=25) had significantly more proteinuria than patients in the control group (n=24) (Figure 17a). This fits to the finding of increased podocyte foot process effacement in the gouty tophi group. There was no significant difference in serum creatinine between patients with tophi (n=60) and the control group (n=71) (Figure 17b).

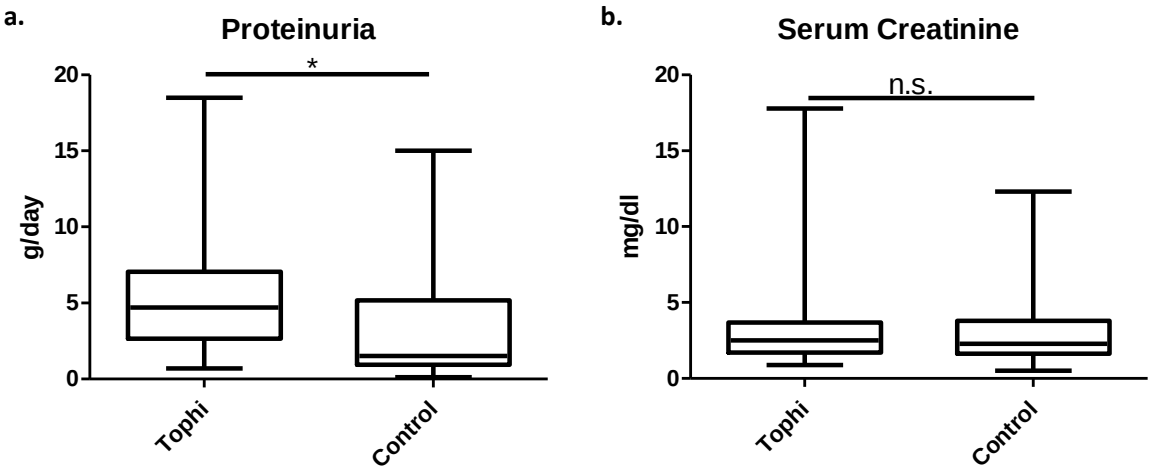

Figure 17. Proteinuria and serum creatine at time of biopsy.
The attending physician provided laboratory values of proteinuria (a.) and serum creatinine (b.) to the nephropathologist in many cases. The two groups were compared using the Mann-Whitney-U test. Box-and-whisker plots show arithmetic mean, one standard deviation and range of data. n.s. = not statistically significant
* = $p<0.05$ vs control cohort.

4.2 Establishment of a new mouse model of UA nephropathy

To further investigate the pathogenesis of chronic UA nephropathy and the relationship between medullary tophi and kidney atrophy, a suitable animal model is needed. The aim of the second part of the study was to establish an animal model capable of forming UA crystal deposits that resembles hyperuricemia-related UA crystalluria and chronic UA nephropathy. First, the previously established model of acute UA nephropathy in mice [168] was analyzed regarding its ability to induce chronic kidney changes like fibrosis, serving as a comparison with the later created model of chronic UA nephropathy.

4.2.1 Uric acid crystalluria but no fibrosis or granuloma formation in mice with acute uric acid nephropathy

One group of Alb-creERT2;*Glut9*$^{lox/lox}$ and one group of *Glut9*$^{lox/lox}$ mice were injected with tamoxifen as described in section 3.3.2. The mice were kept on standard chow diet for the entire duration of the experiment (45 days). Afterwards the mice received an inosine gavage of 100µg of inosine/day for 3 days and were sacrificed on day 45. Alb-creERT2;*Glut9*$^{lox/lox}$ mice that received inosine developed hyperuricemia and azotemia as indicated by a significant increase in serum UA (Figure 18a) as well as BUN (Figure 18b) and creatinine (Figure 18c) levels compared to the *Glut9*$^{lox/lox}$ control mice after inosine gavage on day 48. UA crystals were found in the urinary sediment of inosine-treated Alb-creERT2;*Glut9*$^{lox/lox}$ mice (Figure 18e) but not in the control mice (Figure 18d). In addition, unfixed

frozen kidney sections showed precipitation of polarizable UA crystals inosine-treated Alb-creERT2;*Glut9*$^{lox/lox}$(Figure 18f and g), indicating that these mice developed crystalluria.

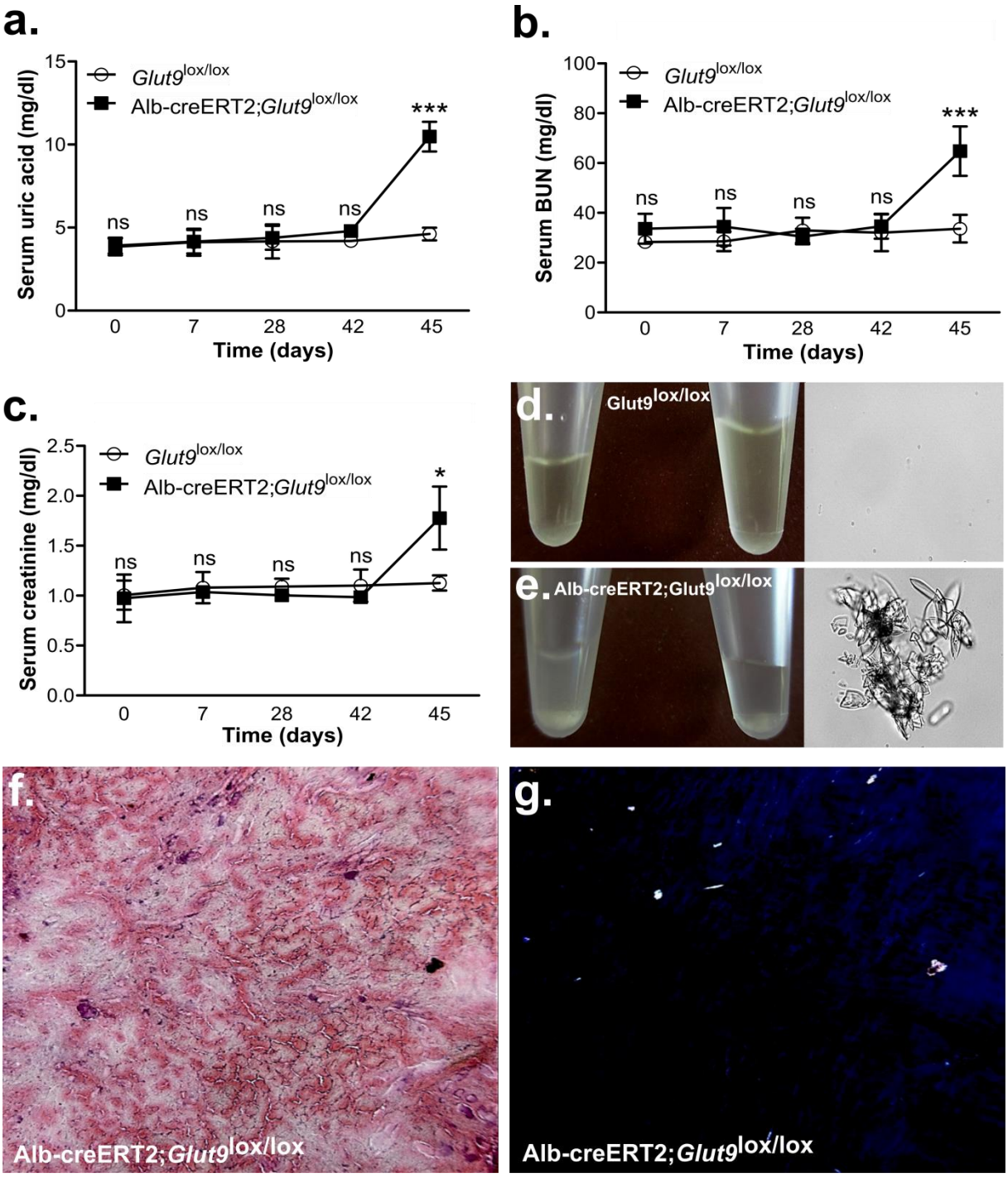

Figure 18. Induction of hyperuricemia, crystalluria, and azotemia in mice with acute UA nephropathy
Serum UA (a) serum BUN (b) and serum creatinine (c) were measured at day 0 (before Tamoxifen induction) and at days 7, 28, 42, and 45 of the experiment. In Alb-creERT2;*Glut9*$^{lox/lox}$ mice, a urinary precipitate is found (d and e). Within this precipitate, UA crystals were found upon microscopy of the urinary sediment (d and e). Polarizable UA crystals were found in the kidney parenchyma upon microscopy of frozen sections of Alb-creERT2;*Glut9*$^{lox/lox}$ kidneys. All groups were compared using a t-test. ns = not statistically significant, * = p<0.05, *** = p<0.001.

Next, kidney sections were fixed, stained, and analyzed under a microscope. Figure 19 shows sample sections of both groups. Only mild changes related to AKI-like tubular dilation and injury were observed on PAS-stained kidney sections from inosine-treated Alb-creERT2;*Glut9*$^{lox/lox}$ mice (Figure 19b) compared to the control group (Figure 19a), which was in line with an increased mRNA expression of the kidney injury marker *KIM-1* and the inflammation marker *Tnfα* and *Il*6 (Figure 19c).However, no fibrosis or UA tophi were observed in inosine-treated Alb-creERT2;*Glut9*$^{lox/lox}$ mice as indicated by silver stain (Figure 19d and e) as well as mRNA expression levels of the fibrosis marker fibronectin 1, Fsp1 and Mmp9 (Figure 19f). The data indicate that short-term administration of inosine induced acute UA nephropathy associated with kidney injury and inflammation but without fibrosis and tophi formation.

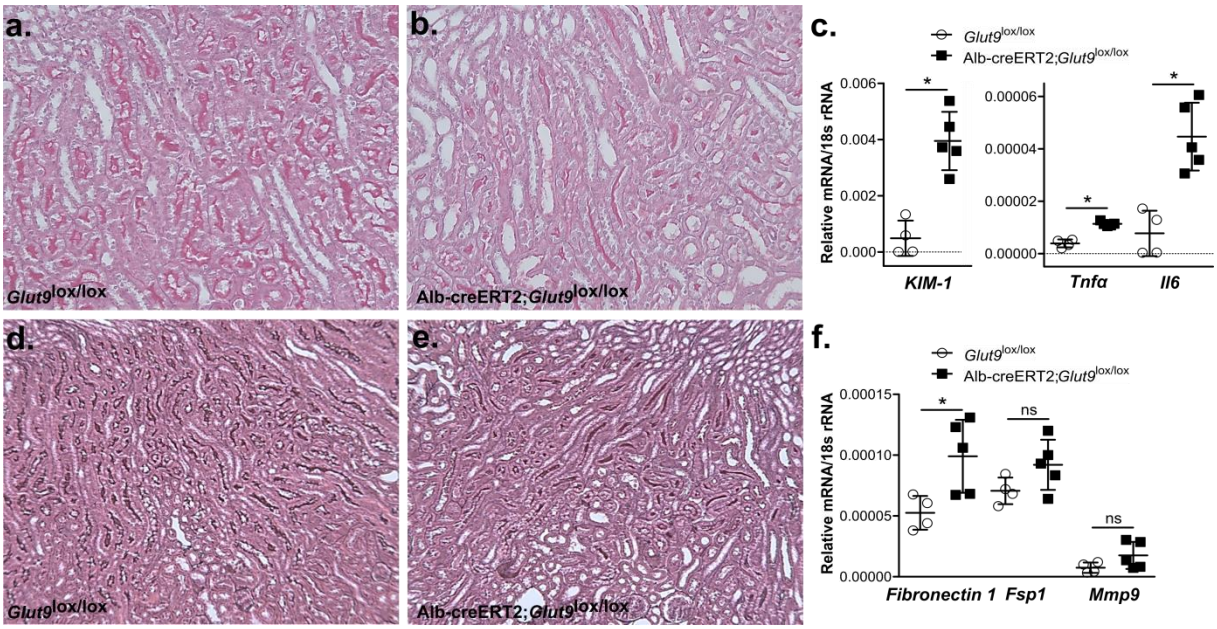

Figure 19. No tophus formation or fibrosis evident in acute UA nephropathy.
(a-b) Kidney sections were fixed and stained using a PAS-Stain. (d-e) Corresponding kidney sections were stained using a fibrosis silver stain. (c and f) RT-qPCR was performed for KIM-1, *Tnfα*, *Il6, Fibronectin 1*, *Fsp1,* and *Mmp9.* n=5 mice per group. Data are mean ± SEM. ns = not statistically significant, * = p<0.05.,

4.2.2 Long-term exposure of Alb-creERT2;*Glut9*$^{lox/lox}$ mice to an acidogenic diet and inosine causes hyperuricemia with crystalluria and chronic uric acid nephropathy.

In order to create a mouse model for chronic UA nephropathy, three experimental groups were used: 1) Alb-creERT2;*Glut9*$^{lox/lox}$ mice that received tamoxifen injections and were placed on a ACD with inosine (Tam, ACD+Ino), 2) Alb-creERT2;*Glut9*$^{lox/lox}$ mice with tamoxifen injections and chow diet with inosine (Tam, Chow+Ino), and 3) Alb-creERT2;*Glut9*$^{lox/lox}$ mice with vehicle injections and ACD with inosine (Veh, ACD+Ino, as described in section 3.3.2). All three groups showed normal serum UA concentrations at around 5 mg/dl at week 0 (baseline). However, serum UA concentrations significantly increased in mice injected with tamoxifen and placed on a chow diet (Tam, Chow+Ino) or ACD enriched with inosine (Tam, ACD+Ino) up to 6 weeks (Figure 20a), indicating that both groups

developed hyperuricemia compared to vehicle-treated mice (Veh, ACD+Ino). In addition, only tamoxifen-injected mice on a ACD diet (Tam, ACD+Ino) showed a significant increase in serum BUN levels (Figure 20b) and a significant diminished GFR (Figure 20c) over time compared to the other two groups. The data indicate that for Alb-creERT2;*Glut9*$^{lox/lox}$ mice to develop hyperuricemia and CKD, first tamoxifen is required to turn of Glut9, second inosine supplementation to induce hyperuricemia, and third an ACD with inosine to induce a decline in kidney function.

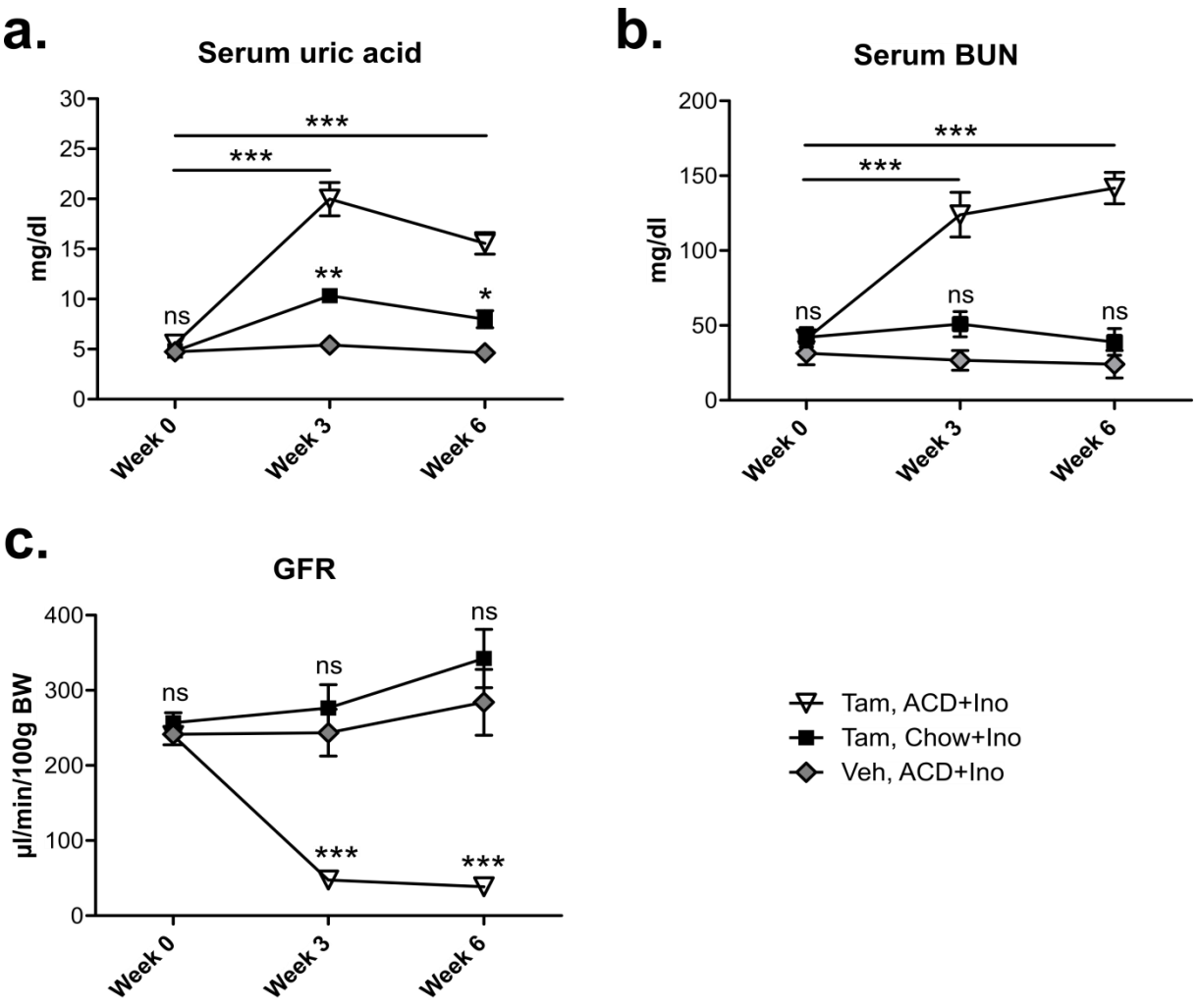

Figure 20. Elevated UA, blood urea, and decreased GFR in tamoxifen-induced mice.
At the end of weeks 0, 3 and 6, tail vein bleeds were collected from all mice. The serum concentrations of UA (a) and of BUN (b) were measured at these time-points. Similarly, transcutaneous measurement of GFR was performed at these timepoints (c). All groups were compared using a one-way ANOVA. P-values were calculated using Tukey's post-hoc test. Differences between time points were calculated using a t-test. n.s. = not statistically significant, * = $p<0.05$, ** = $p<0.01$ *** = $p<0.001$.

4.2.3 Low urinary pH causes uric acid crystalluria in Alb-creERT2;*Glut9*$^{lox/lox}$ mice fed an acidogenic diet with inosine

Reports have shown that a low urine pH promotes the crystallization of soluble UA and the development of UA crystal nephropathy [168]. To investigate whether urinary crystallization is responsible for the deteriorated kidney function in Alb-creERT2;*Glut9*$^{lox/lox}$ mice that were fed an ACD with inosine (Tam, ACD+Ino), the urine was checked in these mice. Indeed, light microscopy revealed crystal deposits in the urine of these mice after 6 weeks (Figure 21–before). Rasburicase, a clinically used recombinant uricase, which exclusively dissolves UA crystals, was added into the urine. The crystals completely dissolved in the presence of rasburicase after 5 minutes, confirming that the urine contains UA crystals (Figure 21). Whether the ACD contributes to tubular occlusion of UA crystals via lowering the urinary pH was tested using a pH electrode. As shown in Figure 22, Alb-creERT2;*Glut9*$^{lox/lox}$ mice that were fed an ACD showed a lower urinary pH than Alb-creERT2;*Glut9*$^{lox/lox}$ mice on a standard chow. Thus, an acidic urine pH contributes to the precipitation of soluble UA; therefore, UA crystal formation is likely the mechanism for the observed kidney impairment in ACD-fed hyperuricemic mice.

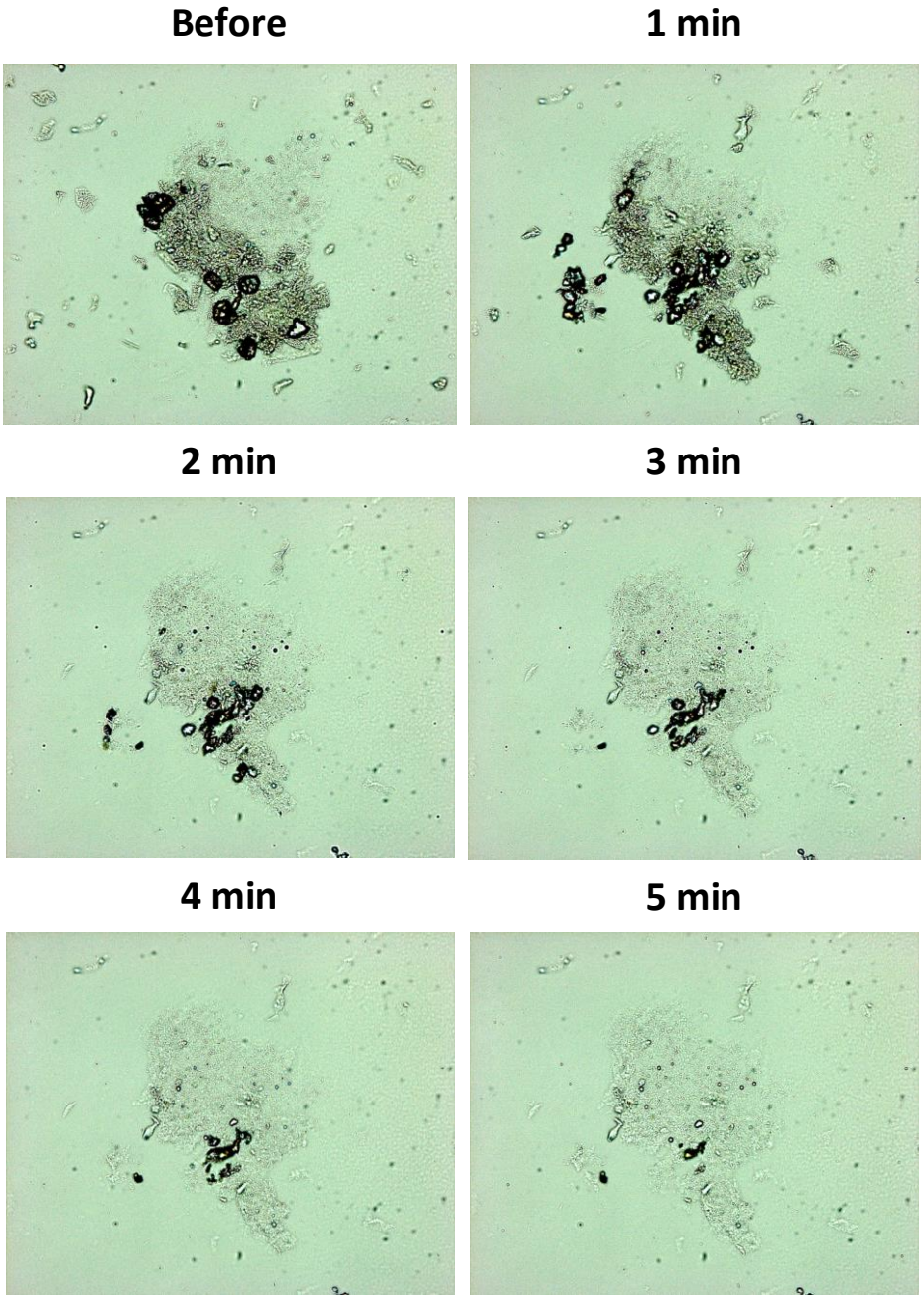

Figure 21. Rasburicase completely dissolved urinary crystals confirming the composition of uric acid. Urine from a mouse of the tam, ACD group at week 6 was pipetted onto a glass microscope slide. A urinary crystal was focused under a microscope and the before picture was taken. Rasburicase (1µl) was added and pictures of the same crystal were taken after 1, 2, 3, 4, and 5 minutes [180].

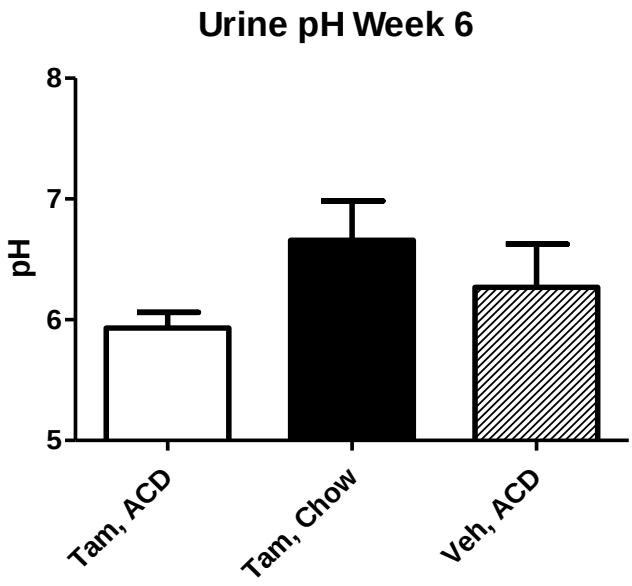

Figure 22. Lower urinary pH in mice fed an acidogenic diet.
The urinary pH was measured at the end of week 6 using a microelectrode. The urinary pH was lower in the ACD with inosine fed mice compared with mice fed a standard chow diet.

4.2.4 Hyperuricemia and uric acid crystalluria lead to macroscopically visible kidney remodeling

After sacrifice, kidneys were checked for macroscopic abnormalities in hyperuricemic mice with crystalluria (Tam, ACD+Ino), mice with asymptomatic hyperuricemia without kidney impairment (Tam, Chow+Ino), or healthy mice (Veh, ACD+Ino). Kidneys from hyperuricemic mice with UA crystalluria were smaller in size and had a rough and pale cortex with white crystal deposits (Figure 23, left image), while the kidneys from the hyperuricemic as well as healthy group appeared both morphologically normal (Figure 23, middle and right image).

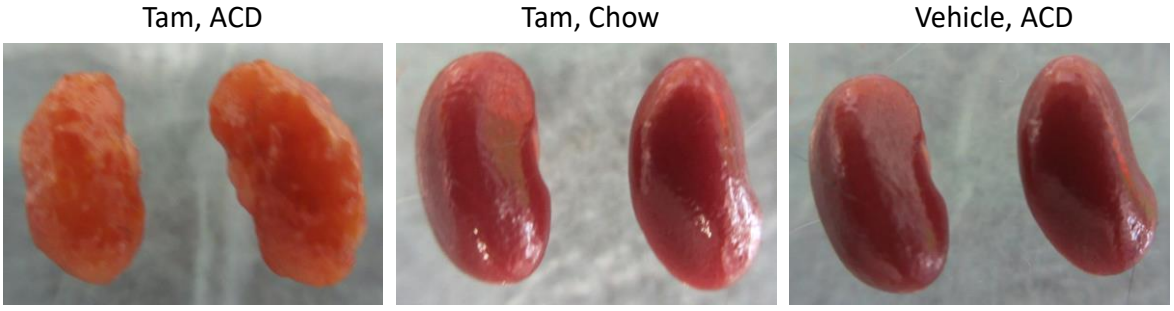

Figure 23. Macroscopic kidney morphology
Immediately following mouse sacrifice, the kidneys were removed and freed of their fibrous capsule. Representative photographs were taken to display kidney morphology of each group [180].

4.2.5 Hyperuricemia with crystalluria induced kidney injury in Alb-creERT2;*Glut9*$^{lox/lox}$ mice

To assess the extent of kidney injury between the three groups, total mRNA was isolated from the kidneys and RT-qPCR analysis for the kidney injury marker *KIM-1* performed after 6 weeks (as described in section 3.4.1). As shown in Figure 24, mRNA expression levels for KIM-1 were significantly upregulated in hyperuricemic mice with crystalluria (Tam, ACD+Ino) compared with hyperuricemic mice (Tam, Chow+Ino) and healthy mice (Veh, ACD+Ino), indicating that hyperuricemia with UA crystalluria induces kidney injury but not asymptomatic hyperuricemia alone.

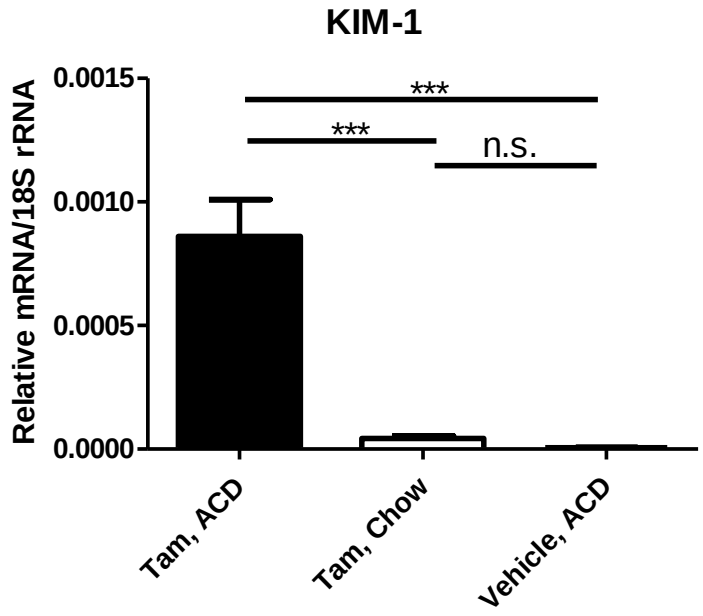

Figure 24. KIM-1 mRNA level is elevated in hyperuricemic mice with uric acid crystalluria.
Total kidney mRNA from all three groups of mice (Tam, ACD+Ino; Tam, Chow+Ino; Veh, ACD+Ino) was isolated and RT-qPCR for *KIM-1* performed (n=5 per group). The data was compared using a one-way ANOVA. P-values were calculated using Tukey's post-hoc test. n.s. = not statistically significant, *** = $p<0.001$.

4.2.6 Increased infiltration of immune cells and inflammation in mice with hyperuricemia and crystalline nephropathy

CKD is not only associated with kidney injury but also with the infiltration of immune cells including macrophages, dendritic cells, neutrophils, monocytes, and T cells. To characterize the different immune cell population in more detail, flow cytometric analysis of single cell suspensions was performed as described in section 3.4.5. The kidney cells were stained with antibodies against CD45, CD11b, CD11C, F4/80. Figure 25a shows the gating strategy for CD45+ CD11b+ CD11c-F4/80^{high} cells that were identified as macrophages, for CD45+ CD11b+ CD11c+ F4/80^{low} cells that were identified as dendritic cells, and for CD45+ CD1b- CD11c- F4/80^{low} cells that were classified as other immune cells. s Mice with hyperuricemia associated crystalline nephropathy (Tam, ACD+Ino) showed a significantly elevated number of infiltration CD45+ F4/80^{high} and CD45+ F4/80^{low} macrophages (Figure 25b and c)

compared with hyperuricemic and healthy mice (Figure 25b and c). The same was the case for the subpopulation of CD45+ F4/80^{high}CD11c^{low} macrophages and CD45+ F4/80^{low} CD11c^{high} dendritic cells (DCs) (Figure 25d-f). Corresponding to the functional data, no significant difference in the number of infiltrated immune cells was observed between the hyperuricemic (Tam, Chow+Ino) and healthy group (Veh, ACD+Ino).

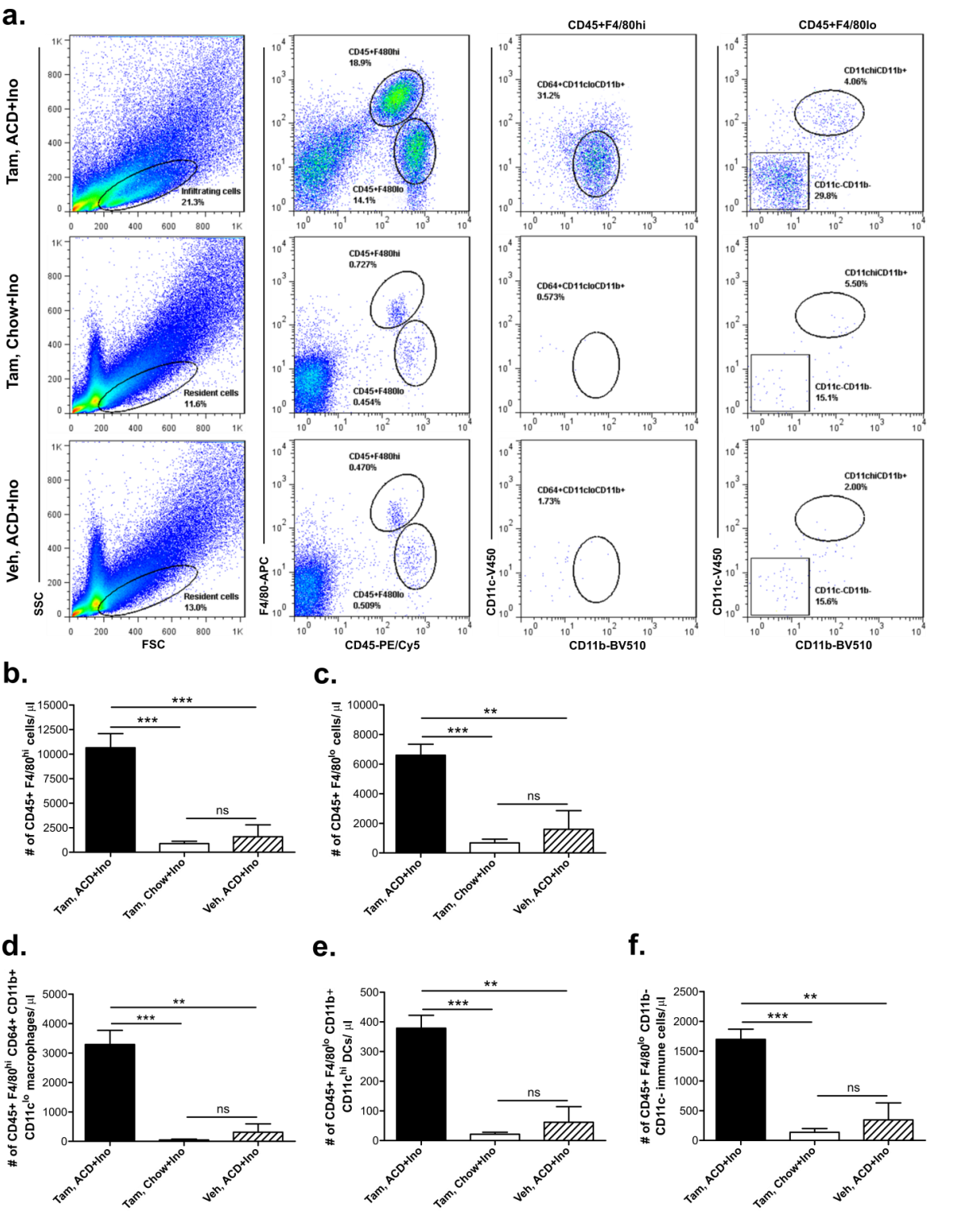

Figure 25. Increased macrophage and dendritic cell infiltration in hyperuricemic mice with uric acid crystalluria.

After sacrifice (n=5 mice per group), a portion of the kidney was used to create a single cell suspension. These cells were fixed and stained with the aforementioned antibodies and analyzed using the gating strategy shown in a. CD45+ and F4/80^{low} / F4/80^{high} cells were gated in and further quantified in regard to their CD11b and CD11c status. (b and c) The number of CD45+ and F4/80$^{low+high}$ monocytic-derived cells per µl of single cell suspension in each group. (d) The number of CD45+ and F4/80^{high} CD11c^{low} subpopulation, corresponding to macrophages. (e) The number of CD45+ and F4/80^{low} CD11c^{high} subpopulation, corresponding to DCs. (f) The number of CD45+ and F4/80^{high} CD11c- subpopulation. All groups were compared using a one-way ANOVA. P-values were calculated using Tukey's post-hoc test. n.s. = not statistically significant, * = p<0.05, ** = p<0.01, *** = p<0.001.

Furthermore, monocytes, neutrophils, NK cells, and T cells were also characterized in experimental kidneys by flow cytometry. The cells were stained with antibodies against CD45, CD11b, Ly6C, Ly6G, CD4, and CD8. Figure 26a shows the gating strategy. Similar as observed for the CD45+ F4/80^{high} CD11c^{low} macrophages and CD45+ F4/80^{low} CD11c^{high} DCs, the CD45+ CD11b- and CD11b+ cells (Figure 26b and e) and their subpopulations were also significantly increased in hyperuricemic mice with crystalluria (Tam, ACD+Ino), while no significant differences were observed between the two control groups. This was also the case for the number of CD45+ CD11b+ Ly6C- Ly6G+ neutrophils (Figure 26c), CD45+ CD11b+ Ly6G- Ly6C+ monocytes (Figure 26d), and all CD45+ CD11b- T cells, including the CD4+ and CD8+ T cell subpopulations.

To further quantify the extend of kidney inflammation, RT-qPCR was performed on kidney samples as described in section 3.4.1 using primers for *Tnf-α* and *Il6*. There was an increase in mRNA expression of *Tnf-α* (Figure 27a) and *Il6* (Figure 27b) in the group with hyperuricemia and UA crystal nephropathy compared with the hyperuricemic or healthy group . No significant difference was observed between the hyperuricemic (Tam, Chow+Ino) and healthy (Veh, ACD+Ino) groups. Taken together, the mRNA data corresponded to the findings that were observed by flow cytometry showing that the kidney injury in hyperuricemic mice with UA crystalluria associates with inflammation and immune cell infiltration.

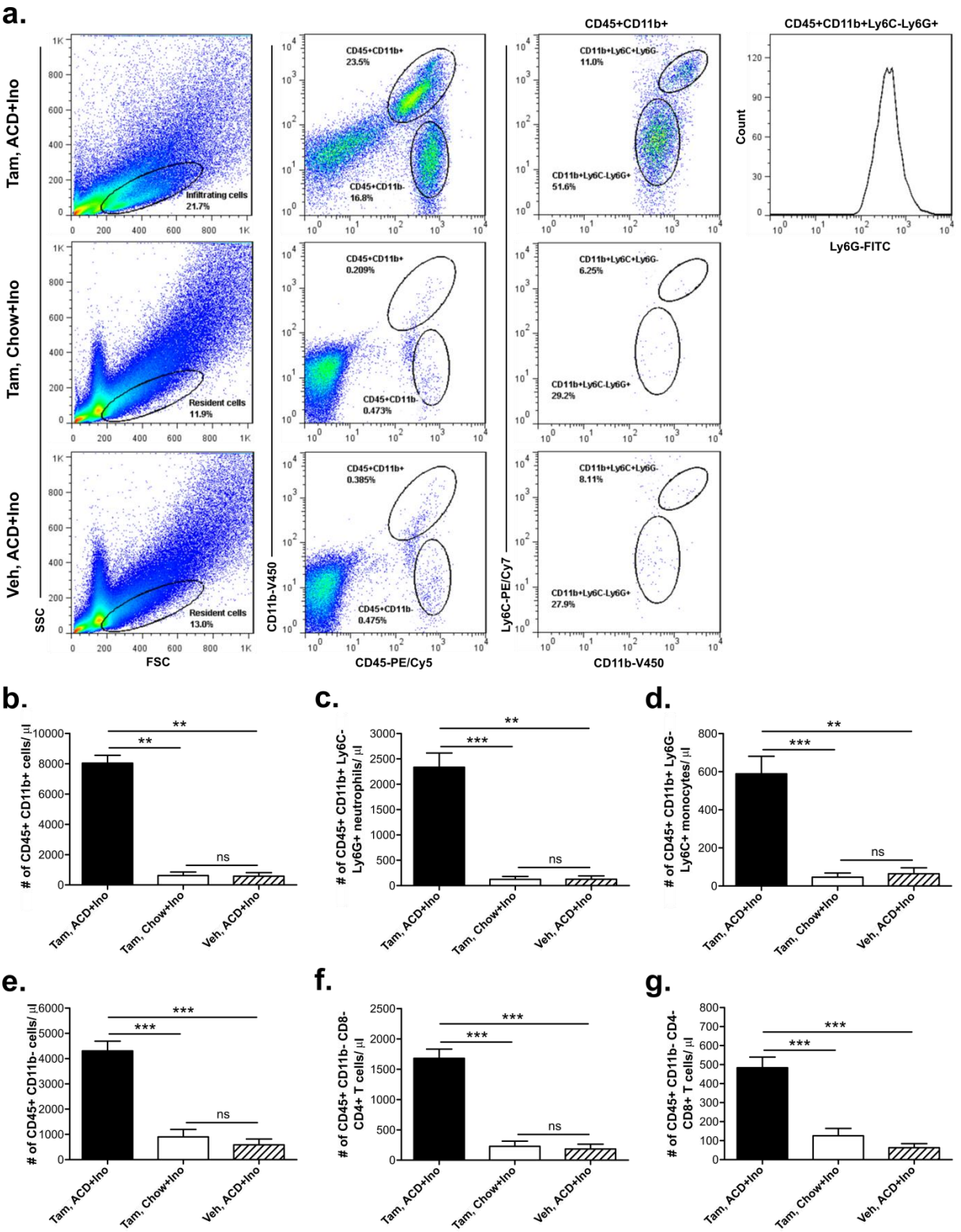

Figure 26. Neutrophils, monocytes and T cells infiltrate in high numbers in the kidneys of mice with hyperuricemia and uric acid crystalluria.

Kidneys (n=5 per group) were prepared a described in section 3.4.5. (a) Gating strategy that was used to identify CD45+ CD11b- and CD11b+ cells. (b) The number of infiltrating CD45+ CD11b+ cells in the kidney. (c and d) The number of CD45+ CD11b+ Ly6C- Ly6G+ neutrophils (c) and CD45+ CD11b+ Ly6G- Ly6C+ monocytes (d). (e-g) The number of CD45+ CD11b- lymphocytes (e) and that of CD4+ T cells (f) and CD8+ T cells (g). All groups were compared using a one-way ANOVA. P-values were calculated using Tukey's post-hoc test. n.s. = not statistically significant, ** = $p<0.01$, *** = $p<0.001$.

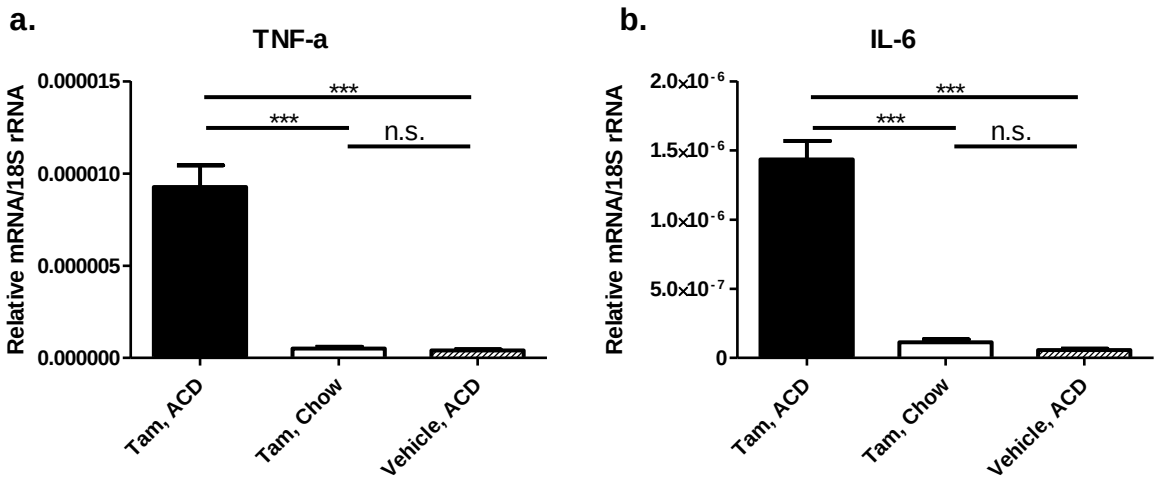

Figure 27. Elevated expression of *Tnf-α* and *Il6* mRNA levels in mice with hyperuricemia and crystalline UA nephropathy.
(a and b) Total mRNA was isolated from kidneys of all three groups of mice after 6 weeks (n=5 per group) and RT-qPCR for *Tnf-α* (a) and *Il-6* (b) performed. All groups were compared using a one-way ANOVA. P-values were calculated using Tukey's post-hoc test. n.s = not statistically significant, *** = p<0.001.

4.2.7 Formation of interstitial uric acid tophi and extensive fibrosis in hyperuricemic mice with crystalluria

To investigate whether hyperuricemia and UA crystalluria contribute to interstitial fibrosis and induce the formation of UA tophi (UA crystal granulomas), kidneys from all three groups of mice were fixed and embedded in paraffin after sacrifice, and stained for PAS as described in section 3.5. Kidney sections from hyperuricemic mice with crystalluria (Tam, ACD+Ino) revealed massive tubular dilation and PAS-positive intratubular casts (Figure 28a, left), indicating acute tubular injury to distal nephrons. No intratubular casts, tubular dilation, tubular atrophy, or fibrosis were observed in both control group (Figure 28a, middle and right). Furthermore, tubular atrophy and massive string-like broadening of the interstitium were present as sings of advanced chronic kidney fibrous conversion. Within the broadened fibrous interstitium, UA tophi were only observed with a small crystal cleft and surrounding inflammatory infiltrate in hyperuricemic mice with crystalluria (black arrows, Figure 28b), while UA crystal granulomas were absent in both control groups. Of note, kidneys from healthy mice (Veh, ACD+Ino) did not show any signs of histological abnormalities, the corticomedullary junction with cylindrical tubular epithelium in the cortex appeared normal and the PAS-positive apical glycocalyx remained completely intact compared to the Tam, ACD+Ino group, suggesting that an ACD with inosine alone does not induce kidney damage in mice, where Glut9 is still active (Veh, ACD+Ino).

To determine the extent of interstitial fibrosis, RT-qPCR was performed for the fibrosis markers *Collagen 1α1 (Col-1)*, *Fibronectin 1*, and *FSP-1*. Figure 28c shows elevated mRNA expression levels of

all three fibrosis-related genes *Col-1*, *Fibronectin 1*, and *FSP-1* in mice with hyperuricemia and UA crystal nephropathy (Tam, ACD+Ino) compared to the control groups. This is further evidence for fibrotic remodeling that was observed macroscopically (Figure 23) and microscopically (Figure 28a). Taken together, the data demonstrate that kidney UA tophi form as a result of UA crystal precipitation in an acidic urine leading to UA crystal-induced tubular injury, inflammation and interstitial fibrosis. Therefore, only hyperuricemia with UA crystalluria but not asymptomatic hyperuricemia causes CKD.

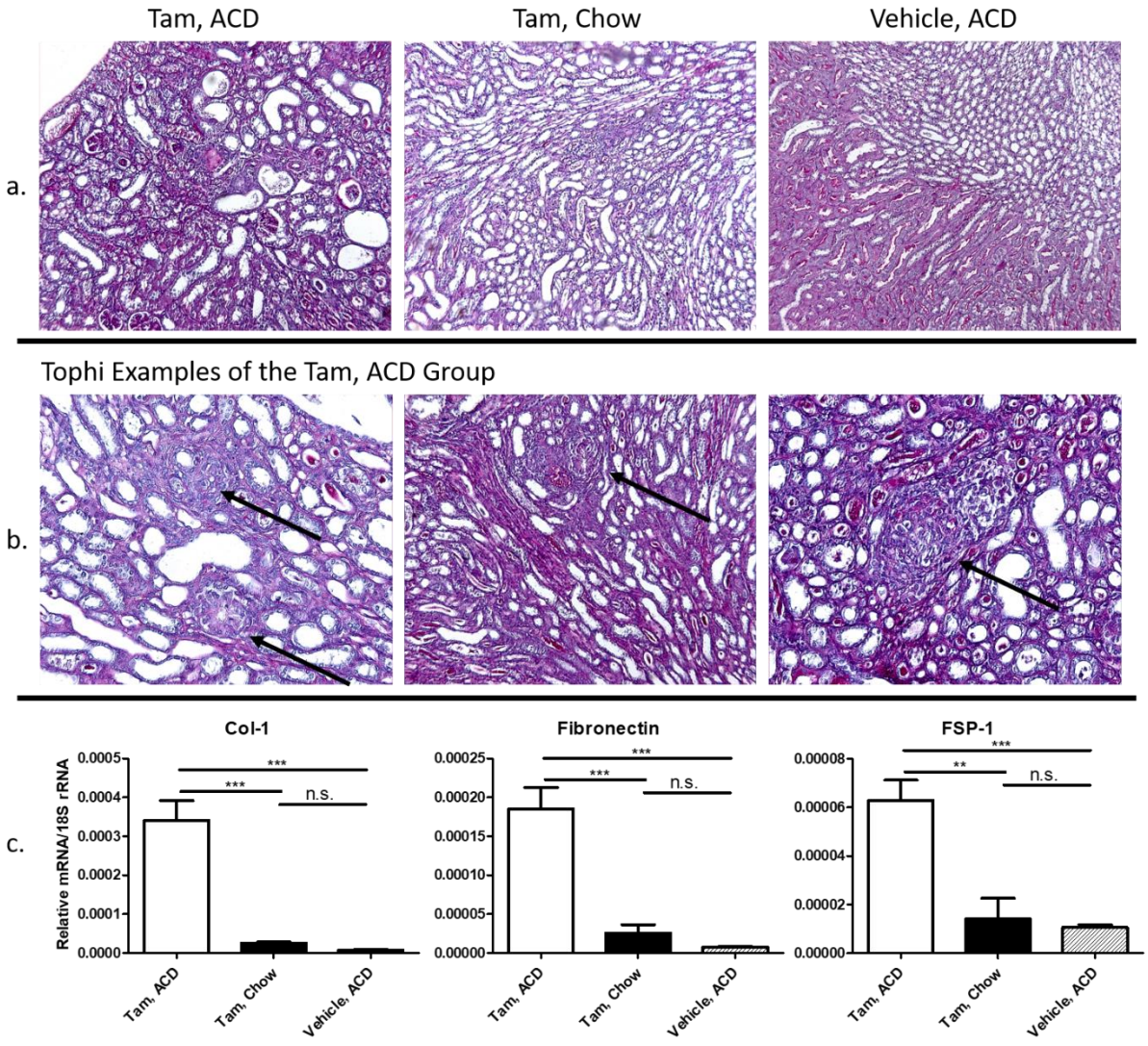

Figure 28. Severe interstitial fibrosis and tophus formation in ACD fed hyperuricemic mice.
(a and b) The kidneys were fixed in formalin and ethanol and later embedded in paraffin. The paraffin blocks were cut and stained using a PAS stain. Representative pictures of each experimental group were taken at 100x magnification. Black arrows indicate UA tophi. (c) Total mRNA expression levels of the fibrosis marker *Col-1*, *Fibronectin 1*, and *FSP-1* (n=5 per group). All groups were compared using a one-way ANOVA. P-values were calculated using Tukey's post-hoc test. n.s = not statistically significant, ** = $p<0.01$, *** = $p<0.001$.

4.3 Asymptomatic hyperuricemia does not affect the progression of aristolochic acid-induced chronic kidney disease

That hyperuricemia with UA crystalluria but not asymptomatic hyperuricemia alone drives CKD with subsequent granulomatous interstitial nephritis has been demonstrated in section 4.2. However, whether asymptomatic hyperuricemia can contribute to the progression of pre-existing CKD has been subject of debate since many years due to the lack of experimental evidence, e.g. a suitable animal model of asymptomatic hyperuricemia with clinically relevant serum UA concentrations.

4.3.1 Hyperuricemia does not alter the progression of aristolochic acid-induced chronic kidney disease

To investigate whether asymptomatic hyperuricemia contributes to CKD progression, Alb-creERT2;*Glut9*$^{lox/lox}$ and *Glut9*$^{lox/lox}$ control mice were injected with AAI to induce a progressive form of non-crystalline CKD or vehicle as control (as described in section 3.3.3). All three groups of mice were placed on a chow diet supplemented with inosine for 42 days. Serum was collected from mice at baseline and after 42 days to determine UA and BUN levels, and GFR measured. At baseline, serum UA levels ranged between 4-6 mg/dl in all three groups (Figure 29a). However, the serum UA levels significantly increased to 12-20 mg/dl in Alb-creERT2;*Glut9*$^{lox/lox}$ that were placed on a chow diet with inosine (group A – HU+CKD and group C – HU only), whereas *Glut9*$^{lox/lox}$ control mice had normal serum UA levels (group D – CKD only). This indicates that Alb-creERT2;*Glut9*$^{lox/lox}$ mice developed asymptomatic hyperuricemia as no crystals were found in the urine of these mice (group A and C). Furthermore, Alb-creERT2;*Glut9*$^{lox/lox}$ and *Glut9*$^{lox/lox}$ mice that received i.p. injections of AAI (groups A and B) were found to have significantly elevated BUN levels at day 42 compared to group C (Figure 29b). In order to precisely assess the effect of asymptomatic hyperuricemia on kidney function, a transcutaneous GFR measurement using FITC-labeled sinistrin was performed as described in section 3.3.5. GFR measurements were carried out at baseline, on day 21 and day 42 (Figure 29c). As expected and based on the BUN analysis, a diminished GFR was found in AAI-injected mice (group A and B), whereas no GFR decline was observed in mice with asymptomatic hyperuricemia only (group C). Importantly, no difference in GFR was found between mice with asymptomatic hyperuricemia and AAI-induced CKD (group A) and mice with only AAI-induced CKD (group B) at either 21 days or 42 days (Figure 29c). This shows that asymptomatic hyperuricemia does not affect kidney function in mice with preexisting CKD.

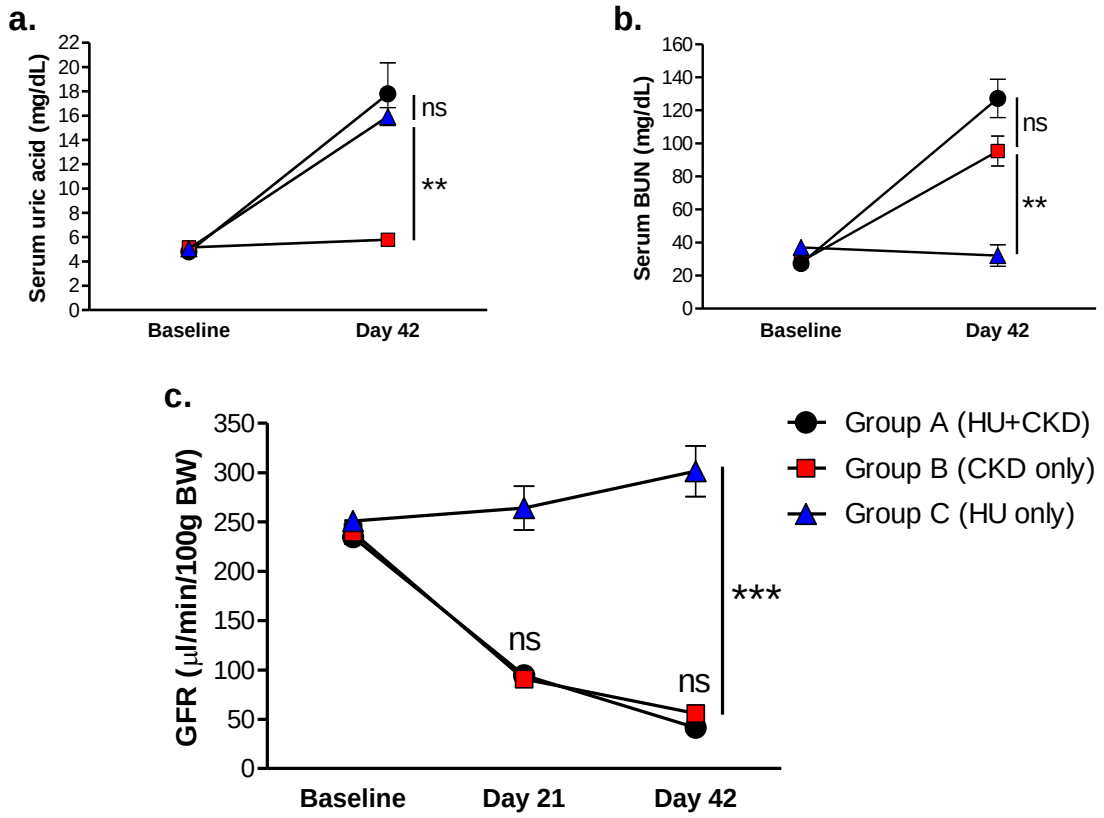

Figure 29. Asymptomatic hyperuricemia does not affect kidney function in aristolochic acid-induced nephropathy.

Alb-creERT2;*Glut9*$^{lox/lox}$ and *Glut9*$^{lox/lox}$ control mice were injected with aristolochic acid I (AAI) to induce CKD or vehicle as control. All three groups of mice were placed on a chow diet with inosine for 42 days. (a and b) Serum uric acid (a) and BUN (b) in hyperuricemic mice with AAI-induced CKD (HU+CKD, group A), in mice with AAI-induced CKD (CKD only, group B), and hyperuricemic mice without CKD (HU only, group C). (c) GFR was measured at baseline, day 21 and day 42 (n=5 mice per group). The data from day 42 was compared with a one-way ANOVA and the p-values were calculated using Tukey's post-hoc test. n.s. = not statistically significant, ** = p<0.01.

4.3.2 Asymptomatic hyperuricemia does not further aggravate tubular injury and fibrosis in mice with pre-existing chronic kidney disease

Finally, tubular injury and interstitial fibrosis was evaluated in all three groups of mice. PAS staining showed similar severe signs of acute tubular injury, including extensive formation of PAS positive casts, flattening of tubular epithelium, dilatation and atrophy between both groups of mice with AAI-induced CKD (group A and B, Figure 30, top panel), while no injury was observed in mice with only hyperuricemia (group C, Figure 30, middle panel). In addition, Picro-sirius red staining was carried out to look at the extend of fibrosis. The Picro-sirius red staining revealed interstitial fibrosis in group A and B but not in group C (Figure 30, bottom panel). No UA tophus formation was observed in any group compared to previously noticed in Figure 28b. Thus, asymptomatic hyperuricemia does not affect the progression of AAI-induced CKD in mice.

a.

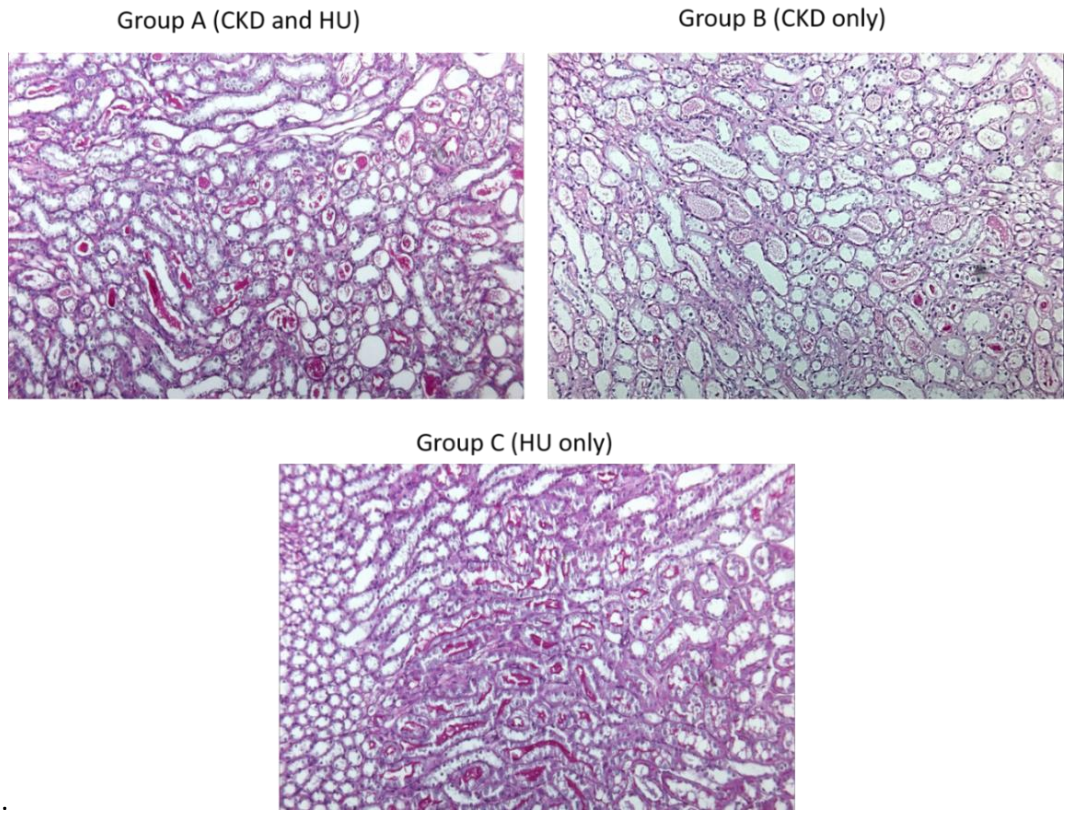

b.

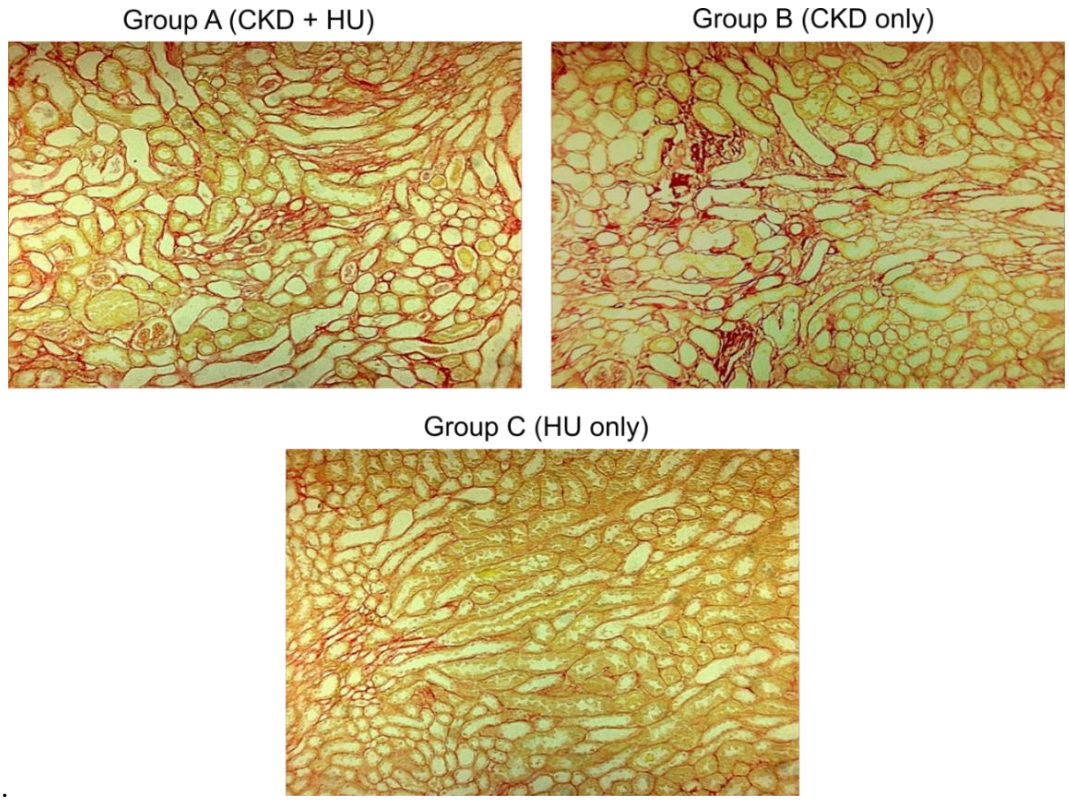

Figure 30. Asymptomatic hyperuricemia does not drive aristolochic acid I-induced chronic kidney disease nor uric acid tophi formation.

Kidneys were fixed in formalin and ethanol and later embedded in paraffin. The paraffin blocks were cut and stained for PAS (a.) and Picro-sirius red (b.). Representative pictures of each group were taken at 100x magnification.

5 Discussion

5.1 Overview

The relationship between UA and kidney function remains complex and is yet to be fully understood. The decline of kidney excretory function in CKD causes hyperuricemia [118] because UA is primarily excreted via the kidney. This raised the question whether hyperuricemia causes or accelerates CKD in a vicious cycle? If so, by what mechanism?

It has been shown that acute hyperuricemia causes AKI as seen in patients with tumor lysis syndrome or crush syndrome [118, 181]. This is due to the supersaturation of UA, which leads to the precipitation of intratubular UA crystals causing tubular occlusion and acute tubular injury. However, the same has not been shown for chronic mild to moderate hyperuricemia, which is the most prevalent type of hyperuricemia [182]. If asymptomatic hyperuricemia worsens kidney function, one would recommend urate-lowering therapy. However, the current medical guidelines do not recommend treatment of asymptomatic hyperuricemia for patients with or without CKD [183] due the lack of large randomized controlled trails.

Many authors, however, do imply a pathological role of hyperuricemia in CKD [121, 181, 184], citing various potential mechanisms. One such mechanism is UA crystal granuloma formation. As described in section 1.5.2, medullary UA crystal granulomas can occasionally be found in patients with advanced CKD and/or chronic gouty arthritis. For many years it was assumed that medullary UA crystal granulomas were a manifestation of chronic gout causing severe kidney function impairment [148, 149] or a result of intratubular UA accumulation similar to acute UA nephropathy [152]. Later, several authors raised doubt about tophaceous nephropathy as a clinical entity and argued that current data could not prove that medullary UA crystal granulomas cause or contribute to CKD progression [147, 153]. This resulted in the stagnation of the role of UA crystal granulomas [169]. However, many authors still list chronic UA nephropathy amongst causes for CKD [169]. In the present work, the relationship between asymptomatic hyperuricemia and UA crystal granuloma formation on CKD progression was examined.

The objectives of this study were as follow:

1. To characterize the histological abnormalities of diagnostic kidney biopsies with medullary UA crystal granulomas in a retrospective case-control study.
2. To investigate whether hyperuricemia with UA crystal granuloma formation contributes to CKD progression in a novel mouse model of chronic UA nephropathy.

3. To test whether asymptomatic hyperuricemia exacerbates preexisting CKD in mice.

5.1 Medullary UA crystal granulomas associate with histological signs of chronic kidney disease

The objective of this retrospective case-control study was to determine the prevalence of UA crystal granulomas in diagnostic kidney biopsies and to investigate whether medullary granulomas associate with significant tissue atrophy and scaring. In this study, medullary UA crystal granulomas can be found in 1 out of 1,000 consecutive kidney biopsies (0.1%) and associate with foreign body granuloma formation and kidney atrophy and scarring.

Hyperuricemia, gouty arthritis and urolithiasis have been shown to be associated with CKD [121, 150, 185-187], and prior to UA lowering therapy the development of end-stage kidney disease was common in patients with gouty arthritis [188, 189]. In the mid-twentieth century, several attempts were made to specify the prevalence of kidney gouty tophi in kidney biopsies that were performed on living patients with impaired kidney function for diagnostic purposes or at autopsies, a body examination to determine the cause of death. For example, Sokoloff *et al*. reported 64 patients with gouty arthritis out of 80 cases of which five had UA nephropathy (6.25%) [190], and Murray *et al.* reported that 11 out of 101 patients with interstitial nephritis had hyperuricemia as the primary cause of their kidney failure, presumably from chronic UA nephropathy (with kidney gouty tophi) [191]. In a larger study, Nickeleit *et al.* addressed the previously unknown prevalence of UA crystal granulomas in autopsies and found 37 cases with kidney UA deposits in a total number of 11,408 autopsies (classified as chronic UA nephropathy; 0.3%, other kidney comorbidities were not documented), and only three patients presented with chronic UA nephropathy from a selected group of 199 patients with end-stage kidney disease (1.5%) [153]. These authors concluded that in gouty arthritis patients, severe kidney damage with pronounced kidney dysfunction is almost invariably caused by other pathologies related to arterial hypertension, diabetes mellitus, urolithiasis or pyelonephritis [153]. Furthermore, in two consecutive studies the prevalence of medullary UA tophi was reported as 8-27% on autopsies from patients with preexisting CKD [151, 192]. The results of this large study with 81,200 total diagnostic kidney biopsies found medullary tophi at a frequency of 1 in 1,000 (0.1%) of all cases. While another retrospective study with only kidney biopsy reports from patients with predominant medullary tissue (796 of 7,409 total biopsies, 10.7%) found medullary UA crystal granulomas in 36 patients out of 572 CKD patients (6.11%) [152].

To verify the concept that hyperuricemia-related medullary UA crystal granulomas would associate with histopathological signs of CKD progression and assuming that hyperuricemia and UA-related conditions are a prerequisite for UA crystal granulomas, while taking into consideration the fact that these conditions themselves are associated with kidney dysfunction [122, 193], biopsy reports of

patients with medullary UA crystal granulomas were compared to biopsy reports of patients with hyperuricemia, and/or gout or UA urolithiasis but without medullary UA crystal granulomas. Therefore, eliminating the most prominent confounders for statistical comparison. In contrast to previous studies [151, 153, 192], the data now show that the observed histopathological differences cannot solely be explained by the kidney damage associated with pre-existing hyperuricemia, gouty arthritis or UA urolithiasis *per se*. The main pathological diagnoses were diverse, suggesting that UA crystal granulomas can occur in any type of CKD. Additionally, biopsies with medullary UA crystal granulomas had significantly more severe interstitial fibrosis, global glomerulosclerosis, foot process effacement, proteinuria, and arteriosclerosis.

Three underlying mechanisms could be responsible for the observed association of medullary UA crystal granulomas and worsening interstitial fibrosis (Figure 31). One possible reason could be preexisting CKD with long-lasting hyperuricemia or gouty arthritis, which contributes to UA crystal deposition due to urine acidification, UA precipitation and concentrated UA in the urine triggering tubular obstruction and activation of the NLRP3 inflammasome assembly to secrete interleukin (IL)-1β [111, 194]. This in turn recruits more inflammatory leukocytes including macrophages that amplify a foreign body UA crystal granuloma reaction and interstitial fibrosis with tubular atrophy [195]. As a result of collecting duct obstruction and subsequent nephron loss the remaining undamaged nephrons must undergo hyperperfusion, which increases the risk for CKD progression. Second, it is possible that larger UA crystal masses induce a particular reparative process known as extratubulation via an active self-protecting mechanism similar to that observed for adenine crystal-induced nephropathy [196]. In this process, tubular cells and macrophages overgrow and surround crystals in the interstitium, restoring the tubular luminal patency, followed by degradation of interstitial crystals by granulomatous inflammation. Third, it is possible that interstitial fibrosis caused by an underlying kidney disease serves as a prerequisite for the deposition of interstitial UA crystals and is therefore a requirement for the formation of medullary UA crystal granulomas. This could suggest that granulomas exacerbate an underlying kidney disease in a vicious cycle of necroinflammation leading to further nephron loss, depending type of inflammation elicited by the tophus (Figure 31, possibility 3). So far, all reports are insufficient to establish causality. Whether medullary UA crystal granulomas cause kidney atrophy and CKD or whether previously established fibrosis is required for the formation of UA granuloma or both can only be addressed by functional studies, e.g. in an animal model of chronic UA nephropathy, or in epidemiological studies.

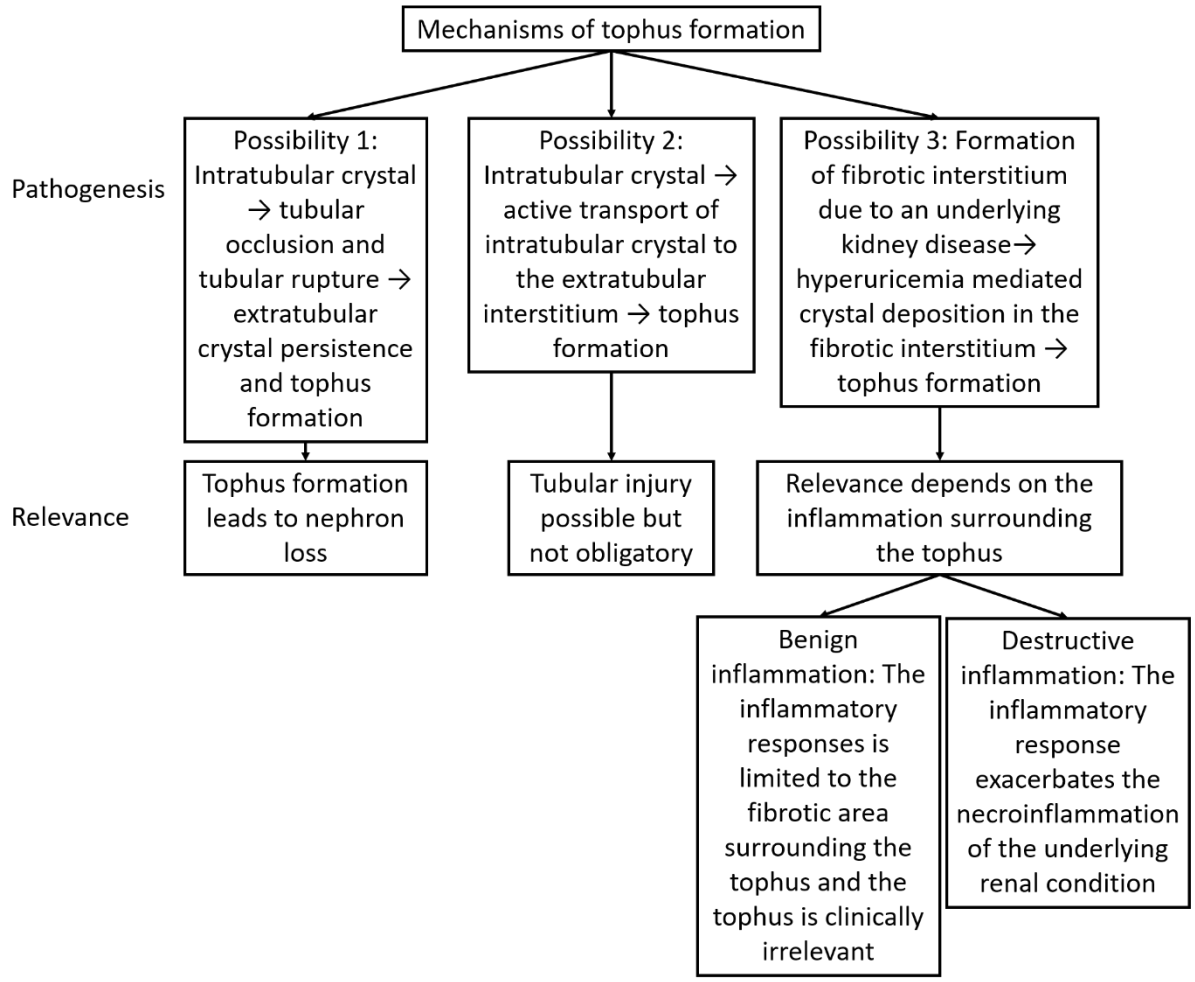

Figure 31. Possible mechanisms of medullary UA crystal granuloma formation.

5.2 Hyperuricemia with UA crystal granulomas drives CKD progression in mice

Thus far, no reliable mouse model of hyperuricemia with UA crystal granulomas has been described. Bluestone *et al.* reported crystal deposits in the kidneys of rats that were administered with oxonic acid and UA [161]. However, these animals did not develop hyperuricemia (serum UA < 5 mg/dl), the granuloma-like structures were inconsistent and only occurred in 66% of animals, and it is not clear whether the crystals are composed of UA. To overcome this issue, a novel animal model was established.

Hyperuricemic mice can develop UA crystal-induced nephropathy if elevated UA levels (serum UA > 7 mg/dl) persist for a long period of time [106, 107, 161]. This is due to a diminished capacity of the mouse kidney to handle large quantities of UA. The pathogenesis of this nephropathy is similar to the pathogenesis seen in humans with acute UA nephropathy due to tumor lysis or crush syndrome, where UA precipitates in the tubules and causes tubular occlusion and subsequent AKI. Consistent with the data in this thesis, Preitner *et al.* showed that in AlbCreERT2;*Glut9*$^{lox/lox}$ mice, long-term

supplementation of ACD but short-term administration of the UA precursor inosine results in acute UA nephropathy in these mice without UA crystal granuloma formation [168]. An ACD is needed for the precipitation of UA crystals and the induction of crystalline nephropathy by lowering the urine pH [168]. While under chronic supplementation of ACD with inosine, Alb-creERT2;*Glut9*$^{lox/lox}$ mice develop hyperuricemia with serum UA levels in a clinical relevant range (12-20 mg/dL) as well as crystalline UA nephropathy with a decline in GFR (of approx. 80%). Crystalline UA nephropathy occurred as a consequence of intratubular crystallization of UA due to an acidic urinary pH, which causes tubular occlusion, tubular injury and inflammation (section 4.2). This inflammatory response was associated with the infiltration of immune cells including macrophages. In addition, Alb-creERT2;*Glut9*$^{lox/lox}$ mice with hyperuricemia and crystalluria had profound interstitial fibrosis and numerous UA crystal granulomas were also observed, a process that may contributes to CKD progression. In contrast, mice with asymptomatic hyperuricemia remained healthy.

The fact that no UA crystal granulomas were found in mice with acute UA nephropathy but were present in mice with chronic UA nephropathy suggests that interstitial fibrosis is a prerequisite for tophi formation. Therefore, out of the three possible pathomechanisms of granuloma formation postulated in Figure 31, a combination of possibility one and three seems to be likely and would explain the data from the animal model because UA crystal granuloma formation requires preexisting interstitial fibrosis. Further support of this concept comes from the analysis of kidney biopsies. The association between tophi and glomerular and interstitial fibrosis on kidney biopsies is most likely caused by 1) vascular diseases as indicated by an increased arteriosclerosis score, or 2) advanced proteinuria-related diseases as shown by increased proteinuria and foot process effacement. Further support come from kidney biopsies of patients with AKI that showed significantly less UA crystal granulomas, indicating that UA crystal granulomas may primarily form in chronic kidney diseases. No biopsy report that was analyzed mentioned chronic UA crystal nephropathy as primary disease entity, suggesting that the kidney damage was always associated with another underlying primary kidney disease. Previous studies on this topic have shown similar results. For example, Nickeleit *et al.* concluded from an autopsy study with UA crystal granulomas that the “deterioration of kidney function can be better explained by other well-known risk factors of kidney disease most of the time” [153]. Berger and Yu, in a longitudinal study of gout patients with a 12 year follow-up, concluded that a decline in kidney function can be attributed to the development of “aging, kidney vascular disease, renal calculi with pyelonephritis or independently occurring nephropathy” [197]. In a follow-up study published seven years later, they showed that (articular) UA tophi were more likely to occur in patients with decreased kidney function and with the exception of a few patients that suffered “fulminant gout”, uncomplicated gout did not lead to the development of CKD [198]. CKD that did develop was attributed to ischemic heart disease, primary preexistent kidney disease, or hypertension [198]. In line

with the clinical research, the *in vivo* mouse model in this study provides further evidence that preexisting fibrosis/CKD is required for UA crystal granuloma formation.

Other underlying diseases including acute UA nephropathy as seen in Alb-creERT2;*Glut9*$^{lox/lox}$ mice and arterionephrosclerosis or FSGS in humans as shown in Figure 13 might serve as primary causes of CKD-related fibrosis; therefore creating an environment for pH-dependent UA crystal precipitation, e.g. the intake of medications or dietary changes, followed by UA crystal-induced tubular injury and subsequent UA crystal granuloma formation, which in turn contributes to CKD progression. Patients with chronic gout can develop CKD in which the primary cause of kidney disease is often related to vascular complications [198]. In advanced CKD stages with persistent hyperuricemia, the possibility for the occurrences of kidney UA crystal granulomas increases, which would explain the strong correlation between UA crystal granulomas not only with kidney fibrosis but also with proteinuria, foot process effacement, and arteriosclerosis, which are all signs for advanced CKD.

The deposition of crystals can elicit a foreign body reaction leading to mononuclear inflammation and formation of giant cells, similar to that observed in infectious or primary inflammatory granulomatous diseases including tuberculosis [199], sarcoidosis [200], granulomatosis with polyangiitis [201] or Chron's disease [202]. If UA crystal granuloma formation augment the progression of CKD is immunological in nature, this would raise the question: Does the granulomatous inflammatory reaction surrounding the UA crystal mass exacerbate the cycle of necroinflammation, which is caused by the primary kidney disease that leads to fibrotic lesions in the first place? Further *in vivo* and *in vitro* studies are needed to resolve this question. UA tophi have been observed in joints, bones, ligaments, tendons, nerves, and the skin [203]. In joints, the presentation of tophi is associated with loss of articular function [204], known as advanced gout, which goes along with significant bone and cartilage destruction [90]. The UA tophus itself represents a complex inflammatory microenvironment with both pro-inflammatory and anti-inflammatory/pro-fibrotic responses [89]. For example, neutrophil extracellular traps (NETs) have been show to degrade inflammatory cytokines and chemokines within the tophus using serine proteases [112]. Inflammation-mediated tissue destruction has been described many other granulomatous diseases as mentioned above as well as for pulmonary foreign body granulomatous reactions that can cause epithelial damage and fibrosis [205]. Therefore, it is reasonable to acknowledge that a certain destructive potential does emanate from the granulomatous inflammation surrounding the UA crystal mass in the kidney, and that the presence of such UA crystal granulomas amplifies the kidney damage in pre-existing CKD. Further *in vivo* studies in animal models are required to investigate this hypothesis.

5.3 Asymptomatic hyperuricemia does not contribute to CKD progression

There is controversial debate about the role of asymptomatic hyperuricemia in prosperity diseases such as CVD, CKD, and hypertension. As discussed in section 1.4.2, the current dogma implies that soluble UA and hyperuricemia have both anti- and pro-oxidant properties in various diseases. In CKD, Johnson *et al.* published a review pointing towards a pathological role for asymptomatic hyperuricemia without crystalluria in the development of CKD [121] by causing endothelial dysfunction, RAAS activation, and vascular smooth muscle proliferation leading to arteriosclerosis, glomerular disease, metabolic syndrome, and CKD progression. The argumentation was primarily based on a report by Kahn *et al.* showing that oxonic acid-induced hyperuricemia in rats (serum UA 3.2 mg/dL) that had undergone 5/6 nephrectomy developed CKD [206], which resulted in kidney injury as a consequence of oxidative stress, hypertension and RAAS activation [121, 206]. Of note, although urate-lowering therapy with allopurinol was effective in improving kidney function [206], these authors did not provide evidence for the presence of UA crystals in the kidney or the urine. Therefore, it is unclear whether the kidney injury was due to asymptomatic hyperuricemia or hyperuricemia with crystalluria. Many other in vivo animal models investigating the effect of hyperuricemia have also been described, models that are either based on diet-, surgical- or chemical-induced mouse model of hyperuricemia including intraperitoneal injection of high concentrations of UA [207, 208], oral administration of potassium oxonate [209-211], unilateral ureter obstruction-induced nephropathy [212] or diabetic nephropathy [213], or on genetic modification of urate transporter [214]. All these studies reported that hyperuricemia causes kidney injury despite only very low serum UA levels (2-5 mg/dL), which would not even be considered clinically as hyperuricemia. Using a novel mouse model of asymptomatic hyperuricemia (serum UA 12-20 mg/dL) without crystalluria, the data within this thesis demonstrate for the first time that asymptomatic hyperuricemia does not cause CKD nor contributes to AAI-induced CKD progression. Further experimental evidence comes from a study by Preitner *et al.* reporting no sign of hypertension in mild hyperuricemic mice after 6 months [106]. In addition, a recent in vivo study also showed that asymptomatic hyperuricemia acts as suppressor of innate immunity with the ability to inhibit monocyte functions during acute gouty arthritis [215], which indicates a rather immunomodulatory role for asymptomatic hyperuricemia.

In a recent review, Sato *et al*. performed an analysis of single- and multi-center randomized controlled trials (RCTs) on the topic of urate-lowering therapy in hyperuricemic patients with CKD [184]. The authors classified RCTs into “interpretable” and “non-interpretable” RCTs based on changes in GFR. The authors concluded that urate-lowering therapy is beneficial for a better outcome of kidney function and strongly recommended the use of urate-lowering therapy in patients with CKD and asymptomatic hyperuricemia. Unfortunately, the authors failed to correct for trial length in selecting studies as “non-interpretable” or “interpretable”, and therefore produced a selection bias, which was

recently corrected in a response meta-analysis [216]. This response letter pointed out other methodical flaws not only in the meta-analysis by Sato *et al.* but also in the underlying clinical trials and showed that the evidence from high powered, multi-center clinical trials has thus far refuted a beneficial role of urate-lowering therapy for hyperuricemic patients with CKD [216]. Furthermore, two large multi-center RCTs recently published in the New England Journal of Medicine consistently reported no effect of urate-lowering therapy on GFR in patients with CKD and asymptomatic hyperuricemia [217] and no effect of urate-lowering therapy in patients with mild to moderate diabetic nephropathy secondary to type I diabetes [218]. Taken together, the in vivo data gathered in this project disprove any (non-crystal induced) effects of asymptomatic hyperuricemia on CDK progression, which in line with the clinical evidence. Therefore, asymptomatic hyperuricemia does not cause CKD nor contributes to the progression of CKD unless UA crystals precipitate in the kidney leading to UA crystal nephropathy.

5.4 Limitations of this study

One limitation of this study as well as by others is a potential underestimation of the true prevalence of medullary UA crystal granulomas on diagnostic kidney biopsies compared to autopsy studies because only patients with suspected kidney disease are subjected to a kidney biopsy and because of the sampling error in diagnostic biopsies. In general, not all diagnostic biopsies contain adequate sampling of medulla, and due to the focal nature of UA tophi, even predominantly medullary biopsies may occasionally miss the tophi. It is also important to note that although rare, medullary tophi have also been observed in diagnostic biopsies of patients without CKD (0.01%) [152] or a history of gout [151, 192]. One reason might be the handling of UA in kidney proximal tubules in patients with hereditary UA overproduction, as in asymptomatic hyperuricemia [185, 219]. Therefore, this retrospective case-control study does not prove a causal relation between UA crystal granulomas and CKD progression.

The findings of this work are based on *in vivo* mouse models and the analysis of human kidney biopsy reports. Although, the animal model of hyperuricemia with or without UA crystal granuloma formation used herein is more closely related to the human disease setting and can be used as a translational model to investigate pathomechanisms, there are differences in the human and animal physiology because human diseases occur *de novo*, whereas animal disease models are produced artificially. In addition, due to the presence of functional uricase in lower mammals, rodents, especially rodent kidneys, have not evolved to deal high UA levels likes humans. This becomes evident when examining the Michaelis constant (Km) of kidney UA transporters in mice in comparison to humans as described in section 1.6. Human URAT1, for example with a Km of 370 µM has a higher affinity for UA than its murine ortholog, called mouse renal-specific transporter (RST) with a Km for UA of 1200 µM [155, 156].

Further evidence suggests that hyperuricemic mice or rats (serum UA level 2-5 mg/dL) develop kidney injury probably due to diet-induced acidification of the urine or genetic manipulation, which causes UA crystallization, similar to human acute gouty nephropathy [106, 107, 161]. Therefore, it is possible that mice are much more susceptible to crystalline nephropathy than humans because asymptomatic hyperuricemia does not lead to acute UA crystalline nephropathy in humans. In this study, care was taken that the conclusions drawn are correct despite this difference in UA handling between mice and humans and that the conclusions are therefore applicable to humans. However, other, perhaps yet unknown, mechanistic differences between human and rodent UA physiology and incorrect previous assumptions may have led to the drawing of incorrect conclusion.

Currently, there is no specific staining available to identify UA crystal granulomas in this mouse model. Here, we identified UA crystal granulomas on PAS-stained kidney sections and quantified morphological abnormalities. UA crystals were also found in the urine of mice to confirm crystalluria. However, it is possible that some were incorrectly identified on kidney sections because during the fixation process, UA crystals will be dissolved and leave only empty clefts behind.

5.5 Conclusions and future perspectives

The research presented within this thesis highlights the effects of asymptomatic hyperuricemia and hyperuricemia with crystalluria in CKD, in particular the role of UA crystal granulomas on the progression of chronic UA crystal nephropathy.

The precipitation of intraluminal UA crystals by feeding hyperuricemic Alb-creERT2;*Glut9*$^{lox/lox}$ mice an ACD with inosine triggers severe UA crystal-induced tubular injury and inflammation associated with the infiltration of immune cells such as macrophages, dendritic cells, neutrophils, monocytes and T cells. These inflammatory processes further lead to profound interstitial fibrosis and subsequent UA crystal granuloma formation. UA crystal granulomas form in the presence of preexisting CKD in a hyperuricemic environment and contribute to the progression of chronic UA crystal nephropathy. A proposed model is illustrated in Figure 32. Evidence for this finding comes from the retrospective case-control study showing that the presence of medullary UA tophi in humans (prevalence of 0.1%) is associated with severe interstitial and glomerular fibrosis as well as arteriosclerosis and foot process effacement. Screening for intrarenal or postrenal UA crystal deposits could be a useful diagnostic tool in clinical practice, as demonstrated within this study, as to whether urate-lowering therapy e.g. with allopurinol or uricostatic drugs may be considered in hyperuricemic CKD patients.

On the other hand, asymptomatic hyperuricemia without crystalluria does not cause tubular injury, inflammation and interstitial fibrosis and does not worsen signs of CKD compared to normouricemic mice with AAI-induced CKD. Recent multi-center RCTs confirm that urate-lowering therapy has no

beneficial effect on CKD progression [217, 218]. Whether a causal relationship between asymptomatic hyperuricemia and other diseases including metabolic syndrome and cardiovascular disease exists needs to be clarified in future studies.

UA crystals induce kidney injury, inflammation and interstitial fibrosis, which ultimately leads to UA crystal granuloma formation and CKD progression. Hyperuricemic patients with incidentally found granulomas on kidney biopsy may profit from xanthine oxidase inhibition, which reduces crystal growth and thus reduces the inflammatory stimulus. Before such treatment recommendations are given, more studies, including human studies, are of course required. In addition, macrophages are known to contribute to the formation of granulomas, e.g. in lung tuberculosis and sarcoidosis [199, 200]. The exact immune phenotype of kidney UA crystal granulomas in the fibrotic interstitium of humans and mice is subject of further investigation. The potential of UA crystal granulomas to amplify kidney damage needs to be further investigated to make adequate treatment recommendations for patients because patients with CKD profit from every nephron that can be saved. The investigational disinterest of recent years in chronic UA crystal nephropathy is unreasonable and much remains to be learned about UA tophi in the kidney and elsewhere in the body. This study has shed light on the pathogenesis of UA tophi, created a useful tool for their investigation, and will hopefully reignite interest in this forgotten disease.

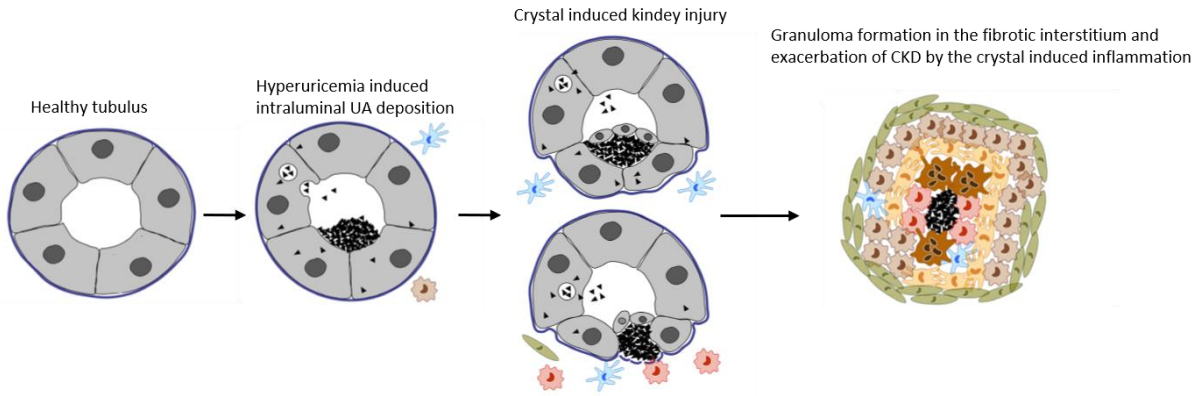

Figure 32. The pathogenesis of UA crystal-induced nephropathy.
Hyperuricemia predisposes to the intraluminal deposition of UA crystals. These intratubular crystals induce kidney injury, leading to nephron loss and ultimately fibrosis. Within the fibrotic interstitium and after CKD has been established UA crystal deposition leads to the formation of UA granulomas, also known as UA tophi, likely further driving CKD and the progression of kidney fibrosis via inflammatory mechanisms. Edited after [220].

6 List of Figures and Tables

6.1 Figures

6.2 Tables

7 References

1. Stevens, P.E., A. Levin, and M. Kidney Disease: Improving Global Outcomes Chronic Kidney Disease Guideline Development Work Group, *Evaluation and management of chronic kidney disease: synopsis of the kidney disease: improving global outcomes 2012 clinical practice guideline.* Ann Intern Med, 2013. **158**(11): p. 825-30.
2. Bertram, J.F., et al., *Human nephron number: implications for health and disease.* Pediatr Nephrol, 2011. **26**(9): p. 1529-33.
3. Denic, A., et al., *Single-Nephron Glomerular Filtration Rate in Healthy Adults.* N Engl J Med, 2017. **376**(24): p. 2349-2357.
4. Romagnani, P., et al., *Chronic kidney disease.* Nat Rev Dis Primers, 2017. **3**: p. 17088.
5. Levey, A.S., et al., *The definition, classification, and prognosis of chronic kidney disease: a KDIGO Controversies Conference report.* Kidney Int, 2011. **80**(1): p. 17-28.
6. Anders, H.-J. and P. Romagnani, *SGLT2 inhibition requires reconsideration of fundamental dogmas in chronic kidney disease, "diabetic nephropathy", IgA nephropathy, and podocytopathies with FSGS lesions*. 2020: NDT Nephrology Dialysis Transplantation.
7. Nevis, I.F., et al., *Pregnancy outcomes in women with chronic kidney disease: a systematic review.* Clin J Am Soc Nephrol, 2011. **6**(11): p. 2587-98.
8. Stenvinkel, P., C. Zoccali, and T.A. Ikizler, *Obesity in CKD--what should nephrologists know?* J Am Soc Nephrol, 2013. **24**(11): p. 1727-36.
9. Hughson, M., et al., *Glomerular number and size in autopsy kidneys: the relationship to birth weight.* Kidney Int, 2003. **63**(6): p. 2113-22.
10. Anders, H.J., J.M. Davis, and K. Thurau, *Nephron Protection in Diabetic Kidney Disease.* N Engl J Med, 2016. **375**(21): p. 2096-2098.
11. Wanner, C., et al., *Empagliflozin and Progression of Kidney Disease in Type 2 Diabetes.* N Engl J Med, 2016. **375**(4): p. 323-34.
12. Heerspink, H.J.L., et al., *Dapagliflozin in Patients with Chronic Kidney Disease.* N Engl J Med, 2020.
13. Ruggenenti, P., P. Cravedi, and G. Remuzzi, *Mechanisms and treatment of CKD.* J Am Soc Nephrol, 2012. **23**(12): p. 1917-28.
14. Schievink, B., et al., *Early renin-angiotensin system intervention is more beneficial than late intervention in delaying end-stage renal disease in patients with type 2 diabetes.* Diabetes Obes Metab, 2016. **18**(1): p. 64-71.
15. Gross, O., et al., *Early angiotensin-converting enzyme inhibition in Alport syndrome delays renal failure and improves life expectancy.* Kidney Int, 2012. **81**(5): p. 494-501.
16. Ruggenenti, P., et al., *Role of remission clinics in the longitudinal treatment of CKD.* J Am Soc Nephrol, 2008. **19**(6): p. 1213-24.
17. Garcia, G.G., P. Harden, and J. Chapman, *The global role of kidney transplantation.* Curr Opin Nephrol Hypertens, 2012. **21**(3): p. 229-34.
18. Bruck, K., et al., *CKD Prevalence Varies across the European General Population.* J Am Soc Nephrol, 2016. **27**(7): p. 2135-47.
19. Ricardo, A.C., et al., *Prevalence and Correlates of CKD in Hispanics/Latinos in the United States.* Clin J Am Soc Nephrol, 2015. **10**(10): p. 1757-66.
20. Jha, V., et al., *Chronic kidney disease: global dimension and perspectives.* Lancet, 2013. **382**(9888): p. 260-72.
21. Lozano, R., et al., *Global and regional mortality from 235 causes of death for 20 age groups in 1990 and 2010: a systematic analysis for the Global Burden of Disease Study 2010.* Lancet, 2012. **380**(9859): p. 2095-128.

22. Deutschland, S.B. *Krankheitskosten in Mio. € für Deutschland. Gliederungsmerkmale: Jahre, Geschlecht, ICD10, Einrichtung*. 2017 May 22, 2017; Available from: http://www.gbe-bund.de/stichworte/Niereninsuffizienz.html.
23. Anandagoda, N. and G.M. Lord, *Preventing aristolochic acid nephropathy.* Clin J Am Soc Nephrol, 2015. **10**(2): p. 167-8.
24. Vanherweghem, J.L., et al., *Rapidly progressive interstitial renal fibrosis in young women: association with slimming regimen including Chinese herbs.* Lancet, 1993. **341**(8842): p. 387-91.
25. Lord, G.M., et al., *Urothelial malignant disease and Chinese herbal nephropathy.* Lancet, 2001. **358**(9292): p. 1515-6.
26. Humans, I.W.G.o.t.E.o.C.R.t., *Some traditional herbal medicines, some mycotoxins, naphthalene and styrene.* IARC Monogr Eval Carcinog Risks Hum, 2002. **82**: p. 1-556.
27. Ivic, M., *[Etiology of endemic nephropathy].* Lijec Vjesn, 1969. **91**(12): p. 1273-81.
28. Gokmen, M.R., et al., *The epidemiology, diagnosis, and management of aristolochic acid nephropathy: a narrative review.* Ann Intern Med, 2013. **158**(6): p. 469-77.
29. Debelle, F.D., J.L. Vanherweghem, and J.L. Nortier, *Aristolochic acid nephropathy: a worldwide problem.* Kidney Int, 2008. **74**(2): p. 158-69.
30. Cosyns, J.P., *Aristolochic acid and 'Chinese herbs nephropathy': a review of the evidence to date.* Drug Saf, 2003. **26**(1): p. 33-48.
31. Zhou, L., et al., *Activation of p53 promotes renal injury in acute aristolochic acid nephropathy.* J Am Soc Nephrol, 2010. **21**(1): p. 31-41.
32. Nortier, J.L., et al., *Invasive urothelial carcinoma after exposure to Chinese herbal medicine containing aristolochic acid may occur without severe renal failure.* Nephrol Dial Transplant, 2003. **18**(2): p. 426-8.
33. Vanherweghem, J.L., et al., *Effects of steroids on the progression of renal failure in chronic interstitial renal fibrosis: a pilot study in Chinese herbs nephropathy.* Am J Kidney Dis, 1996. **27**(2): p. 209-15.
34. Martinez, M.C., et al., *Steroid therapy in chronic interstitial renal fibrosis: the case of Chinese-herb nephropathy.* Nephrol Dial Transplant, 2002. **17**(11): p. 2033-4.
35. Honarpisheh, M., et al., *Aristolochic acid I determine the phenotype and activation of macrophages in acute and chronic kidney disease.* Sci Rep, 2018. **8**(1): p. 12169.
36. Bobulescu, I.A. and O.W. Moe, *Renal transport of uric acid: evolving concepts and uncertainties.* Adv Chronic Kidney Dis, 2012. **19**(6): p. 358-71.
37. Cammalleri, L. and M. Malaguarnera, *Rasburicase represents a new tool for hyperuricemia in tumor lysis syndrome and in gout.* Int J Med Sci, 2007. **4**(2): p. 83-93.
38. Wilcox, W.D., *Abnormal serum uric acid levels in children.* J Pediatr, 1996. **128**(6): p. 731-41.
39. Nguyen, K.V. and W.L. Nyhan, *Mutation in the Human HPRT1 Gene and the Lesch-Nyhan Syndrome.* Nucleosides Nucleotides Nucleic Acids, 2016. **35**(8): p. 426-33.
40. Runolfsdottir, H.L., et al., *Kidney Disease in Adenine Phosphoribosyltransferase Deficiency.* Am J Kidney Dis, 2016. **67**(3): p. 431-8.
41. Ishikawa, T., W. Aw, and K. Kaneko, *Metabolic Interactions of Purine Derivatives with Human ABC Transporter ABCG2: Genetic Testing to Assess Gout Risk.* Pharmaceuticals (Basel), 2013. **6**(11): p. 1347-60.
42. Mandal, A.K. and D.B. Mount, *The molecular physiology of uric acid homeostasis.* Annu Rev Physiol, 2015. **77**: p. 323-45.
43. Andrade Sierra, J. and M.M. Flores Fonseca, *Renal Handling of Uric Acid.* Contrib Nephrol, 2018. **192**: p. 1-7.
44. Passwell, J.H., et al., *Fractional excretion of uric acid in infancy and childhood. Index of tubular maturation.* Arch Dis Child, 1974. **49**(11): p. 878-82.
45. Stapleton, F.B., et al., *Uric acid excretion in normal children.* J Pediatr, 1978. **92**(6): p. 911-4.
46. Stiburkova, B. and A.J. Bleyer, *Changes in serum urate and urate excretion with age.* Adv Chronic Kidney Dis, 2012. **19**(6): p. 372-6.

47. Gutman, A.B., T.F. Yu, and L. Berger, *Tubular secretion of urate in man.* J Clin Invest, 1959. **38**: p. 1778-81.
48. Gutman, A.B. and T.F. Yu, *A three-component system for regulation of renal excretion of uric acid in man.* Trans Assoc Am Physicians, 1961. **74**: p. 353-65.
49. Sirota, J.H., T.F. Yu, and A.B. Gutman, *Effect of benemid (p-[di-n-propylsulfamyl]-benzoic acid) on urate clearance and other discrete renal functions in gouty subjects.* J Clin Invest, 1952. **31**(7): p. 692-701.
50. Burns, J.J., et al., *A potent new uricosuric agent, the sulfoxide metabolite of the phenylbutazone analogue, G-25671.* J Pharmacol Exp Ther, 1957. **119**(3): p. 418-26.
51. Yu, T.F. and A.B. Gutman, *Study of the paradoxical effects of salicylate in low, intermediate and high dosage on the renal mechanisms for excretion of urate in man.* J Clin Invest, 1959. **38**(8): p. 1298-315.
52. Yu, T.F., L. Berger, and A.B. Gutman, *Suppression of tubular secretion of urate by pyrazinamide in the dog.* Proc Soc Exp Biol Med, 1961. **107**: p. 905-8.
53. Diamond, H.S. and J.S. Paolino, *Evidence for a postsecretory reabsorptive site for uric acid in man.* J Clin Invest, 1973. **52**(6): p. 1491-9.
54. Fathallah-Shaykh, S.A. and M.T. Cramer, *Uric acid and the kidney.* Pediatr Nephrol, 2014. **29**(6): p. 999-1008.
55. So, A. and B. Thorens, *Uric acid transport and disease.* J Clin Invest, 2010. **120**(6): p. 1791-9.
56. Guggino, S.E. and P.S. Aronson, *Paradoxical effects of pyrazinoate and nicotinate on urate transport in dog renal microvillus membranes.* J Clin Invest, 1985. **76**(2): p. 543-7.
57. Enomoto, A., et al., *Molecular identification of a renal urate anion exchanger that regulates blood urate levels.* Nature, 2002. **417**(6887): p. 447-52.
58. Fischer, H. *Kidney Nephron*. [Image] 2013; This is an image of a kidney nephron and its structure.]. Available from: https://commons.wikimedia.org/wiki/File:Kidney_Nephron.png.
59. Kottgen, A., et al., *Genome-wide association analyses identify 18 new loci associated with serum urate concentrations.* Nat Genet, 2013. **45**(2): p. 145-54.
60. Tanaka, M., et al., *Two male siblings with hereditary renal hypouricemia and exercise-induced ARF.* Am J Kidney Dis, 2003. **42**(6): p. 1287-92.
61. Wakida, N., et al., *Mutations in human urate transporter 1 gene in presecretory reabsorption defect type of familial renal hypouricemia.* J Clin Endocrinol Metab, 2005. **90**(4): p. 2169-74.
62. Ichida, K., et al., *Age and origin of the G774A mutation in SLC22A12 causing renal hypouricemia in Japanese.* Clin Genet, 2008. **74**(3): p. 243-51.
63. Ichida, K., et al., *Clinical and molecular analysis of patients with renal hypouricemia in Japan-influence of URAT1 gene on urinary urate excretion.* J Am Soc Nephrol, 2004. **15**(1): p. 164-73.
64. Phay, J.E., H.B. Hussain, and J.F. Moley, *Cloning and expression analysis of a novel member of the facilitative glucose transporter family, SLC2A9 (GLUT9).* Genomics, 2000. **66**(2): p. 217-20.
65. Augustin, R., et al., *Identification and characterization of human glucose transporter-like protein-9 (GLUT9): alternative splicing alters trafficking.* J Biol Chem, 2004. **279**(16): p. 16229-36.
66. Li, S., et al., *The GLUT9 gene is associated with serum uric acid levels in Sardinia and Chianti cohorts.* PLoS Genet, 2007. **3**(11): p. e194.
67. Dehghan, A., et al., *Association of three genetic loci with uric acid concentration and risk of gout: a genome-wide association study.* Lancet, 2008. **372**(9654): p. 1953-61.
68. Doring, A., et al., *SLC2A9 influences uric acid concentrations with pronounced sex-specific effects.* Nat Genet, 2008. **40**(4): p. 430-6.
69. Wallace, C., et al., *Genome-wide association study identifies genes for biomarkers of cardiovascular disease: serum urate and dyslipidemia.* Am J Hum Genet, 2008. **82**(1): p. 139-49.
70. Witkowska, K., et al., *Human SLC2A9a and SLC2A9b isoforms mediate electrogenic transport of urate with different characteristics in the presence of hexoses.* Am J Physiol Renal Physiol, 2012. **303**(4): p. F527-39.

71. Dinour, D., et al., *Homozygous SLC2A9 mutations cause severe renal hypouricemia.* J Am Soc Nephrol, 2010. **21**(1): p. 64-72.
72. Dinour, D., et al., *Two novel homozygous SLC2A9 mutations cause renal hypouricemia type 2.* Nephrol Dial Transplant, 2012. **27**(3): p. 1035-41.
73. Stiburkova, B., K. Ichida, and I. Sebesta, *Novel homozygous insertion in SLC2A9 gene caused renal hypouricemia.* Mol Genet Metab, 2011. **102**(4): p. 430-5.
74. Mou, L.J., L.P. Jiang, and Y. Hu, *A novel homozygous GLUT9 mutation cause recurrent exercise-induced acute renal failure and posterior reversible encephalopathy syndrome.* J Nephrol, 2015. **28**(3): p. 387-92.
75. Anzai, N., et al., *Plasma urate level is directly regulated by a voltage-driven urate efflux transporter URATv1 (SLC2A9) in humans.* J Biol Chem, 2008. **283**(40): p. 26834-8.
76. Matsuo, H., et al., *Mutations in glucose transporter 9 gene SLC2A9 cause renal hypouricemia.* Am J Hum Genet, 2008. **83**(6): p. 744-51.
77. Kawamura, Y., et al., *Pathogenic GLUT9 mutations causing renal hypouricemia type 2 (RHUC2).* Nucleosides Nucleotides Nucleic Acids, 2011. **30**(12): p. 1105-11.
78. van der Harst, P., et al., *Replication of the five novel loci for uric acid concentrations and potential mediating mechanisms.* Hum Mol Genet, 2010. **19**(2): p. 387-95.
79. Yang, Q., et al., *Multiple genetic loci influence serum urate levels and their relationship with gout and cardiovascular disease risk factors.* Circ Cardiovasc Genet, 2010. **3**(6): p. 523-30.
80. Kolz, M., et al., *Meta-analysis of 28,141 individuals identifies common variants within five new loci that influence uric acid concentrations.* PLoS Genet, 2009. **5**(6): p. e1000504.
81. Phipps-Green, A.J., et al., *Twenty-eight loci that influence serum urate levels: analysis of association with gout.* Ann Rheum Dis, 2016. **75**(1): p. 124-30.
82. Sakiyama, M., et al., *A common variant of organic anion transporter 4 (OAT4/SLC22A11) gene is associated with renal underexcretion type gout.* Drug Metab Pharmacokinet, 2014. **29**(2): p. 208-10.
83. Bahn, A., et al., *Identification of a new urate and high affinity nicotinate transporter, hOAT10 (SLC22A13).* J Biol Chem, 2008. **283**(24): p. 16332-41.
84. El-Sheikh, A.A., et al., *Effect of hypouricaemic and hyperuricaemic drugs on the renal urate efflux transporter, multidrug resistance protein 4.* Br J Pharmacol, 2008. **155**(7): p. 1066-75.
85. Jutabha, P., et al., *Human sodium phosphate transporter 4 (hNPT4/SLC17A3) as a common renal secretory pathway for drugs and urate.* J Biol Chem, 2010. **285**(45): p. 35123-32.
86. Iharada, M., et al., *Type 1 sodium-dependent phosphate transporter (SLC17A1 Protein) is a Cl(-)-dependent urate exporter.* J Biol Chem, 2010. **285**(34): p. 26107-13.
87. Woodward, O.M., et al., *Identification of a urate transporter, ABCG2, with a common functional polymorphism causing gout.* Proc Natl Acad Sci U S A, 2009. **106**(25): p. 10338-42.
88. Enomoto, A. and H. Endou, *Roles of organic anion transporters (OATs) and a urate transporter (URAT1) in the pathophysiology of human disease.* Clin Exp Nephrol, 2005. **9**(3): p. 195-205.
89. Dalbeth, N., et al., *Cellular characterization of the gouty tophus: a quantitative analysis.* Arthritis Rheum, 2010. **62**(5): p. 1549-56.
90. Dalbeth, N., et al., *Mechanisms of bone erosion in gout: a quantitative analysis using plain radiography and computed tomography.* Ann Rheum Dis, 2009. **68**(8): p. 1290-5.
91. Kuo, C.F., et al., *Global epidemiology of gout: prevalence, incidence and risk factors.* Nat Rev Rheumatol, 2015. **11**(11): p. 649-62.
92. Zhu, Y., B.J. Pandya, and H.K. Choi, *Comorbidities of gout and hyperuricemia in the US general population: NHANES 2007-2008.* Am J Med, 2012. **125**(7): p. 679-687 e1.
93. Choi, H.K. and G. Curhan, *Independent impact of gout on mortality and risk for coronary heart disease.* Circulation, 2007. **116**(8): p. 894-900.
94. Mallamaci, F., et al., *A genetic marker of uric acid level, carotid atherosclerosis, and arterial stiffness: a family-based study.* Am J Kidney Dis, 2015. **65**(2): p. 294-302.
95. Kleber, M.E., et al., *Uric Acid and Cardiovascular Events: A Mendelian Randomization Study.* J Am Soc Nephrol, 2015. **26**(11): p. 2831-8.

96. Testa, A., et al., *Association of a polymorphism in a gene encoding a urate transporter with CKD progression.* Clin J Am Soc Nephrol, 2014. **9**(6): p. 1059-65.
97. Ames, B.N., et al., *Uric acid provides an antioxidant defense in humans against oxidant- and radical-caused aging and cancer: a hypothesis.* Proc Natl Acad Sci U S A, 1981. **78**(11): p. 6858-62.
98. Yu, Z.F., et al., *Uric acid protects neurons against excitotoxic and metabolic insults in cell culture, and against focal ischemic brain injury in vivo.* J Neurosci Res, 1998. **53**(5): p. 613-25.
99. Hooper, D.C., et al., *Uric acid, a natural scavenger of peroxynitrite, in experimental allergic encephalomyelitis and multiple sclerosis.* Proc Natl Acad Sci U S A, 1998. **95**(2): p. 675-80.
100. Sautin, Y.Y. and R.J. Johnson, *Uric acid: the oxidant-antioxidant paradox.* Nucleosides Nucleotides Nucleic Acids, 2008. **27**(6): p. 608-19.
101. Hayden, M.R. and S.C. Tyagi, *Uric acid: A new look at an old risk marker for cardiovascular disease, metabolic syndrome, and type 2 diabetes mellitus: The urate redox shuttle.* Nutr Metab (Lond), 2004. **1**(1): p. 10.
102. Glantzounis, G.K., et al., *Uric acid and oxidative stress.* Curr Pharm Des, 2005. **11**(32): p. 4145-51.
103. Santos, C.X., E.I. Anjos, and O. Augusto, *Uric acid oxidation by peroxynitrite: multiple reactions, free radical formation, and amplification of lipid oxidation.* Arch Biochem Biophys, 1999. **372**(2): p. 285-94.
104. Sanchez-Lozada, L.G., et al., *Uric acid-induced endothelial dysfunction is associated with mitochondrial alterations and decreased intracellular ATP concentrations.* Nephron Exp Nephrol, 2012. **121**(3-4): p. e71-8.
105. Savage, P.J., et al., *Influence of long-term, low-dose, diuretic-based, antihypertensive therapy on glucose, lipid, uric acid, and potassium levels in older men and women with isolated systolic hypertension: The Systolic Hypertension in the Elderly Program. SHEP Cooperative Research Group.* Arch Intern Med, 1998. **158**(7): p. 741-51.
106. Preitner, F., et al., *No development of hypertension in the hyperuricemic liver-Glut9 knockout mouse.* Kidney Int, 2015. **87**(5): p. 940-7.
107. Lu, J., et al., *Knockout of the urate oxidase gene provides a stable mouse model of hyperuricemia associated with metabolic disorders.* Kidney Int, 2018. **93**(1): p. 69-80.
108. Watanabe, S., et al., *Uric acid, hominoid evolution, and the pathogenesis of salt-sensitivity.* Hypertension, 2002. **40**(3): p. 355-60.
109. Johnson, R.J., et al., *Essential hypertension, progressive renal disease, and uric acid: a pathogenetic link?* J Am Soc Nephrol, 2005. **16**(7): p. 1909-19.
110. Feig, D.I., B. Soletsky, and R.J. Johnson, *Effect of allopurinol on blood pressure of adolescents with newly diagnosed essential hypertension: a randomized trial.* JAMA, 2008. **300**(8): p. 924-32.
111. Martinon, F., et al., *Gout-associated uric acid crystals activate the NALP3 inflammasome.* Nature, 2006. **440**(7081): p. 237-41.
112. Schauer, C., et al., *Aggregated neutrophil extracellular traps limit inflammation by degrading cytokines and chemokines.* Nat Med, 2014. **20**(5): p. 511-7.
113. Garrod, A.B., *The nature and treatment of gout and rheumatic gout*. 1859, London: Walton and Maberly. xvi, 601 p.
114. Garrod, A.B., *Observations on certain pathological conditions of the blood and urine, in gout, rheumatism, and Bright's disease.* Med Chir Trans, 1848. **31**: p. 83-97.
115. Rundres, R., *Effects of a xanthine oxidase inhibitor on thiopurine metabolism, hyperuricemia and gout.* Trans Ass Amer Phycns, 1963. **76**: p. 126-140.
116. Dalbeth, N., T.R. Merriman, and L.K. Stamp, *Gout.* Lancet, 2016. **388**(10055): p. 2039-2052.
117. Schumacher, H.R., Jr., et al., *Effects of febuxostat versus allopurinol and placebo in reducing serum urate in subjects with hyperuricemia and gout: a 28-week, phase III, randomized, double-blind, parallel-group trial.* Arthritis Rheum, 2008. **59**(11): p. 1540-8.
118. Suliman, M.E., et al., *J-shaped mortality relationship for uric acid in CKD.* Am J Kidney Dis, 2006. **48**(5): p. 761-71.

119. Madero, M., et al., *Uric acid and long-term outcomes in CKD.* Am J Kidney Dis, 2009. **53**(5): p. 796-803.
120. Sturm, G., et al., *Uric acid as a risk factor for progression of non-diabetic chronic kidney disease? The Mild to Moderate Kidney Disease (MMKD) Study.* Exp Gerontol, 2008. **43**(4): p. 347-52.
121. Johnson, R.J., et al., *Uric acid and chronic kidney disease: which is chasing which?* Nephrol Dial Transplant, 2013. **28**(9): p. 2221-8.
122. Obermayr, R.P., et al., *Elevated uric acid increases the risk for kidney disease.* J Am Soc Nephrol, 2008. **19**(12): p. 2407-13.
123. Weiner, D.E., et al., *The relationship between nontraditional risk factors and outcomes in individuals with stage 3 to 4 CKD.* Am J Kidney Dis, 2008. **51**(2): p. 212-23.
124. Yen, C.J., et al., *Hyperuricemia associated with rapid renal function decline in elderly Taiwanese subjects.* J Formos Med Assoc, 2009. **108**(12): p. 921-8.
125. Altemtam, N., J. Russell, and M. El Nahas, *A study of the natural history of diabetic kidney disease (DKD).* Nephrol Dial Transplant, 2012. **27**(5): p. 1847-54.
126. Shi, Y., et al., *Clinical outcome of hyperuricemia in IgA nephropathy: a retrospective cohort study and randomized controlled trial.* Kidney Blood Press Res, 2012. **35**(3): p. 153-60.
127. Lee, S.M., et al., *Low serum uric acid level is a risk factor for death in incident hemodialysis patients.* Am J Nephrol, 2009. **29**(2): p. 79-85.
128. Quinones Galvan, A., et al., *Effect of insulin on uric acid excretion in humans.* Am J Physiol, 1995. **268**(1 Pt 1): p. E1-5.
129. Messerli, F.H., et al., *Serum uric acid in essential hypertension: an indicator of renal vascular involvement.* Ann Intern Med, 1980. **93**(6): p. 817-21.
130. Choi, H.K., et al., *Purine-rich foods, dairy and protein intake, and the risk of gout in men.* N Engl J Med, 2004. **350**(11): p. 1093-103.
131. Sanchez-Lozada, L.G., et al., *Effects of febuxostat on metabolic and renal alterations in rats with fructose-induced metabolic syndrome.* Am J Physiol Renal Physiol, 2008. **294**(4): p. F710-8.
132. Nakagawa, T., et al., *A causal role for uric acid in fructose-induced metabolic syndrome.* Am J Physiol Renal Physiol, 2006. **290**(3): p. F625-31.
133. Lai, L.H., et al., *Renal dysfunction and hyperuricemia with low blood lead levels and ethnicity in community-based study.* Sci Total Environ, 2008. **401**(1-3): p. 39-43.
134. Lin, J.L., H.H. Ho, and C.C. Yu, *Chelation therapy for patients with elevated body lead burden and progressive renal insufficiency. A randomized, controlled trial.* Ann Intern Med, 1999. **130**(1): p. 7-13.
135. Roncal, C., et al., *Lead, at low levels, accelerates arteriolopathy and tubulointerstitial injury in chronic kidney disease.* Am J Physiol Renal Physiol, 2007. **293**(4): p. F1391-6.
136. Siu, Y.P., et al., *Use of allopurinol in slowing the progression of renal disease through its ability to lower serum uric acid level.* Am J Kidney Dis, 2006. **47**(1): p. 51-9.
137. Goicoechea, M., et al., *Effect of allopurinol in chronic kidney disease progression and cardiovascular risk.* Clin J Am Soc Nephrol, 2010. **5**(8): p. 1388-93.
138. Momeni, A., et al., *Effect of allopurinol in decreasing proteinuria in type 2 diabetic patients.* Iran J Kidney Dis, 2010. **4**(2): p. 128-32.
139. Wang, H., et al., *Effects of urate-lowering therapy in hyperuricemia on slowing the progression of renal function: a meta-analysis.* J Ren Nutr, 2013. **23**(5): p. 389-96.
140. Ito, S., et al., *Impact of serum uric acid on renal function and cardiovascular events in hypertensive patients treated with losartan.* Hypertens Res, 2012. **35**(8): p. 867-73.
141. Lusco, M.A., et al., *AJKD Atlas of Renal Pathology: Gouty Nephropathy.* Am J Kidney Dis, 2017. **69**(1): p. e5-e6.
142. Cairo, M.S. and M. Bishop, *Tumour lysis syndrome: new therapeutic strategies and classification.* Br J Haematol, 2004. **127**(1): p. 3-11.
143. Wilson, F.P. and J.S. Berns, *Onco-nephrology: tumor lysis syndrome.* Clin J Am Soc Nephrol, 2012. **7**(10): p. 1730-9.

144. Alakel, N., et al., *Prevention and treatment of tumor lysis syndrome, and the efficacy and role of rasburicase.* Onco Targets Ther, 2017. **10**: p. 597-605.
145. Goldman, S.C., et al., *A randomized comparison between rasburicase and allopurinol in children with lymphoma or leukemia at high risk for tumor lysis.* Blood, 2001. **97**(10): p. 2998-3003.
146. Chhana, A. and N. Dalbeth, *The gouty tophus: a review.* Curr Rheumatol Rep, 2015. **17**(3): p. 19.
147. Beck, L.H., *Requiem for gouty nephropathy.* Kidney Int, 1986. **30**(2): p. 280-7.
148. Modern, F.W. and L. Meister, *The kidney of gout, a clinical entity.* Med Clin North Am, 1952. **21**: p. 941-51.
149. Talbott, J.H. and K.L. Terplan, *The kidney in gout.* Medicine (Baltimore), 1960. **39**: p. 405-67.
150. Barlow, K.A. and L.J. Beilin, *Renal disease in primary gout.* Q J Med, 1968. **37**(145): p. 79-96.
151. Linnane, J.W., A.F. Burry, and B.T. Emmerson, *Urate deposits in the renal medulla. Prevalence and associations.* Nephron, 1981. **29**(5-6): p. 216-22.
152. Ayoub, I., et al., *Revisiting medullary tophi: a link between uric acid and progressive chronic kidney disease?* Clin Nephrol, 2016. **85**(2): p. 109-13.
153. Nickeleit, V. and M.J. Mihatsch, *Uric acid nephropathy and end-stage renal disease--review of a non-disease.* Nephrol Dial Transplant, 1997. **12**(9): p. 1832-8.
154. Bernd, Z., *Laborchemische Referenzbereiche für Wistarratten und C57BL/6-Mäuse*, in *Medizinische Fakultät*. 2005, Universität Düsseldorf.
155. Hosoyamada, M., et al., *Function and localization of urate transporter 1 in mouse kidney.* J Am Soc Nephrol, 2004. **15**(2): p. 261-8.
156. Mori, K., et al., *Kidney-specific expression of a novel mouse organic cation transporter-like protein.* FEBS Lett, 1997. **417**(3): p. 371-4.
157. Eraly, S.A., et al., *Multiple organic anion transporters contribute to net renal excretion of uric acid.* Physiol Genomics, 2008. **33**(2): p. 180-92.
158. Keembiyehetty, C., et al., *Mouse glucose transporter 9 splice variants are expressed in adult liver and kidney and are up-regulated in diabetes.* Mol Endocrinol, 2006. **20**(3): p. 686-97.
159. Williamson, D.J., M.L. Hooper, and D.W. Melton, *Mouse models of hypoxanthine phosphoribosyltransferase deficiency.* J Inherit Metab Dis, 1992. **15**(4): p. 665-73.
160. Jinnah, H.A., F.H. Gage, and T. Friedmann, *Animal models of Lesch-Nyhan syndrome.* Brain Res Bull, 1990. **25**(3): p. 467-75.
161. Bluestone, R., J. Waisman, and J.R. Klinenberg, *Chronic experimental hyperuricemic nephropathy.* Lab Invest, 1975. **33**(3): p. 273-9.
162. Zhang, Y., et al., *Effect and mechanism of dioscin from Dioscorea spongiosa on uric acid excretion in animal model of hyperuricemia.* J Ethnopharmacol, 2018. **214**: p. 29-36.
163. Martinez-Ramirez, M., et al., *Hyperuricemia is Associated with Increased Apo AI Fractional Catabolic Rates and Dysfunctional HDL in New Zealand Rabbits.* Lipids, 2017. **52**(12): p. 999-1006.
164. Kurra, V., et al., *Effects of oxonic acid-induced hyperuricemia on mesenteric artery tone and cardiac load in experimental renal insufficiency.* BMC Nephrol, 2015. **16**: p. 35.
165. Garcia-Arroyo, F.E., et al., *Probiotic supplements prevented oxonic acid-induced hyperuricemia and renal damage.* PLoS One, 2018. **13**(8): p. e0202901.
166. Wu, X., et al., *Hyperuricemia and urate nephropathy in urate oxidase-deficient mice.* Proc Natl Acad Sci U S A, 1994. **91**(2): p. 742-6.
167. Preitner, F., et al., *Glut9 is a major regulator of urate homeostasis and its genetic inactivation induces hyperuricosuria and urate nephropathy.* Proc Natl Acad Sci U S A, 2009. **106**(36): p. 15501-6.
168. Preitner, F., et al., *Urate-induced acute renal failure and chronic inflammation in liver-specific Glut9 knockout mice.* Am J Physiol Renal Physiol, 2013. **305**(5): p. F786-95.
169. Herold, G., *Innere Medizin eine vorlesungsorientierte Darstellung unter Berücksichtigung des Gegenstandskataloges für die ärztliche Prüfung mit ICD 10-Schlüssel im Text und Stichwortverzeichnis*. 2015. p. Bände.

170. Liapis, H., et al., *Banff Histopathological Consensus Criteria for Preimplantation Kidney Biopsies.* Am J Transplant, 2017. **17**(1): p. 140-150.
171. rodents, F.w.g.o.r.o.g.f.h.m.o., et al., *FELASA recommendations for the health monitoring of mouse, rat, hamster, guinea pig and rabbit colonies in breeding and experimental units.* Lab Anim, 2014. **48**(3): p. 178-192.
172. Kilkenny, C., et al., *Improving bioscience research reporting: the ARRIVE guidelines for reporting animal research.* PLoS Biol, 2010. **8**(6): p. e1000412.
173. Kelmenson, P. *Cre Lox Breeding For Beginners, PART 1*. The Jackson Laboratory [Blog post] 2011; Available from: https://www.jax.org/news-and-insights/jax-blog/2011/september/cre-lox-breeding.
174. Marschner, J., *Die Rolle von Pentraxin 3 bei entzündlichen Nierenerkrankungen*. 2019, LMU München.
175. Yu, W., R.M. Sandoval, and B.A. Molitoris, *Rapid determination of renal filtration function using an optical ratiometric imaging approach.* Am J Physiol Renal Physiol, 2007. **292**(6): p. F1873-80.
176. Liapis, H., et al., *Myoglobin casts in renal biopsies: immunohistochemistry and morphologic spectrum.* Hum Pathol, 2016. **54**: p. 25-30.
177. Steiger, S., et al., *Anti-Transforming Growth Factor beta IgG Elicits a Dual Effect on Calcium Oxalate Crystallization and Progressive Nephrocalcinosis-Related Chronic Kidney Disease.* Front Immunol, 2018. **9**: p. 619.
178. Deegens, J.K., et al., *Podocyte foot process effacement as a diagnostic tool in focal segmental glomerulosclerosis.* Kidney Int, 2008. **74**(12): p. 1568-76.
179. Marshall, C.B., *Rethinking glomerular basement membrane thickening in diabetic nephropathy: adaptive or pathogenic?* Am J Physiol Renal Physiol, 2016. **311**(5): p. F831-F843.
180. Sellmayr, M., et al., *Only Hyperuricemia with Crystalluria, but not Asymptomatic Hyperuricemia, Drives Progression of Chronic Kidney Disease.* J Am Soc Nephrol, 2020.
181. Giordano, C., et al., *Uric Acid as a Marker of Kidney Disease: Review of the Current Literature.* Dis Markers, 2015. **2015**: p. 382918.
182. Liu, R., et al., *Prevalence of Hyperuricemia and Gout in Mainland China from 2000 to 2014: A Systematic Review and Meta-Analysis.* Biomed Res Int, 2015. **2015**: p. 762820.
183. Kiltz, U., et al., *Langfassung zur S2e-Leitlinie Gichtarthritis (fachärztlich): Evidenzbasierte Leitlinie der Deutschen Gesellschaft für Rheumatologie (DGRh)(Leitlinie).* Zeitschrift für Rheumatologie, 2016. **75**(2): p. 11-60.
184. Sato, Y., et al., *The case for uric acid-lowering treatment in patients with hyperuricaemia and CKD.* Nat Rev Nephrol, 2019. **15**(12): p. 767-775.
185. Jalal, D.I., *Hyperuricemia, the kidneys, and the spectrum of associated diseases: a narrative review.* Curr Med Res Opin, 2016. **32**(11): p. 1863-1869.
186. Shang, W., et al., *History of kidney stones and risk of chronic kidney disease: a meta-analysis.* PeerJ, 2017. **5**: p. e2907.
187. Chou, Y.C., et al., *Elevated uric acid level as a significant predictor of chronic kidney disease: a cohort study with repeated measurements.* J Nephrol, 2015. **28**(4): p. 457-62.
188. Levin, N.W. and O.L. Abrahams, *Allopurinol in patients with impaired renal function.* Ann Rheum Dis, 1966. **25**(6 Suppl): p. 681-7.
189. Briney, W.G., et al., *The influence of allopurinol on renal function in gout.* Arthritis Rheum, 1975. **18**(6 Suppl): p. 877-81.
190. Sokoloff, L., *The pathology of gout.* Metabolism, 1957. **6**(3): p. 230-43.
191. Murray, T. and M. Goldberg, *Chronic interstitial nephritis: etiologic factors.* Ann Intern Med, 1975. **82**(4): p. 453-9.
192. Verger, D., et al., *[Gouty tophi in the renal medulla in chronic uremia. Study of 17 cases discovered from among 62 autopsies].* Nephron, 1967. **4**(6): p. 356-70.
193. Moe, O.W., *Posing the question again: does chronic uric acid nephropathy exist?* J Am Soc Nephrol, 2010. **21**(3): p. 395-7.

194. Desai, J., S. Steiger, and H.J. Anders, *Molecular Pathophysiology of Gout.* Trends Mol Med, 2017. **23**(8): p. 756-768.
195. Mulay, S.R. and H.J. Anders, *Crystal nephropathies: mechanisms of crystal-induced kidney injury.* Nat Rev Nephrol, 2017. **13**(4): p. 226-240.
196. Klinkhammer, B.M., et al., *Cellular and Molecular Mechanisms of Kidney Injury in 2,8-Dihydroxyadenine Nephropathy.* J Am Soc Nephrol, 2020. **31**(4): p. 799-816.
197. Berger, L. and T.F. Yu, *Renal function in gout. IV. An analysis of 524 gouty subjects including long-term follow-up studies.* Am J Med, 1975. **59**(5): p. 605-13.
198. Yu, T.F. and L. Berger, *Impaired renal function gout: its association with hypertensive vascular disease and intrinsic renal disease.* Am J Med, 1982. **72**(1): p. 95-100.
199. Qualls, J.E. and P.J. Murray, *Immunometabolism within the tuberculosis granuloma: amino acids, hypoxia, and cellular respiration.* Semin Immunopathol, 2016. **38**(2): p. 139-52.
200. Newman, L.S., C.S. Rose, and L.A. Maier, *Sarcoidosis.* N Engl J Med, 1997. **336**(17): p. 1224-34.
201. Thompson, L.D., *Wegener granulomatosis.* Ear Nose Throat J, 2013. **92**(1): p. 18-22.
202. Marshak, R.H., *Granulomatous disease of the intestinal tract (Crohn's disease).* Radiology, 1975. **114**(1): p. 3-22.
203. Forbess, L.J. and T.R. Fields, *The broad spectrum of urate crystal deposition: unusual presentations of gouty tophi.* Semin Arthritis Rheum, 2012. **42**(2): p. 146-54.
204. Dalbeth, N., et al., *Tophaceous joint disease strongly predicts hand function in patients with gout.* Rheumatology, 2007. **46**(12): p. 1804-1807.
205. Staloch, D.A. and J.S. Hedley, *Pulmonary Foreign-Body Granulomatosis.* N Engl J Med, 2017. **377**(13): p. 1273.
206. Kang, D.H., et al., *A role for uric acid in the progression of renal disease.* J Am Soc Nephrol, 2002. **13**(12): p. 2888-97.
207. Yang, Z., et al., *Uric acid increases fibronectin synthesis through upregulation of lysyl oxidase expression in rat renal tubular epithelial cells.* Am J Physiol Renal Physiol, 2010. **299**(2): p. F336-46.
208. Romi, M.M., et al., *Uric acid causes kidney injury through inducing fibroblast expansion, Endothelin-1 expression, and inflammation.* BMC Nephrol, 2017. **18**(1): p. 326.
209. Khosla, U.M., et al., *Hyperuricemia induces endothelial dysfunction.* Kidney Int, 2005. **67**(5): p. 1739-42.
210. Tung, Y.T., et al., *Antioxidative phytochemicals from Rhododendron oldhamii Maxim. leaf extracts reduce serum uric acid levels in potassium oxonate-induced hyperuricemic mice.* BMC Complement Altern Med, 2015. **15**: p. 423.
211. Shi, Y.W., et al., *Uricosuric and nephroprotective properties of Ramulus Mori ethanol extract in hyperuricemic mice.* J Ethnopharmacol, 2012. **143**(3): p. 896-904.
212. Braga, T.T., et al., *Soluble Uric Acid Activates the NLRP3 Inflammasome.* Sci Rep, 2017. **7**: p. 39884.
213. Kim, S.M., et al., *Hyperuricemia-induced NLRP3 activation of macrophages contributes to the progression of diabetic nephropathy.* Am J Physiol Renal Physiol, 2015. **308**(9): p. F993-F1003.
214. Lu, J., et al., *Mouse models for human hyperuricaemia: a critical review.* Nat Rev Rheumatol, 2019. **15**(7): p. 413-426.
215. Ma, Q., et al., *Soluble Uric Acid Is an Intrinsic Negative Regulator of Monocyte Activation in Monosodium Urate Crystal-Induced Tissue Inflammation.* J Immunol, 2020. **205**(3): p. 789-800.
216. Steiger, S., Q. Ma, and H.-J. Anders, *The case for evidence-based medicine for the association between hyperuricaemia and CKD.* Nature Reviews Nephrology, 2020.
217. Badve, S.V., et al., *Effects of Allopurinol on the Progression of Chronic Kidney Disease.* N Engl J Med, 2020. **382**(26): p. 2504-2513.
218. Doria, A., et al., *Serum Urate Lowering with Allopurinol and Kidney Function in Type 1 Diabetes.* N Engl J Med, 2020. **382**(26): p. 2493-2503.
219. Emmerson, B.T. and P.G. Row, *Editorial: An evaluation of the pathogenesis of gouty kidney.* Kidney Int, 1975. **8**(2): p. 65-71.

220. Mulay, S.R., et al., *A guide to crystal-related and nano- or microparticle-related tissue responses.* FEBS J, 2020. **287**(5): p. 818-832.

8 Acknowledgements

Many people have supported me during the time spent in the laboratory conducting experiments and later in the writing process of this thesis. Collectively, all have made this work possible.

First and foremost, I would like to thank my thesis supervisor Dr. Stefanie Steiger for offering me this engaging and methodically diverse project and therefore placing a large amount of trust in me. While teaching me almost everything I know about science, she allowed me to work independently and to pursue my own ideas within this project. Thus far, I have yet to meet another person more passionate about science. She has left me with a desire to continue pursuing science as a physician.

Furthermore, I would like to thank Prof. Dr. Hans-Joachim Anders for his insight and expertise in advancing this project. His passion for science (of the kidney) and his work ethic are infectious. A special thanks goes out to Julian Marschner for always offering methodical guidance and troubleshooting, and to Johannes Bauernschmitt for his moral support, especially in difficult times. A big thanks goes out to all the dear people within the laboratory, many of whom I now happily call friends.

I greatly thank Jana and Dan for their technical expertise and for providing histological staining and mouse genotyping. I also thank Prof. Helen Liapis for granting access to and searching the database of Arcana Laboratories and for proving nephropathological certainty that the structures we found within the kidneys of our novel mouse model were indeed UA tophi.

Last but not least, I would like to thank my parents and grandparents for their unconditional support and love, as well as their ever-present interest in my scientific endeavors.

9 Eidesstattliche Versicherung

Ich erkläre hiermit an Eides statt,

dass ich die vorliegende Dissertation mit dem Titel

„The Pathogenesis of Chronic Uric Acid Crystal Nephropathy“

selbständig verfasst, mich außer der angegebenen keiner weiteren Hilfsmittel bedient und alle Erkenntnisse, die aus dem Schrifttum ganz oder annähernd übernommen sind, als solche kenntlich gemacht und nach ihrer Herkunft unter Bezeichnung der Fundstelle einzeln nachgewiesen habe.

Ich erkläre des Weiteren, dass die hier vorgelegte Dissertation nicht in gleicher oder in ähnlicher Form bei einer anderen Stelle zur Erlangung eines akademischen Grades eingereicht wurde.

München, 02.07.2021	Moritz Hernandez Petzsche
Ort, Datum	Moritz Roman Hernandez Petzsche